Summer 8-15-2017

Topics in QCD at Nonzero Temperature and Density

Kamal Pangeni
Washington University in St. Louis

WASHINGTON UNIVERSITY IN ST. LOUIS

Department of Physics

Dissertation Examination Committee:
Michael C. Ogilvie, Chair
Mark G. Alford
Claude Bernard
P. S. Bhupal Dev
Renato Feres

Topics in QCD at Nonzero Temperature and Density

by

Kamal Pangeni

A dissertation presented to
The Graduate School
of Washington University in
partial fulfillment of the
requirements for the degree
of Doctor of Philosophy

August 2017
St. Louis, Missouri

TABLE OF CONTENTS

LIST OF FIGURES

LIST OF TABLES

ACKNOWLEDGMENTS

This thesis would not have been possible without the direct and indirect help of many individuals. Foremost, I would like to express my sincere gratitude to my advisor, Professor Michael Ogilvie, for taking me as his graduate student and supporting throughout my research and preparation of this thesis. I am thankful for his excellent supervision and immense knowledge that helped me grow as a research scientist. I am also grateful for the opportunity to work with Professor Mark Alford for the last two years. His valuable guidance helped me venture into new research areas during my PhD. I am very thankful for his excellent mentorship and support.

A significant part of the research presented in this thesis was done in collaboration with Dr. Hiromichi Nishimura. I thank him for all his hard work and contribution to our research. Furthermore, I would like to thank Professor Claude Bernard for serving as a member in my mentoring committee and providing helpful comments throughout different stages of my research. I appreciate his feedback after careful reading of this thesis. I am also thankful to other defense committee members, Professor Bhupal Dev and Professor Renato Feres, for their valuable time.

The physics department at Washington University supported me to attend a summer school and a conference where I presented part of the research included in this thesis. I am very grateful to the department for its support. Moreover, I am thankful to all the

faculty members and staffs at the department for a friendly and pleasant learning environment. The graduate school experience would not have been this enjoyable without the many friends I made in the department. They were always there for discussions that provided new perspective in my research. I take this opportunity to express my sincere gratitude to them.

My academic journey from Nepal to the US wouldn't have been successful without the guidance of many teachers in my previous institutions. My sincere thanks to teachers at Brigham Young University (Provo, UT), National School of Sciences (Kathmandu, Nepal), Siddhartha Vanasthali Institute(Kathmandu, Nepal) and Pioneers Higher Secondary School (Waling, Nepal). They provided me with the platform to fulfill my academic goals and always encouraged me to take initiatives and inspired me to work hard.

Finally, my deep and sincere gratitude to my family for their unconditional love and support. I am grateful to my wife, Aradhana, for her unwavering love, support and encouragement. I am forever indebted to my parents for the sacrifices they made to see me excel in academia and always encouraging me to achieve my goals. I am also thankful to my brother and sister for always being there as a friend and supporting throughout my academic career.

Kamal Pangeni

Washington University

August 2017

to my family

ABSTRACT OF THE DISSERTATION

Topics in QCD at Nonzero Temperature and Density

by

Kamal Pangeni

Doctor of Philosophy in Physics

Washington University in St. Louis, 2017

Professor Michael C. Ogilvie, Chair

Understanding the behavior of matter at ultra-high density such as neutron stars require the knowledge of ground state properties of Quantum chromodynamics (QCD) at finite chemical potential. However, this task has turned out to be very difficult because of two main reasons: 1) QCD may still be strongly coupled at those regimes making perturbative calculations unreliable and 2) QCD at finite density suffers from the sign problem that makes the use of lattice simulation problematic and it even affects phenomenological models. In the first part of this thesis, we show that the sign problem in analytical calculations of finite density models can be solved by considering the CK-symmetric, where C is charge conjugation and K is complex conjugation, complex saddle points of the effective action. We then explore the properties and consequences of such complex saddle points at non-zero temperature and density. Due to CK symmetry, the mass matrix eigenvalues in these models are not

always real but can be complex, which results in damped oscillation of the density-density correlation function, a new feature of finite density models. To address the generality of such behavior, we next consider a lattice model of QCD with static quarks at strong-coupling. Computation of the mass spectrum confirms the existence of complex eigenvalues in much of temperature-chemical potential plane. This provides an independent confirmation of our results obtained using phenomenological models of QCD.

The existence of regions in parameter space where density-density correlation function exhibit damped oscillation is one of the hallmarks of typical liquid-gas system. The formalism developed to tackle the sign problem in QCD models actually gives a simple understanding for the existence of such behavior in liquid-gas system. To this end, we develop a generic field theoretic model for the treatment of liquid-gas phase transition. An effective field theory at finite density derived from a fundamental four dimensional field theory turns out to be complex but CK symmetric. The existence of CK symmetry results in complex mass eigenvalues, which in turn leads to damped oscillatory behavior of the density-density correlation function.

In the last part of this thesis, we study the effect of large amplitude density oscillations on the transport properties of superfluid nuclear matter. In nuclear matter at neutron-star densities and temperature, Cooper pairing leads to the formations of a gap in the nucleon excitation spectra resulting in exponentially strong Boltzmann suppression of many

transport coefficients. Previous calculations have shown evidence that density oscillations of sufficiently large amplitude can overcome this suppression for flavor-changing β processes via the mechanism of "gap-bridging". We address the simplifications made in that initial work, and show that gap bridging can counteract Boltzmann suppression of neutrino emissivity for the realistic case of modified Urca processes in matter with $^3P_2$ neutron pairing.

Chapter 1

INTRODUCTION

1.1 Introduction to Quantum Chromodynamics

The discovery of numerous new particles during the 1960's challenged the notion that protons and neutrons are the fundamental particles of nature and they, along with electrons, make up all the matter in our universe. This led Murray Gell-Mann [1] and George Zweig [2] to independently propose the idea that hadrons such as protons and neutrons are not fundamental but are composed of elementary particles called quarks that have fractional electric charge. However, particles with fractional electric charges were not known during that time. This lead to the search for particles with fractional electric charge but none were discovered in nature. However, a series of inelastic baryon scattering experiments [3–5] done in the 1970's provided strong support for the existence of quarks inside of protons and neutrons even though they were not directly observed in nature. This immediately raised the question about the nature of the force that binds the quarks inside of protons and neutrons. It was expected that these forces were carried by the exchange of bosons so it was natural to assume that the force between quarks were mediated by some boson field that later came to be known as the gluon. The existence of the gluon was later confirmed primarily by the discovery of 3-jet events in the inelastic collision of electrons and positrons [6–8].

The modern theory describing the interaction between quarks and gluons is known as quantum chromodynamics(QCD). It is a gauge theory with local symmetry group $SU(3)_c$, the group of 3×3 unitary matrices with unit determinant, in the internal color space. The fundamental degrees of freedom are the quark fields ψ_i^f and gluons A_μ^a. The index i in quark field refers to the color degrees of freedom (i = red, green or blue) while f refers to the different types of quarks commonly referred to as flavors (f = up, down, strange, top, bottom or charm). In QCD, each quark flavor belong to the fundamental representation of $SU(3)_c$ and they are represented by 3 dimensional column vector

$$\psi(x) = \begin{pmatrix} \psi_r(x) \\ \psi_b(x) \\ \psi_g(x) \end{pmatrix} \tag{1.1}$$

where r, g and b refers to the color degrees red, green and blue respectively. The gluon field A_μ^a belongs to the adjoint representation of $SU(3)_c$ and carries color with color index a=1,...,8. The eight different colors are associated with the eight independent generators of $SU(3)_c$.

The Lagrangian density of QCD is:

$$\mathcal{L} = \sum_f \bar{\psi}_i^f (i\not{\partial} - m_f)^{ij} \psi_j^f - \frac{1}{4} F_a^{\mu\nu} F_{\mu\nu a} - g_s \bar{\psi}_j^f A_a^\mu \frac{\lambda_{ji}^a}{2} \gamma_\mu \psi_i^f \tag{1.2}$$

where m_f is the mass of quark with flavor f, g_s is the strong coupling constant, γ_μ's are

the Dirac matrices with Dirac index μ =1,...,4, λ^a's are the Gell-Mann matrices, and $F_a^{\mu\nu} = \partial^\mu A_a^\nu - \partial^\nu A_a^\mu - g_s[A_a^\mu, A_a^\nu]$ is the field strength. The first term in the Lagrangian density (Eq. 1.2) represents the kinetic energy of the quarks, while the second term describes the interaction between gluons. The last term represents the minimal coupling between quarks and gluons. This Lagrangian, by construction, is invariant under transformation by a local symmetry group $SU(3)_c$. Under $SU(3)_c$, the quark field and gluon field transform as

$$\begin{aligned} \psi &\to U(x)\psi \\ A_\mu &\to U(x)A_\mu U^{-1}(x) + \frac{1}{g_s}(\partial_\mu U(x))U^{-1}(x) \end{aligned} \tag{1.3}$$

where $U(x) = \exp(ig_s\theta_a(x)\frac{\lambda_a}{2}) \in \mathrm{SU}(3)$ for some real function $\theta_a(x)$.

In addition to the local symmetry associated with color, the QCD Lagrangian (Eq. 1.2) has global symmetries such as a global $U(1)$ symmetry associated baryon number conservation and approximate chiral symmetry, which will be discussed in section 1.1.1.

1.1.1 Chiral Symmetry

The six quark flavors can be naturally divided into two sectors: light (up, down, strange) and heavy (top, bottom, charm). As a first order approximation the quarks in the light sector can be taken to be massless and the heavy quarks ignored. In this limit, the QCD Lagrangian has a much larger symmetry associated with the chiral flavor symmetry $SU(3)_R \otimes SU(3)_L$.

To see this we separate the quark fields according to their chirality,

$$\psi = \psi_R + \psi_L \quad \text{and } \bar{\psi} = \bar{\psi}_R + \bar{\psi}_L \tag{1.4}$$

where $\psi_R = 1/2(1+\gamma_5)\psi$, $\psi_L = 1/2(1-\gamma_5)\psi$, $\bar{\psi}_R = 1/2(1-\gamma_5)\bar{\psi}$ and $\bar{\psi}_L = 1/2(1+\gamma_5)\bar{\psi}$. If we plug this decomposition back into the Lagrangian then it falls apart into two components, the left handed part and right handed part:

$$\mathcal{L} = \mathcal{L}_1(\psi_R, \bar{\psi}_R) + \mathcal{L}_2(\psi_L, \bar{\psi}_L). \tag{1.5}$$

Each term possess symmetry under global $SU(3)_{L/R}$ rotation in flavor space so the overall symmetry group is the $SU(3)_L \otimes SU(3)_R$. This is known as chiral symmetry and is spontaneously broken by the QCD vacuum. An important consequence of spontaneous symmetry breakdown is the existence of massless Goldstone bosons. In the case of chiral symmetry breakdown, the associated Goldstone bosons are the pions and pseudoscalar mesons. If the quarks were truly massless then the pions would also have been massless but up and down quarks have small mass so we expect pions to have small mass, which is indeed the case. A phenomenological model of QCD with chiral symmetry breaking effects will be introduced in sec 1.7, and further analysis will be presented in chapter 3.

1.2 Asymptotic freedom

Asymptotic freedom refers to the phenomenon where the interaction strength between particles gets weaker with increasing energy. In the context of QCD, it was discovered in 1973 by D.J. Gross, F. Wilczek [9] and H.D.Politzer [10]. The change in coupling constant (often referred as "running of the coupling constant") with energy scale is mathematically expressed as

$$\mu \frac{d}{d\mu} \alpha(\mu)|_{\alpha_0} = \beta(\alpha) \tag{1.6}$$

where $\alpha_s = g_s^2/4\pi$ and α_0 refers to the fixed bare coupling . The beta function, $\beta(\alpha)$, in the case of QCD for N_f flavor of quarks to lowest order is [11]

$$\beta(\alpha) = \frac{\alpha^2}{\pi}(-33/6 + N_f/3). \tag{1.7}$$

We can see that for $N_f < 33/2$ the beta function is negative, which implies that the coupling (α) decreases with increasing energy scale (μ). This is important as it allows for pertubative QCD calculations and to test it against the result of high energy experiments. Major confidence in QCD as theory of strong interaction came from the agreement of perturbative calculations with results of experiments at high energies. In addition, asymptotic freedom implies that the perturbation theory is valid at high temperature and density and it can use it to explore the phase structure in that regime. At low temperature and density, where the coupling is still large, the only first principle tool we have to study the phase structure is lattice QCD, which will be introduced in the next section.

1.3 Lattice QCD

At low energies where the QCD coupling is strong and perturbative approaches fail, lattice QCD provides an *ab initio* tool for calculating the hadron spectrum [12, 13] and studying non-perturbative aspects of QCD such as color confinement [14] and chiral symmetry breaking [15, 16]. It is formulated on a discrete euclidean space-time grid that naturally provides a cutoff and thus regularizes the ultraviolet behavior of the theory. Once formulated on a lattice, it can be treated as a statistical mechanics system [17] which can be simulated on computer systems using standard Monte-Carlo techniques [18]. Lattice models can also be studied using standard statistical mechanics methods such as mean field approximation and strong coupling expansion [19].

1.3.1 Fermionic action on lattice

Consider the fermionic part of the QCD action in the continuum

$$S_F^0[\psi, \bar{\psi}] = \int d^4x \bar{\psi}(x)(\gamma^\mu \partial_\mu + m)\psi(x). \tag{1.8}$$

To obtain the lattice version of this action we start by discretizing spacetime into 4-dimensional euclidean square lattice "Λ" with lattice spacing "a". In principle, different discretization schemes can be used, but one needs to recover the correct continuum limit as the lattice spacing "a" goes to zero. After discretization, we place the fermions at each lattice site and

replace the derivative and integral in Eq. 1.8 with their discrete versions as follows

$$\begin{aligned}
&\psi(x) \to \psi(n) \\
&\bar{\psi}(x) \to \bar{\psi}(n) \\
&\partial_\mu \psi \to \frac{1}{2a}(\psi(n+\hat{\mu}) - \psi(n-\hat{\mu})) \\
&\int d^4x \to a^4 \sum_{n\in\Lambda}.
\end{aligned} \tag{1.9}$$

With this straightforward substitution we end up the following lattice action:

$$S_F^0[\psi, \bar{\psi}] = a^4 \sum_{n\in\Lambda} \bar{\psi}(n) \left(\sum_{\mu=1}^{4} \gamma_\mu \frac{\psi(n+\hat{\mu}) - \psi(n-\hat{\mu})}{2a} + m\psi(n) \right). \tag{1.10}$$

However, this naive discreitized form of the lattice action is not gauge invariant. Under gauge transformation the fermion fields transform as

$$\begin{aligned}
\psi(n) &\to \psi'(n) = \Omega(n)\psi(n) \\
\bar{\psi}(n) &\to \bar{\psi}'(n) = \bar{\psi}(n)\Omega(n)^\dagger
\end{aligned} \tag{1.11}$$

where Ω(n) is an element of the gauge group. It is easy to see that while the mass term in Eq. 1.10 is gauge invariant, the derivative term is not. Gauge invariance can be restored by introducing a new field $U_\mu(n)$ and redefining the derivative in the following way:

$$\partial_\mu \psi \to \frac{1}{2a}(U_\mu(n)\psi(n+\hat{\mu}) - U_{-\mu}(n)\psi(n-\hat{\mu})) \tag{1.12}$$

where $U_{-\mu}(n) = U_\mu(n-\hat{\mu})^\dagger$. We require $U_\mu(n)$ to have following transformation property under a gauge transformation

$$U_\mu(n) \to U'_\mu(n) = \Omega(n) U_\mu(n) \Omega(n+\hat{\mu})^\dagger. \tag{1.13}$$

With this new definition of derivative, we get

$$S_F^0[\psi, \bar{\psi}] = a^4 \sum_n \bar{\psi}(n) \left(\sum_{\mu=1}^{4} \gamma_\mu \frac{U_\mu(n)\psi(n+\hat{\mu}) - U_{-\mu}(n)\psi(n-\hat{\mu})}{2a} + m\psi(n) \right) \tag{1.14}$$

which is now gauge invariant. U_μ acts as a connection between fermions at adjacent lattice sites, so it is often referred to as "link variable". The link variable is related to the continuum gauge fields A_μ via the relation

$$U_\mu(n) = \exp(iaA_\mu(n)). \tag{1.15}$$

Though gauge invariant, the lattice action in Eq. 1.14 has other lattice artifacts such as the fermion doubling problem. We will not discuss these issues here but interested readers can refer to [20] for more discussion.

1.3.2 Gauge fields on lattice

The link variable $U_\mu(n)$ was introduced in the previous section to preserve the gauge invariance of the fermionic part of the lattice action. These link variables are the lattice counterpart of the fields A_μ and play a fundamental role in the construction of the action for

the gluonic degrees of freedom in lattice. Instead of starting with the continuum action for gluon fields and discretizing it, one can use gauge invariant objects constructed out of links to build an action for gluon fields on the lattice. Gauge invariant objects on the lattice can be constructed by taking the trace over the products of link variables $U_\mu(n)$ along a closed path. The simplest non-trivial closed path contour with perimeter of four links is called a plaquette. A plaquette in the $\mu - \nu$ plane is defined as

$$U_{\mu\nu} = U_\mu(n)U_\nu(n+\hat{\mu})U_\mu(n+\hat{\nu})^\dagger U_\nu(n)^\dagger. \tag{1.16}$$

A gauge invariant action constructed out of these plaquettes is commonly referred to as the "plaquette action" or the Wilson action, and it has the following form:

$$S_G[U] = \frac{2N}{g^2}\sum_n \sum_{\mu<\nu} \text{Re tr}[1 - U_{\mu\nu}(n)]. \tag{1.17}$$

The normalization factor in Eq. 1.17 is chosen so that we recover the correct continuum limit as $a \to 0$. It is easy to expand the link variables in power series of A_μ's and verify that the leading order expansion is indeed proportional to $F_{\mu\nu}^2$, the correct continuum limit [21]. An important gauge invariant quantity that plays a crucial role in our understanding of confinement is the trace of the Wilson loop. The Wilson loop is defined as

$$W[U] = \prod_{(n,\mu)\in\mathcal{L}} U_\mu(n) \tag{1.18}$$

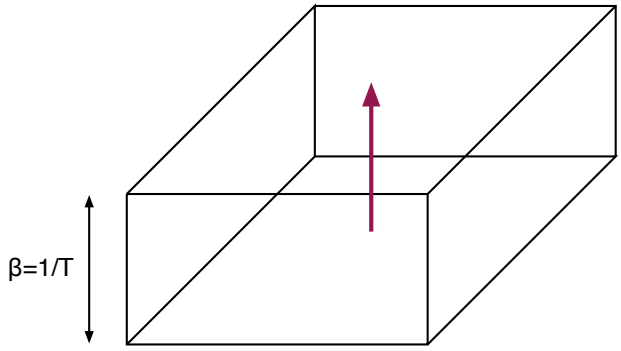

Figure 1.1: The Polyakov loop as the worldline of a heavy particle.

where $\mathcal{L}$ refers to a closed loop. The trace of a rectangular Wilson loop of spatial width L and time length T can be associated with a particle-antiparticle pair that are created at one time and move to a separation L and move forward in time for an interval T, and then annihilate [22]. The expectation value of the Wilson loop is associated with the effective potential of the heavy quark.

$$\langle Tr_R W[C] \rangle \sim \exp[-V_R(L)T] \tag{1.19}$$

where $V_R(L)$ is the heavy quark-antiquark potential for particles in representation R.

$$V(L) \to \sigma_R L + \mathcal{O}(1) \tag{1.20}$$

σ_R is the string tension. A non-zero value of the string tension implies confinement as the potential rises linearly with distance. For a review of quark confinement see [23].

1.4 Pure Gauge theory at finite temperature

Finite temperature is implemented by compactifying the euclidean time direction. The length of the compactified dimension is given by β, the inverse of the temperature T. String tension at finite temperature can be measured using the Polyakov loop, $P(\vec{x})$, which is basically the Wilson loop that is periodic in the compactified direction, as show in Fig. 1.1 [24]. Formally,

$$P(\vec{x}) = \mathcal{P} \exp[i \int_0^\beta dx_4 A_4(x)] \tag{1.21}$$

where $\mathcal{P}$ refers to path ordering. The one-point function of the Polyakov loop, $\langle Tr_R P(\vec{x}) \rangle$, can be interpreted as the Boltzmann factor $\exp(-\beta F_R)$ where F_R is the free energy needed to add static quarks in the system. Under $Z(N)$, the center of the group SU(3), the lattice action remains invariant but the Polyakov loop transforms as $P(\vec{x}) \to zP(\vec{x})$. In the case of unbroken $Z(N)$, $\langle Tr_R P(\vec{x}) \rangle = 0$, which implies $F_R = \infty$. This implies confinement as an infinite amount of free energy is required to introduce the new quark into the system. However, in the case of broken $Z(N)$, $\langle Tr_R P(\vec{x}) \rangle \neq 0$ implying $F_R \neq \infty$. This signals the deconfined phase of QCD. The string tension at finite temperature can be determined from the two-point function of the Polyakov loop

$$\langle Tr_R P(\vec{x}) Tr_R P(\vec{y}) \rangle \sim e^{-\beta \sigma_R |\vec{x}-\vec{y}|} \tag{1.22}$$

1.5 QCD phase diagram

QCD is expected to have a rich phase structure at finite temperature and density[25, 26]. The theoretical understanding of different phases is important as they can be realized in heavy ion experiments, in the early universe and in compact stars [27–29]. Furthermore, the study of different phases and the transition between them can provide insight into non-perturbative effects such as confinement and chiral symmetry breaking. These phases, in principle, can be studied using both analytical and numerical methods. However, the strong coupling nature of the QCD vacuum has limited the analytical study to high energy regions where the coupling is weak. In strong coupling regions, numerical methods based on lattice simulations have been the principle method to study phase structure from first principles.

Fig. 1.2[1] shows the conjectured phase diagram of QCD in the temperature-chemical potential plane. We can see three main phases: the hadronic phase at low temperature and density, the Quark Gluon Plasma (QGP) phase at high temperature and the density and the color superconducting phase at high density and low temperature. The hadronic phase is characteized by permanent confinement of quarks and the breaking of chiral symmetry by quark-antiquark condensate, while the QGP phase is characterized by the presence of free quarks and restoration of chiral symmetry. In the color superconducting phase, chiral symmetry is again broken in this case by the diquark condensate.

[1]Figure from: http://www.jicfus.jp/en/wp-content/uploads/2012/12/QGPT.jpg

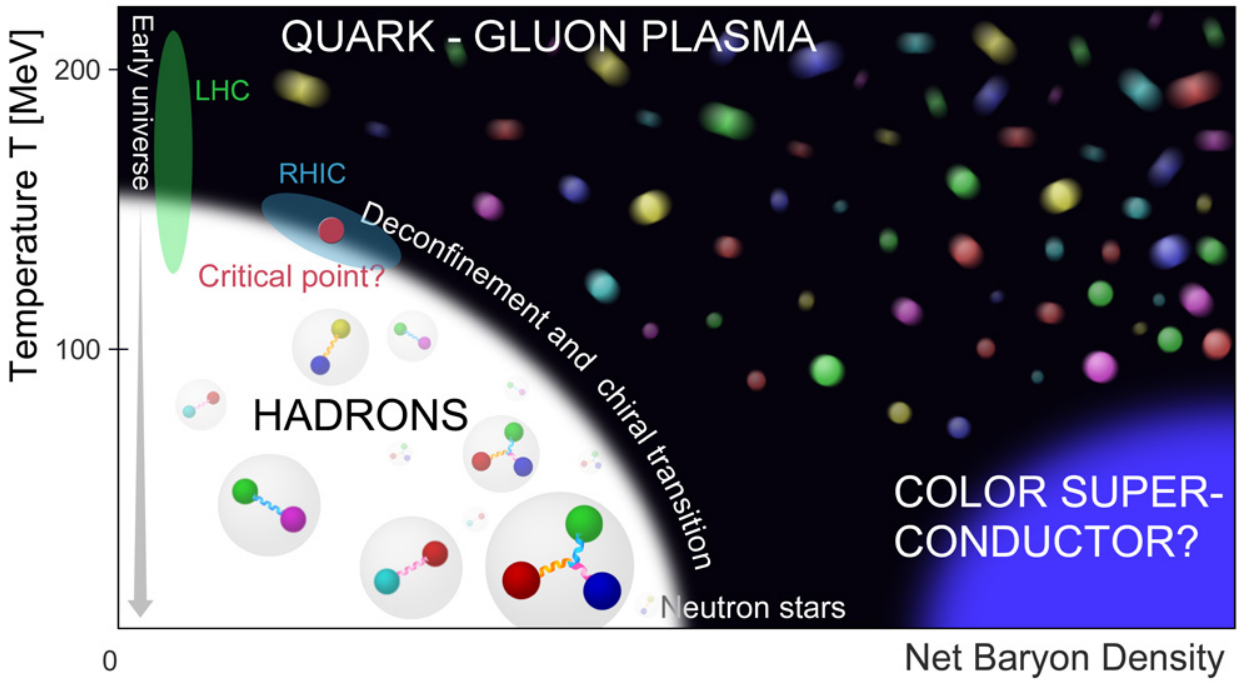

Figure 1.2: Phase diagram of QCD

The phase structure along the temperature axis and at zero density has been extensively studied using lattice simulations [30, 31]. These studies provided the first conclusive theoretical evidence for the existence of the deconfined Quark Gluon Plasma (QGP) phase which was later confirmed by the elliptic flow measurments from heavy ion collision experiments at LHC and RHIC [27]. Early studies on the lattice with gluons only showed a first order transition from a low temperature hadronic phase to a high temperature QGP phase [32–34]. Improved calculations performed using physical quark masses revealed that the QCD phase transition is a crossover [35] that happens at a temperature of around 140 MeV.

While lattice simulation of QCD at finite temperature has been very successful, the study

of the phase structure at finite density has been severely restricted by the sign problem. As a result, most of our understanding of this region is based on the study of phenomenological models. Results obtained from phenomenological models [22] suggest a first order transition from the hadronic phase to a QGP phase at a density around the scale of the hadron mass. With increasing temperature, the first order transition weakens and the critical density at which the first order transition occurs decreases. Eventually, the first order transition ends at a second order critical end point as shown in Fig. 1.2. The critical end point plays a very significant role in determining the universal properties of the theory. The QCD critical end point is widely expected to fall in the Ising, or liquid-gas universality class [36]. There have been experimental efforts to determine the exact location and universality calls of this critical end point [37].

At asymptotically high density and low temperature, the weakly interacting quarks pair up to form "Cooper pairs ", giving rise to color superconductivity [38, 39]. The type of pairing depends on the actual density of the matter. At the highest density, all three flavors of quark pair symmetrically and produce a color-flavor-locked (CFL) phase [40]. At lower densities other pairing patterns are preferred, which result in a variety of phases such as acrystalline phase, a two-flavor pairing, or spin-locked phase. For a through review about different phases of color superconducting matter see [26].

1.6 Nature of the sign Problem in finite density QCD

The partition function in lattice QCD is calculated by a performing the path integral over all field configurations weighted by the exponential of the action in Euclidean space-time.

$$Z_{LQCD} = \int \mathcal{D}A\mathcal{D}\psi\mathcal{D}\bar{\psi}e^{-S_{LQCD}} \tag{1.23}$$

where A represents the gluon field, ψ and $\bar{\psi}$ represents the fermionic fields, and S_{LQCD} is the QCD action.

$$S_{LQCD} = \int d^4x \left(\frac{1}{4}F_{\mu\nu}F^{\mu\nu} - \bar{\psi}M(A,m,\mu)\psi\right) \tag{1.24}$$

where $M(A,m,\mu) = \not{D} + m + \mu\gamma_0$ is the Dirac Operator. The fermionic part of the integral can be done analytically, resulting in

$$Z_{LQCD} = \int \mathcal{D}A \, \det[\not{D} + m + \mu\gamma_0] \exp\left(-\int d^4x \frac{1}{4}F_{\mu\nu}F^{\mu\nu}\right) \tag{1.25}$$

where $\det[\not{D} + m + \mu\gamma_0]$ is the functional determinant. A popular method for calculating this type of integral numerically is Monte-Carlo simulation which works as long as the weight function is positive. The determinant of the Dirac operator in Eq. 1.24 satisfies $\det(\not{D} + m + \mu\gamma^0) = \det^*(\not{D} + m - \mu^*\gamma_0)$, which constrains the determinant to be real only when μ is zero or purely imaginary. For real non zero values of μ the determinant is complex so the usual Monte-Carlo techniques do not work. This problem of complex weights is commonly referred to as the sign problem and is found in many areas of physics [41–43].

The sign problem in QCD has been known since the first lattice simulation at nonzero chemical potential was carried out by Barbour et. al in 1986 [44], and no definitive solution has been found yet. Due to the lack of lattice results, phenomenological models have been a popular tool to explore many features of finite density QCD. However, analytical calculations in these phenomenological models in mean field approximation are also affected by sign problem. This thesis will present a way to solve the sign problem that appears in analytical calculations in mean-field versions of finite density models. The next section will provide an introduction to an effective model of QCD.

1.7 Nambu-JonaLasino model

As mentioned in previous sections, the enormous difficulties one encounters in analytical as well as numerical treatment of QCD has motivated physicists to study simple, mathematically tractable, models that embody the symmetry of QCD and its spontaneous breakdown. As a consequence, these models have many features similar to QCD and can be studied analytically. One such popular model is the Nambu-JonaLasinio (NJL) model that was originally constructed as theory for the nucleon [45, 46] but later reinterpreted as a theory of quarks. It embodies the chiral symmetry of QCD and its spontaneous breakdown at low energies which is responsible for the dynamical generation of quark masses. It also reproduces many well known results of current-algebra that hold for QCD [47–49].

The Lagrangian for NJL model with two flavors of quarks is

$$\mathcal{L} = \bar{\psi}(i\partial\!\!\!/ - m_q)\psi + G\{(\bar{\psi}\psi)^2 + (\bar{\psi}i\gamma_5\vec{\tau}\psi)^2\} \tag{1.26}$$

where m_q is the current mass of quarks, G is the four-fermion coupling and $\vec{\tau}$ are the generators of flavor symmetry group SU(2). By construction this Lagrangian is invariant under $SU_V(2) \otimes SU_A(2) \otimes U_V(1)$ symmetry, the symmetries of two flavor QCD. Unlike QCD, where the fermions interact by exchange of gluons, the fermion interaction in the NJL model is point-like. As a consequence this model is non-renormalizable, and a cutoff parameter is needed to regulate the theory.

A mean field approximation to the thermodynamic potential is given by

$$V_{NJL} = \frac{1}{4G}(M - m_q)^2 - 2N_c N_f \int_0^\Lambda \frac{d^3p}{(2\pi)^3}\{E_p + T\log[1 + e^{-(E_p-\mu)/T}] + T\log[1 + e^{-(E_p+\mu)/T}]\} \tag{1.27}$$

where $E_p = \sqrt{p^2 + M^2}$, $M = m_q - 2G\langle\bar{q}q\rangle$ and Λ is the three-momentum cut-off. Minimizing the effective potential of NJL with respect to M results in a self consistent equation for M.

$$M = m_q + \frac{4GN_cN_f}{\pi^2}\int_0^\Lambda p^2 \frac{M}{E_p}\left(1 - \frac{1}{1 + e^{(E_p-\mu)/T}} - \frac{1}{1 + e^{(E_p+\mu)/T}}\right) \tag{1.28}$$

The solution of this self consistent equation is plotted as a function of temperature in Fig. 1.3 for $m_q = 5.5$ MeV, $G = 5.496$ GeV^{-2} and $\Lambda = 631.4$ MeV. These parameters are chosen

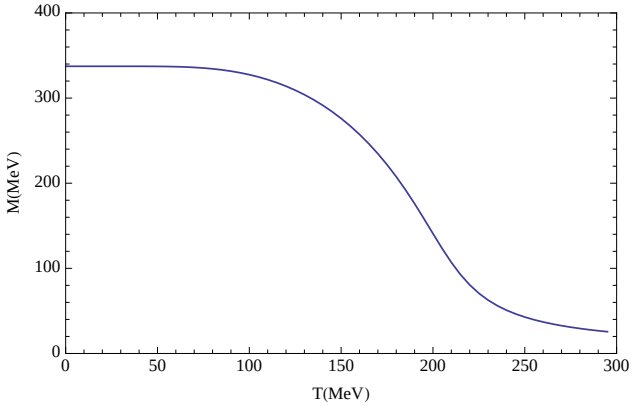

Figure 1.3: The constituent quark mass (M) as function of temperature in the two flavor NJL model.

so that the correct pion mass and decay constant are reproduced at zero temperature [47]. As clearly seen in the plot, the constituent quark mass (M) is large for low temperatures reflecting the spontaneous breakdown of chiral symmetry ($\langle\bar{q}q\rangle \neq 0$). However, at large temperature the constituent masss approaches the bare mass reflecting the restoration of chiral symmetry ($\langle\bar{q}q\rangle$=0).

1.8 Polyakov loop extended NJL model

The NJL model has had widespread success in describing the low-energy hadronic physics that is dominated by chiral symmetry. However, this model lacks quark confinement which is an important aspect of QCD. Conceptually the phenomena of deconfinement and chiral symmetry restoration are entirely different, but lattice simulations with dynamical quarks have shown that they occur around the same temperature [50, 51]. This suggests an interplay between the order parameters of chiral dynamics and deconfinement, the chiral condensate ($\langle\bar{q}q\rangle$) and the Polyakov loop (P) respectively. The first successful study to reproduce both

deconfinement and chiral-symmetry restoration was done by Gocksch and Ogilvie in the strong coupling lattice model using an expansion for a large number of dimensions [52]. In the context of the NJL model, the effect of Polyakov loop on chiral restoration was first studied in [53], where the authors found that chiral restoration in quenched QCD depends crucially on the Z_3 phase of the Polyakov loop. Later, Kenji Fukushima extended the NJL model by introducing the effective potential for Polyakov loop which is now commonly referred to as PNJL model [54]. The details of the PNJL model is discussed in chapter 3.

Chapter 2

COMPLEX SADDLE POINTS IN QCD AT FINITE TEMPERATURE AND DENSITY

This chapter contains the materials published under the same title [1]*. This work was done in collaboration with Dr. Hiromichi Nishimura under the supervision of my advisor, Prof. Michael Ogilvie*

As discussed in the introduction, the sign problem is a fundamental issue in the study of QCD at finite density, manifesting as complex weights in the path integral that make lattice simulations extremely problematic [41–43]. However, the sign problem also appears in analytical calculations of mean-field type. Here we show that the sign problem can be solved in such calculations provided a fundamental symmetry of finite-density models, $\mathcal{CK}$ symmetry, is respected. This leads to the analytic continuation of Polyakov loop eigenvalues into the complex plane from the unit circle. Our results are complementary to recent work on simulations of lattice field theories at finite densities using the theory of Lefschetz thimbles [55–60], and give an indication of how analytical and simulation results might be combined to give a comprehensive picture of gauge theories at finite density.

Let us consider an $SU(N)$ gauge theory coupled to fermions in the fundamental representation. It is well known that the log of the fermion determinant, $\log\det(\mu, A)$, which is a function of the quark chemical potential μ and the gauge field A, can be formally expanded as a sum over Wilson loops with real coefficients. For a gauge theory at finite temperature, the

[1] Nishimura, H., Ogilvie, M.C. and Pangeni, K., 2014. Complex saddle points in QCD at finite temperature and density. Physical Review D, 90(4), p.045039.

sum includes Wilson loops that wind nontrivially around the Euclidean timelike direction; Polyakov loops, also known as Wilson lines, are examples of such loops. At $\mu = 0$, every Wilson loop $\mathrm{Tr}_F W$ appearing in the expression for the fermion determinant is combined with its conjugate $\mathrm{Tr}_F W^\dagger$ to give a real contribution to path integral weighting. This can be understood as a consequence of charge conjugation invariance $\mathcal{C}$, which acts on the gauge field as

$$\mathcal{C} : A_\mu \to -A_\mu^t \tag{2.1}$$

and thus exchanges $\mathrm{Tr}_F W$ and $\mathrm{Tr}_F W^\dagger$. When $\mu \neq 0$, Wilson loops with nontrivial winding number n in the x_4 direction receive a weight $e^{n\beta\mu}$ while the conjugate loop is weighted by $e^{-n\beta\mu}$. Thus it is seen that these loops break charge conjugation invariance when $\mu \neq 0$. However, $\mathrm{Tr}_F W$ transforms into itself under the combined action of $\mathcal{CK}$, where $\mathcal{K}$ is the fundamental antilinear operation of complex conjugation. Thus the theory is invariant under $\mathcal{CK}$ even in the case $\mu \neq 0$. For fermions, $\mathcal{CK}$ symmetry implies the well-known relation $\det(-\mu, A_\mu) = \det(\mu, A_\mu)^*$ for Hermitian A_μ, but can be used with bosons as well as fermions.

Given the existence of the symmetry $\mathcal{CK}$ at finite density, we wish to ensure that, in the absence of spontaneous symmetry breaking, calculational methods of all types respect the symmetry. For perturbative or mean-field type calculations, this leads naturally to the consideration of complex but $\mathcal{CK}$-symmetric saddle points for some effective potential at finite temperature and density V_{eff} , such that the free energy density is given by the value

of V_{eff} at the dominant saddle point. Such saddle points have been seen before in finite-density calculations [61–64]. A field configuration is $\mathcal{CK}$ symmetric if $-A_\mu^\dagger$ is equivalent to A_μ under a gauge transformation. For such a field configuration, it is easy to see that every Wilson loop is real and thus $\det(\mu, A_\mu)$ is real and positive.

Let us consider the Polyakov loop P associated with some particular field configuration that is $\mathcal{CK}$ symmetric. We can transform to Polyakov gauge where A_4 is diagonal and time independent, and work with the eigenvalues θ_j defined by

$$P(\vec{x}) = \mathrm{diag}\left[e^{i\theta_1(\vec{x})}, \cdots, e^{i\theta_N(\vec{x})}\right] \tag{2.2}$$

where the θ_j's are complex but satisfy $\sum_j \theta_j = 0$. Because we are primarily interested in constant saddle points, we suppress the spatial dependence hereafter. Invariance under $\mathcal{CK}$ means that the set $\left\{-\theta_j^*\right\}$ is equivalent to the $\{\theta_j\}$ although the eigenvalues themselves may permute. In the case of $SU(3)$, we may write this set uniquely as

$$\{\theta - i\psi, -\theta - i\psi, 2i\psi\}\,. \tag{2.3}$$

This parametrizes the set of $\mathcal{CK}$-symmetric $SU(3)$ Polyakov loops. Notice that both

$$\mathrm{Tr}_F P = e^{\psi} 2\cos\theta + e^{-2\psi} \tag{2.4}$$

and

$$\mathrm{Tr}_F P^\dagger = e^{-\psi} 2\cos\theta + e^{2\psi} \tag{2.5}$$

are real, but they are equal only if $\psi = 0$. In the usual interpretation of the Polyakov loop expectation value, this implies that the free energy change associated with the insertion of a fermion is different from the free energy change associated with its antiparticle. It is easy to check that the trace of all powers of P or $P^\dagger$ are all real, and thus all group characters are real as well. This parametrization represents a generalization of the Polyakov loop parametrization used in the application of mean-field methods to confinement, *e.g.*, in PNJL models [65] or in gauge theories with double-trace deformations [66, 67]. This parametrization can be generalized to include finite-density models for arbitrary N.

The existence of complex $\mathcal{CK}$-symmetric saddle points provides a fundamental approach to non-Abelian gauge theories that is similar to the heuristic introduction of color chemical potentials, and naturally ensures the system has zero color charge, *i.e.*, all three charges contribute equally [68]. In the case of $SU(3)$, extremization of the thermodynamic potential with respect to θ leads to the requirement $\langle n_r \rangle - \langle n_g \rangle = 0$ where $\langle n_r \rangle$ is red color density, including the contribution of gluons. Similarly, extremization of the thermodynamic potential with respect to ψ leads to $\langle n_r \rangle + \langle n_g \rangle - 2\langle n_b \rangle = 0$. Taken together, these two relations imply that $\langle n_r \rangle = \langle n_g \rangle = \langle n_b \rangle$.

We demand that any saddle point solution be stable to constant, real changes in the Polyakov loop eigenvalues, corresponding for $SU(3)$ to constant real changes in A_4^3 and A_4^8.

Consider the $(N-1)\times(N-1)$ matrix M_{ab}, defined in Polyakov gauge as

$$M_{ab} \equiv g^2 \frac{\partial^2 V_{eff}}{\partial A_4^a \partial A_4^b}. \tag{2.6}$$

The stability criterion is then that the eigenvalues of M must have positive real parts. At $\mathcal{CK}$-symmetric saddle points, the eigenvalues will be either real or part of a complex conjugate pair. In the case of $SU(3)$, the matrix M may also be written in terms of derivatives with respect to θ and ψ as

$$M = \frac{g^2}{T^2} \begin{pmatrix} \frac{1}{4}\frac{\partial^2 V_{eff}}{\partial \theta^2} & \frac{i}{4\sqrt{3}}\frac{\partial^2 V_{eff}}{\partial \theta \partial \psi} \\ \frac{i}{4\sqrt{3}}\frac{\partial^2 V_{eff}}{\partial \theta \partial \psi} & \frac{-1}{12}\frac{\partial^2 V_{eff}}{\partial \psi^2} \end{pmatrix}. \tag{2.7}$$

This stability criterion generalizes the stability criterion used previously for color chemical potentials, which was $\partial^2 V_{eff}/\partial\psi^2 < 0$. Crucially, the mass matrix M is invariant under $M^* = \sigma_3 M \sigma_3$, which is a generalized parity-time ($\mathcal{PT}$) symmetry transformation [69, 70]. It is easy to see that this relation implies that M has either two real eigenvalues or a complex eigenvalue pair.

We first illustrate the working of $\mathcal{CK}$ symmetry using the well-known one-loop expressions for the effective potential of particles moving in a constant background Polyakov loop. The one-loop contribution to the effective potential of N_f flavors of fundamental fermions moving in a background gauge field A is given by

$$\beta \mathcal{V} V_{eff}^f = -N_f \log\left[\det\left(\mu, A\right)\right] \tag{2.8}$$

where det again represents the functional determinant of the Dirac operator and $\beta\mathcal{V}$ is the volume of spacetime. A compact expression for the effective potential of massless fermions when the eigenvalues of P are complex was derived using zeta function methods in [71]. It will be useful in what follows to repeat their derivation and check the reality of V_{eff}^{f} for $\mathcal{CK}$-symmetric backgrounds. Our starting point is the finite-temperature contribution to the effective potential of a single Dirac fermion in a $U(1)$ background Polyakov loop characterized by an angle θ:

$$v_f(\theta) = -2T \int \frac{d^3k}{(2\pi)^3} \left\{ \log\left[1 + e^{-\beta\omega_k + i\theta}\right] + \log\left[1 + e^{-\beta\omega_k - i\theta}\right] \right\}. \tag{2.9}$$

Setting the fermion mass to zero, and expanding the logarithms, we obtain

$$v_f(\theta) = -\frac{4T^4}{\pi^2} \sum_{n=1}^{\infty} \frac{(-1)^{n+1}}{n^4} \cos(n\theta). \tag{2.10}$$

After expanding the cosine and interchanging the order of summation, we get

$$v_f(\theta) = -\frac{4T^4}{\pi^2} \sum_{m=0}^{\infty} \frac{(-1)^m \theta^{2m} \eta(4-2m)}{(2m)!} \tag{2.11}$$

where η is the Dirichlet eta function. Only the first three terms of the expansion are nonzero, and we arrive at

$$v_f(\theta) = -\frac{4T^4}{\pi^2} \left(\frac{\theta^4}{48} - \frac{\pi^2\theta^2}{24} + \frac{7\pi^4}{720} \right). \tag{2.12}$$

This expression is valid provided $Re[\theta] \in (-\pi, \pi)$. In general, if θ is complex, so is v_f.

However, the free energy of quarks in a $\mathcal{CK}$-symmetric background Polyakov loop is always real. For $SU(3)$, we have

$$V_f(\theta,\psi,\mathrm{T},\mu) = N_f\left(v_f\left(\theta - i\psi - \frac{i\mu}{T}\right) + v_f\left(-\theta - i\psi - \frac{i\mu}{T}\right) + v_f\left(2i\psi - \frac{i\mu}{T}\right)\right) \quad (2.13)$$

which is explicitly real. For two massless flavors, the result is

$$\begin{aligned} V_f(\theta,\psi,\mathrm{T},\mu) &= -\frac{\mu^4}{2\pi^2} + T^2\left(-\mu^2 + \frac{2\theta^2\mu^2}{\pi^2} - \frac{6\mu^2\psi^2}{\pi^2}\right) + \frac{4T^3\left(\theta^2\mu\psi + \mu\psi^3\right)}{\pi^2} \\ &\quad + \frac{T^4\left(-7\pi^4 + 20\pi^2\theta^2 - 10\theta^4 - 60\pi^2\psi^2 + 60\theta^2\psi^2 - 90\psi^4\right)}{30\pi^2}. \end{aligned} \quad (2.14)$$

Because we are interested in the analytic continuation of Polyakov loop eigenvalues into the complex plane, we need expressions for the gauge bosons as well as for fermions. Our starting point in this case is

$$v_b(\theta) = 2T\int\frac{d^3k}{(2\pi)^3}\left\{\log\left[1 - e^{-\beta\omega_k + i\theta}\right] + \log\left[1 - e^{-\beta\omega_k - i\theta}\right]\right\} \quad (2.15)$$

which represents the one-loop of two gauge bosons of opposite $U(1)$ charge. A naive repetition of the zeta-function argument that was successful for fermions fails for bosons even in the case where θ is real. The expansion of $v_b(\theta)$ around $\theta = 0$ is invalid, because the final result is only valid for $0 \leq Re[\theta] \leq 2\pi$. In contrast, the fermionic expression is valid for

$-\pi \leq Re\,[\theta] \leq \pi$. However, it is possible to define the bosonic analog of $v_f\,(\theta)$ by [72]

$$v_b\,(\theta) = -v_f\,(\theta - \pi) \tag{2.16}$$

and this leads to the correct expression when $Re\,[\theta] \in (0, 2\pi)$:

$$v_b\,(\theta) = -\frac{\left(-15\theta^4 + 60\pi\theta^3 - 60\pi^2\theta^2 + 8\pi^4\right) T^4}{180\pi^2}. \tag{2.17}$$

As in the fermionic case, $v_b\,(\theta)$ is generally complex if θ is complex. However, the one-loop gluonic contribution for a $\mathcal{CK}$-symmetric Polyakov loop background, given by

$$V_g(P) = v_b(0) + v_b(2\theta) + v_b(\theta + i3\psi) + v_b(\theta - i3\psi) \tag{2.18}$$

is real. Explicitly, we have for $SU(3)$

$$V_g(P) = \frac{T^4\left(135\left(\theta^2 - 3\psi^2\right)^2 + 180\pi^2\left(\theta^2 - 3\psi^2\right) + 60\pi\theta\left(27\psi^2 - 5\theta^2\right) - 16\pi^4\right)}{90\pi^2} \tag{2.19}$$

which is real. Note that the valid range of θ is $(0, \pi)$ due to the appearance of 2θ as an eigenvalue in the adjoint representation. The one-loop effective potential is simply the sum of $V_g(\theta)$ and $V_f(\theta)$. As is the case when $\mu = 0$, the dominant saddle point remains at $\theta = 0$ when $\mu \neq 0$.

We now consider a simple phenomenological model that combines the one-loop result with the effects of confinement for the case of $SU(3)$ gauge bosons and two flavors of massless

fermions at finite temperature and density. The model is described by an effective potential which is the sum of three terms:

$$V_{eff}(P) = V_g(P) + V_f(P) + V_d(P) \tag{2.20}$$

where $V_g(P) + V_f(P)$ is the one-loop effective potential for gluons and quarks given above and $V_d(P)$ is an additional term that favors the confined phase [24, 66, 73, 74]. There are two different points of view that can be taken on this model. In one view, $V_d(P)$ represents a deformation of the original model. In typical applications, the temperature T is taken to be large such that perturbation theory is reliable in the chromoelectric sector because the running coupling $g^2(T)$ is small. The deformation term is taken to respect center symmetry and is used to move between the confined and deconfined phases in a controlled way. The gauge contribution $V_g(P)$ favors the deconfined phase, and in the pure gauge theory ($N_f = 0$) the deconfinement transition arises out of the competition between $V_g(P)$ and $V_d(P)$. The confined phase arising in models of this type is known to be analytically connected to the usual low-temperature confined phase of $SU(3)$ gauge theory [66]. This point of view emphasizes analytic control at the price of deforming the original gauge theory by the addition of $V_d(P)$. From the second point of view, the entire model is phenomenological in nature, with the potential $V_d(P)$ models the unknown confining dynamics of the pure gauge theory. The parameters of $V_d(P)$ are set to reproduce the deconfinement temperature of the pure gauge theory, known from lattice simulations to occur at $T_d \approx 270\,\mathrm{MeV}$.

We will take the second point of view, using a simple expression for $V_d(P)$ that reproduces

much of the thermodynamic behavior seen in lattice simulations of the pure gauge theory. The specific form used is Model A of [73], where the two terms $V_g(P) + V_d(P)$ can be written together as

$$V_A(\theta) = -\sum_{j,k=1}^{N} \frac{1}{\pi^2}(1 - \frac{1}{N}\delta_{jk}) \left[-\frac{2\pi^4}{3\beta^4} B_4\left(\frac{\Delta\theta_{jk}}{2\pi}\right) - \frac{m^2\pi^2}{2\beta^2} B_2\left(\frac{\Delta\theta_{jk}}{2\pi}\right) \right] \tag{2.21}$$

where $\Delta\theta_{jk} = |\theta_j - \theta_k|$ are the adjoint Polyakov loop eigenvalues and B_j is the j'th Bernoulli polynomial. This expression gives a simple quartic polynomial in the Polyakov loop eigenvalues and thus can be thought of as a form of Landau-Ginsburg potential for the Polyakov loop eigenvalues. For the $SU(3)$ parametrization used here, $V_d(P)$ takes the simple form

$$V_d(P) = \frac{m^2 T^2 \left((2\pi - 3\theta)^2 - 27\psi^2\right)}{6\pi^2}. \tag{2.22}$$

The parameter m controls the location of the deconfinement transition in the pure gauge theory, and is set to 596 MeV. At low temperatures, this term dominates the pure gauge theory effective potential. The variable ψ is zero, and $V_d(P)$ is minimized when $\theta = 2\pi/3$. For this value of θ, the eigenvalues of P are uniformly spaced around the unit circle, respecting center symmetry, and $\mathrm{Tr}_F P = \mathrm{Tr}_F P^\dagger = 0$. As the temperature increases, $V_g(P)$ becomes relevant, and gives rise to the deconfined phase where center symmetry is spontaneously broken. The addition of light fundamental quarks via $V_f(P)$ explicitly breaks center symmetry. For all nonzero temperatures, center symmetry is broken and $\langle \mathrm{Tr}_F P \rangle \neq 0$. However, a remnant of the deconfinement transition remains in the form of a rapid crossover from smaller value of

$\mathrm{Tr}_F P$ to larger ones as T and μ are varied. Note that this simple model neglects both chiral symmetry breaking, relevant at low T and low μ and the formation of a color superconductor, which occurs at low T and high μ. Because the simplified model we are using does not treat chiral symmetry breaking, it should not be expected to reproduce exactly the features seen in lattice simulations. Nevertheless, comparison with PNJL model results, *e.g.*, [75], show that the model is quantitatively similar to the behavior of models with many more free parameters that include chiral symmetry effects. In the model studied here, $\mathrm{Tr}_F P$ shows a slightly larger initial rise in $\mathrm{Tr}_F P$ with temperature than does the model studied in Ref. [75]. This is consistent with the role that chiral symmetry breaking plays in diminishing the explicit breaking of $Z(3)$ symmetry by quarks. We plan to include the effects of chiral symmetry breaking in a PNJL-type treatment in a future work.

For a given T and μ, the free energy and other thermodynamic quantities are obtained from the saddle point of $V_{eff}(P)$. Figure 2.1 shows $\mathrm{Tr}_F P$ and $\mathrm{Tr}_F P^\dagger$ as functions of T at constant μ for values up to $\mu = 450\,\mathrm{MeV}$ for two flavors of massless quarks. There is a rapid crossover in $\mathrm{Tr}_F P$ and $\mathrm{Tr}_F P^\dagger$ for smaller values of μ that becomes less dramatic as μ increases. There is a small difference between $\mathrm{Tr}_F P$ and $\mathrm{Tr}_F P^\dagger$ in the crossover region when $\mu \neq 0$, with $\mathrm{Tr}_F P^\dagger > \mathrm{Tr}_F P$, indicating that it is easier to insert a heavy antiquark into the system than a heavy quark. Figure 2.2 shows $\mathrm{Tr}_F P$ and $\mathrm{Tr}_F P^\dagger$ as functions of μ at constant T for values up to $T = 250\,\mathrm{MeV}$. Similar behavior is obtained as that shown in Fig. 2.1, but the crossover is less abrupt and almost gone at $T = 250\,\mathrm{MeV}$. These results are consistent with more complicated models that include the effects of chiral symmetry and

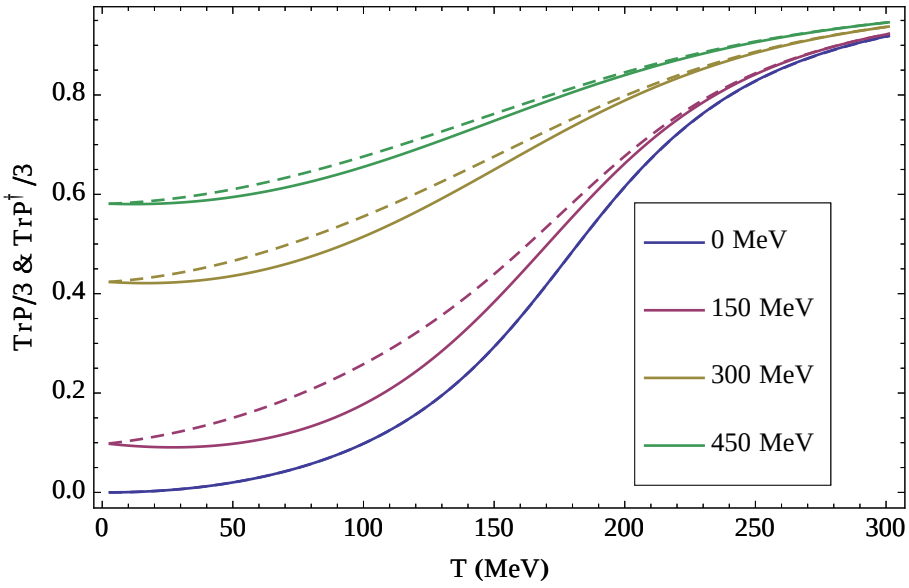

Figure 2.1: $\frac{1}{3}\mathrm{Tr}_F P$ (solid line) and $\frac{1}{3}\mathrm{Tr}_F P^\dagger$ (dotted line) as functions of T at constant μ for values up to $\mu = 450$ MeV with $N_f = 2$.

color superconductivity.

As discussed above, the mass matrix associated with the fields A_4^3 and A_4^8 has the property that the eigenvalues are either both real or form a complex conjugate pair. The most physically interesting region for this model occurs when T is larger than the $\mu = 0$ crossover temperature. In this region, we can safely assume that chiral symmetry is approximately restored, and the use of zero-mass quarks is a reasonable approximation. Working in this region also excludes color superconducting phases. Useful analytic results can be obtained in the region $T, \mu \gg m$, where the saddle point is given approximately by

$$\theta \approx \frac{3m^2\pi}{8\pi^2T^2 + 6\mu^2} \tag{2.23}$$

$$\psi \approx \frac{9m^4\pi^2T\mu}{4\left(4\pi^2T^2 + 3\mu^2\right)^3}. \tag{2.24}$$

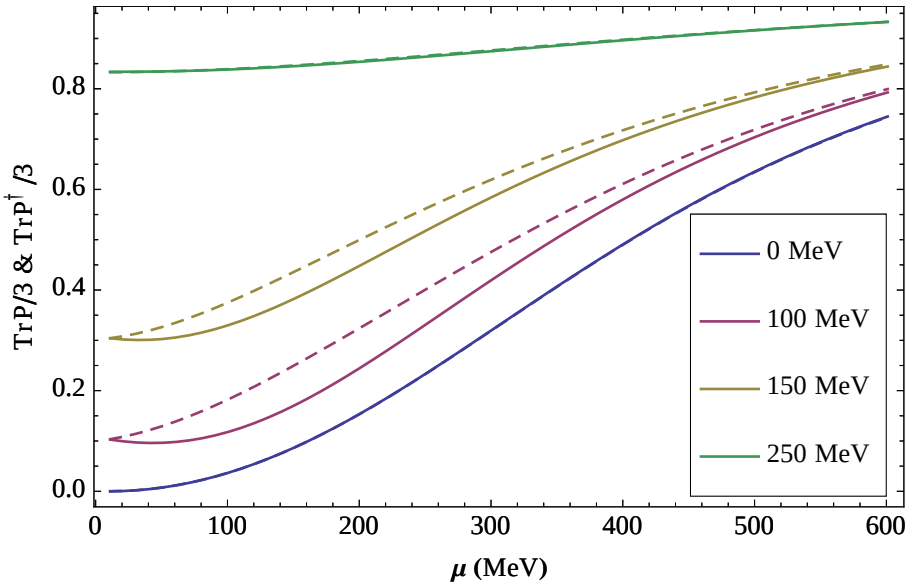

Figure 2.2: $\frac{1}{3}\mathrm{Tr}_F P$ (solid line) and $\frac{1}{3}\mathrm{Tr}_F P^\dagger$ (dotted line) as a function of μ at constant T for values up to $T = 250\,\mathrm{MeV}$ with $N_f = 2$.

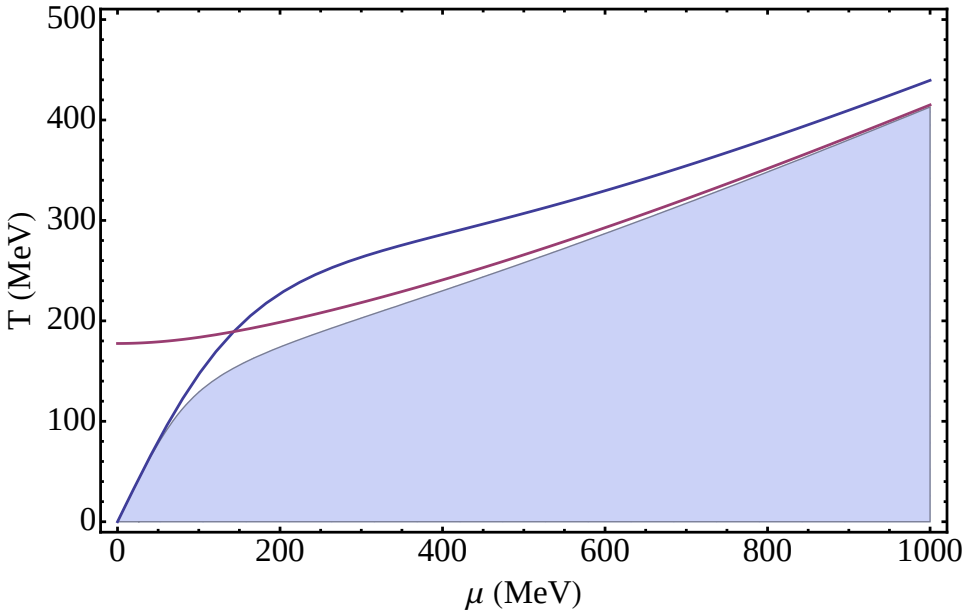

Figure 2.3: The shaded region of the $\mu - T$ plane indicates where the mass matrix is complex. High-T and low-T approximations to the boundary are also shown.

The corresponding mass matrix eigenvalues are given to order m^2 by

$$g^2\left(\frac{4T^2}{3}+\frac{\mu^2}{\pi^2}\right)+\frac{g^2m^2\left(9\mu^2-12\pi^2T^2\pm 2\pi T\sqrt{9\pi^2T^2-12\mu^2}\right)}{4\pi^2\left(3\mu^2+4\pi^2T^2\right)}, \tag{2.25}$$

a formula that combines the one-loop formula for the screening masses $g^2\left(4T^2/3+\mu^2/\pi^2\right)$ with corrections due to the confining term V_d in V_{eff} that are proportional to m^2. If $T > 2\mu/\sqrt{3}\pi$, there are two real, nondegenerate eigenvalues. However, if $T < 2\mu/\sqrt{3}\pi$, the two eigenvalues form a conjugate pair. The occurrence of such pairs is unusual in a Euclidean field theory, and is associated with the sign problem at finite density [70]. In a d-dimensional theory, a boson of mass m_B contributes a term

$$\frac{1}{2}\int\frac{d^dk}{(2\pi)^d}\log\left[k^2+m_B^2\right] \tag{2.26}$$

to the effective potential. A negative value for m_B^2 leads to an imaginary part for the effective potential, indicating instability, as would a complex value. However, in the case where there are complex conjugate pairs of mass eigenvalues where $m_B^2=a\pm ib$, the contribution of the two terms is now

$$\frac{1}{2}\int\frac{d^dk}{(2\pi)^d}\log\left[\left(k^2+a+ib\right)\left(k^2+a-ib\right)\right]=\frac{1}{2}\int\frac{d^dk}{(2\pi)^d}\log\left[\left(k^2+a\right)^2+b^2\right] \tag{2.27}$$

which is always positive, and thus shows no instability. However, correlation functions will in general exhibit modulated decay.

The occurrence of complex eigenvalues indicates periodic modulation in the spatial decay of color-color density correlation functions reminiscent of similar oscillations in density-density correlation functions in liquids. Figure 2.3 shows the region where the exact mass matrix is complex, along with high-T and low-T approximations to the boundary of the region. This result may depend strongly on the choice of V_d, an issue we plan to address in later work. Patel has suggested that a signal for such oscillatory behavior might appear in baryon number correlators in heavy ion collisions at RHIC and the LHC [76, 77]. Based on the results reported here, it would be more natural to observe this behavior in the CBM experiment at FAIR, but much work is needed to determine a useful experimental signature.

Chapter 3

COMPLEX SADDLE POINTS AND DISORDER LINES IN QCD AT FINITE TEMPERATURE AND DENSITY

This chapter contains the materials published under the same title [1]*. This work was done in collaboration with Dr. Hiromichi Nishimura under the supervision of my advisor, Prof. Michael Ogilvie*

3.1 Introduction

The phase structure of QCD at finite density and temperature is of fundamental importance, and can be studied experimentally, theoretically and via lattice simulations. Nevertheless, progress has been slow, in part because of the sign problem, which afflicts both phenomenological models and lattice simulations. The sign problem is found in many area of physics [41–43]. In QCD, the quark contribution to the partition function, given as a functional determinant dependent on the gauge field, is complex for typical gauge field configurations when the quark chemical potential μ is non-zero. It is natural to consider the analytically continuation of the gauge field into the complex plane. Some progress has been made in incorporating this idea into lattice simulations [55–60, 78]. Here we show that the consideration of complex saddle points provides a conceptually cohesive phenomenological model of QCD at finite T and μ. Our results can provide guidance for lattice simulations by indicating the behavior of the dominant field configuration, within a phenomenological framework. We

[1] Nishimura, H., Ogilvie, M.C. and Pangeni, K., 2015. Complex Saddle Points and Disorder Lines in QCD at finite temperature and density. Physical Review D, 91(5), p.054004.

will show that certain features of the saddle point appear to be independent of the choice of a particular phenomenological model. Moreover, we will identify a new property of QCD at finite density, the occurence of a disorder line, that may have observable consequences in experiment and/or lattice simulation. Some feature associated with the disorder line differentiate strongly between different phenomenological models, and may thus have an impact on our understanding of confinement.

The remainder of this paper is organized as follows. In section II, we provide a simple example based on the the $U(1)$ group that indicates the need for complex saddle points. Section III reviews the formalism first developed in our previous work [79]. We pay particular attention to the existence and consequences of an antilinear symmetry $\mathcal{CK}$ in finite density field theories, where $\mathcal{C}$ is charge conjugation and $\mathcal{K}$ is complex conjugation; in some sense this symmetry replaces charge conjugation symmetry when $\mu \neq 0$. The following section, section IV, describes the different phenomenological models we study using an effective potential for the Polyakov loop P and chiral condensate $\bar{\psi}\psi$. We do not consider other possible condensates in this work, such as the color superconducting condensate, deferring this to later work. A total of six different models are considered. We use two different models for the confining part of the effective potential, Model A and Model B, taken from [73]. We consider three cases of quarks, always with two flavors: heavy quarks, massless quarks with no chiral dynamics and a full treatment of light quarks, with chiral dynamics included via a bosonized four-fermion interaction. Our most realisitic models are therefore of Polyakov-Nambu-Jona Lasinio (PNJL) type, with the major new feature the consideration of complex

saddle points of the effective potential. Section V, VI and VII describe in detail the results for the three different cases of quarks. A final section offers conclusions.

3.2 Simple U(1) example

As an illustration of the role of analytic continuation in field space for models with non-zero chemical potential, we consider a single-site model, where a particle propagates in a closed loop in Euclidean time, always returning to the same lattice site. The model has a hopping parameter J, a dimensionless chemical potential μ and a $U(1)$ background field θ [80]. The partition function is

$$Z = \int \frac{d\theta}{2\pi} e^S \tag{3.1}$$

where

$$S = J\left[e^{\mu+i\theta} + e^{-\mu-i\theta}\right]. \tag{3.2}$$

The action S is complex, so Z has a sign problem. It is easy to find Z exactly by a strong-coupling expansion in J:

$$Z = \sum_{n=0}^{\infty} \frac{J^{2n}}{(n!)^2} = I_0(J), \tag{3.3}$$

where $I_0(J)$ is the modified Bessel function of order 0. Similar results can be obtained for expectation values such as $\left\langle e^{i\theta}\right\rangle$, which are zero-dimensional analogs of Polyakov loops. It is instructive to consider Z as a contour integral in the variable $z = \exp(i\theta)$:

$$Z = \int_{|z|=1} \frac{dz}{2\pi i z} \exp\left[Jze^{\mu} + Jz^{-1}e^{-\mu}\right]. \tag{3.4}$$

We ask if the contour $|z| = 1$ can be deformed to a contour C along which S is real. The contour C is given by the circle $|z| = e^{-\mu}$. Making a change of variable $\theta \to \theta + i\mu$, we recover exact results such as

$$\begin{aligned} Z &= I_0(J) \\ \left\langle e^{i\theta} \right\rangle &= e^{-\mu} \frac{I_1(J)}{I_0(J)} \\ \left\langle e^{-i\theta} \right\rangle &= e^{+\mu} \frac{I_1(J)}{I_0(J)}. \end{aligned} \tag{3.5}$$

We apply a saddle-point method to the original integral, looking for the saddle-point in the complex plane. The saddle point satisfies

$$e^{\mu} - e^{-\mu}/z^2 = 0 \tag{3.6}$$

so the saddle is at $i\theta = -\mu$. Returning to the original notation, we approximate Z by

$$Z \approx \int \frac{d\theta}{2\pi} \exp\left[2J - \frac{1}{2} 2J\theta^2\right] = \frac{e^{2J}}{\sqrt{4\pi J}} \tag{3.7}$$

which is the leading-order asymptotic behavior of $I_0(2J)$. A similar evaluation for the expectation values yields

$$\begin{aligned} \left\langle e^{i\theta} \right\rangle &\simeq e^{-\mu} \\ \left\langle e^{-i\theta} \right\rangle &\simeq e^{+\mu}. \end{aligned} \tag{3.8}$$

If we had used $Re(S) = J\left(e^{\mu} + e^{-\mu}\right)\cos\theta$ as a starting point for a steepest descents calculation, the result for Z would have been

$$\frac{e^{J\left(e^{\mu}+e^{-\mu}\right)}}{\sqrt{2\pi J\left(e^{\mu}+e^{-\mu}\right)}} \tag{3.9}$$

which does not represent the correct asymptotic behavior.

It is important to emphasize that neither a deformation of the contour into the complex plane nor the use of complex saddle points is required in an exact evaluation of Z and related quantities. However, many methods, from perturbation theory to importance sampling in lattice simulations, rely implicitly or explicitly on the existence of appropriate saddle points. In this simple $U(1)$ model, the use of complex saddle points naturally allows the expected values of the Polyakov loops for particle and antiparticles to be different: $\left\langle e^{i\theta}\right\rangle \neq \left\langle e^{-i\theta}\right\rangle$. In an exact calculation using a real contour for θ, this result must be recovered from rapid fluctuations in the integration. A saddle point approximation incorrectly using $Re(S)$ for the location of saddle points would have obtained $\left\langle e^{i\theta}\right\rangle = \left\langle e^{-i\theta}\right\rangle$ at leading order.

3.3 Formalism for SU(N) gauge theories at finite density

We now consider an $SU(N)$ gauge theory coupled to fermions in the fundamental representation. It is well-known that the Euclidean Dirac operator has complex eigenvalues when a non-zero chemical potential is introduced [41]. This can be understood as an explicit breaking of charge conjugation symmetry $\mathcal{C}$. The log of the fermion determinant, $\log\det(\mu, A)$, which is a function of the quark chemical potential μ and the gauge field A, can be formally

expanded as a sum over Wilson loops with real coefficients. For a gauge theory at finite temperature, the sum includes Wilson loops that wind non-trivially around the Euclidean timelike direction; Polyakov loops, also known as Wilson lines, are examples of such loops. At $\mu = 0$, every Wilson loop $\mathrm{Tr}_F W$ appearing in the expression for the fermion determinant is combined with its conjugate $\mathrm{Tr}_F W^\dagger$ to give a real contribution to path integral weighting. More formally, charge conjugation acts on matrix-valued Hermitian gauge fields as

$$\mathcal{C} : A_\mu \to -A_\mu^t \tag{3.10}$$

where the overall minus sign is familiar from QED, and the transpose interchanges particle and antiparticle, *e.g.*, W^+ and W^- in $SU(2)$. This transformation law in turn implies that $\mathcal{C}$ exchanges $\mathrm{Tr}_F W$ and $\mathrm{Tr}_F W^\dagger$ so unbroken charge symmetry implies a real fermion determinant. When $\mu \neq 0$, Wilson loops with non-trivial winding number n in the x_4 direction receive a weight $e^{n\beta\mu}$ while the conjugate loop is weighted by $e^{-n\beta\mu}$ and invariance under $\mathcal{C}$ is explicitly broken. However, there is a related antilinear symmetry which is unbroken: $\mathrm{Tr}_F W$ transforms into itself under the combined action of $\mathcal{CK}$, where $\mathcal{K}$ is the fundamental antilinear operation of complex conjugation. Thus the theory is invariant under $\mathcal{CK}$ even in the case $\mu \neq 0$. This symmetry is an example of a generalized $\mathcal{PT}$ (parity-time) symmetry transformation [69, 70]; theories with such symmetries form special class among theories with sign problems. For fermions, $\mathcal{CK}$ symmetry implies the well-known relation $\det(-\mu, A_\mu) = \det(\mu, A_\mu)^*$ for Hermitian A_μ, a relation which is often derived using a γ_5 transformation of the Dirac operator. The advantage of using $\mathcal{CK}$ is that it is more general,

leading to more insight into the sign problem and applying to bosons as well as to fermons. For example, it is easy to see that our simple zero-dimensional $U(1)$ model in the preceding section is invariant under the combined action of $\mathcal{K} : i \to -i$ and $\mathcal{C} : \theta \to -\theta$.

For phenomenological models, the existence of $\mathcal{CK}$ symmetry leads naturally to the consideration of complex but $\mathcal{CK}$-symmetric saddle points. $\mathcal{CK}$ symmetry will map any saddle-point configuration $A_\mu^{(1)}$ into another saddle point given by $A_\mu^{(2)} = -A_\mu^{(1)\dagger}$ with a corresponding connection between the actions of the two configurations: $S^{(2)} = S^{(1)*}$. However, some field configurations are themselves $\mathcal{CK}$-symmetric in that $-A_\mu^\dagger$ is equivalent to A_μ under a gauge transformation. If a saddle point is $\mathcal{CK}$ symmetric, then its action and effective potential are necessarily real. A quick direct proof can be given: For such a field configuration, it is easy to prove that every Wilson loop is real and thus $\det(\mu, A_\mu)$ is real and positive for a $\mathcal{CK}$-symmetric field configuration. If a single $\mathcal{CK}$-symmetric saddle point dominates the effective potential, then the sign problem is solved, at least for a particular phenomenological model. Such $\mathcal{CK}$-symmetric saddle points have been seen before in finite density calculations [61–64].

Let us consider the Polyakov loop P, a special kind of Wilson loop, associated with some particular field configuration that is $\mathcal{CK}$-symmetric. We can transform to Polyakov gauge where A_4 is diagonal and time-independent, and work with the eigenvalues θ_j defined by

$$P(\vec{x}) = \mathrm{diag}\left[e^{i\theta_1(\vec{x})}, \cdots, e^{i\theta_N(\vec{x})}\right] \tag{3.11}$$

where the θ_j's are complex but satisfy $\sum_j \theta_j = 0$. Because we are primarily interested in

constant saddle points, we suppress the spatial dependence hereafter. Invariance under $\mathcal{CK}$ means that the set $\left\{-\theta_j^*\right\}$ is equivalent to the $\{\theta_j\}$ although the eigenvalues themselves may permute. In the case of $SU(3)$, we may write this set uniquely as

$$\{\theta - i\psi, -\theta - i\psi, 2i\psi\}\,. \tag{3.12}$$

This parametrizes the set of $\mathcal{CK}$-symmetric $SU(3)$ Polyakov loops. Notice that both

$$\mathrm{Tr}_F P = e^{\psi} 2\cos\theta + e^{-2\psi} \tag{3.13}$$

and

$$\mathrm{Tr}_F P^\dagger = e^{-\psi} 2\cos\theta + e^{2\psi} \tag{3.14}$$

are real, but they are equal only if $\psi = 0$. In the usual interpretation of the Polyakov loop expectation value, this implies that the free energy change associated with the insertion of a fermion is different from the free energy change associated with its antiparticle. It is easy to check that the trace of all powers of P or $P^\dagger$ are all real, and thus all group characters are real as well. This parametrization represents a generalization of the Polyakov loop parametrization used in the application of mean-field methods to confinement, *e.g.*, in PNJL models [65] or in gauge theories with double-trace deformations [66, 67]. This parametrization can be generalized to include finite density models for arbitrary N.

The existence of complex $\mathcal{CK}$-symmetric saddle points provides a fundamental approach to non-Abelian gauge theories that is similar to the heuristic introduction of color chemical

potentials, and naturally ensures the system has zero color charge, *i.e.*, all three charges contribute equally [68]. In the case of $SU(3)$, extremization of the thermodynamic potential with respect to θ leads to the requirement $\langle n_r \rangle - \langle n_g \rangle = 0$ where $\langle n_r \rangle$ is red color density, including the contribution of gluons. Similarly, extremization of the thermodynamic potential with respect to ψ leads $\langle n_r \rangle + \langle n_g \rangle - 2 \langle n_b \rangle = 0$. Taken together, these two relations imply that $\langle n_r \rangle = \langle n_g \rangle = \langle n_b \rangle$.

We demand that any saddle point solution be stable to constant, real changes in the Polyakov loop eigenvalues, corresponding for $SU(3)$ to constant real changes in A_4^3 and A_4^8. Consider the $(N-1) \times (N-1)$ matrix M_{ab}, defined in Polyakov gauge as

$$M_{ab} \equiv g^2 \frac{\partial^2 V_{eff}}{\partial A_4^a \partial A_4^b}. \tag{3.15}$$

At very high temperatures and densities, the eigenvalues of this mass matrix give the usual Debye screening masses. The stability criterion is that the eigenvalues of M must have positive real parts. At $\mathcal{CK}$-symmetric saddle points, the eigenvalues will be either real or part of a complex conjugate pair. In the case of $SU(3)$, the matrix M may also be written in terms of derivatives with respect to θ and ψ as

$$M = \frac{g^2}{T^2} \begin{pmatrix} \frac{1}{4} \frac{\partial^2 V_{eff}}{\partial \theta^2} & \frac{i}{4\sqrt{3}} \frac{\partial^2 V_{eff}}{\partial \theta \partial \psi} \\ \frac{i}{4\sqrt{3}} \frac{\partial^2 V_{eff}}{\partial \theta \partial \psi} & \frac{-1}{12} \frac{\partial^2 V_{eff}}{\partial \psi^2} \end{pmatrix}. \tag{3.16}$$

This stability criterion generalizes the stability criterion used previously for color chemical potentials, which was $\partial^2 V_{eff}/\partial \psi^2 < 0$. Crucially, the mass matrix M_{ab} is invariant under

$M^* = \sigma_3 M \sigma_3$, which is itself a generalized $\mathcal{PT}$ (parity-time) symmetry transformation [69, 70]. It is easy to see that this relation implies that M_{ab} has either two real eigenvalues or a complex eigenvalue pair. In either case, the real part of the eigenvalues must be positive for stability. In the case where there are two real eigenvalues, we will denote by κ_1 and κ_2 the two positive numbers such that κ_1^2 and κ_2^2 are the eigenvalues of the mass matrix M_{ab}. If M_{ab} has two complex eigenvalues, we define two positive real numbers κ_R and κ_I such that $(\kappa_R \pm i\kappa_I)^2$ are the conjugate eigenvalues of M_{ab}. The border separating the region $\kappa_I \neq 0$ from the region $\kappa_I = 0$ is known as the disorder line [81–83]. In this case, it separates the region where the color density correlation function decays exponentially in the usual way from the region where a sinusoidal modulation is imposed on that decay.

We illustrate the working of $\mathcal{CK}$ symmetry using the well-known one-loop expressions for the effective potential of particles moving in a constant background Polyakov loop. The one-loop contribution to the effective potential of N_f flavors of fundamental fermions moving in a background gauge field A is given by

$$\beta \mathcal{V} V_{eff}^f = -N_f \log \left[\det \left(\mu, A\right)\right] \tag{3.17}$$

where det again represents the functional determinant of the Dirac operator and $\beta\mathcal{V}$ is the volume of spacetime. A compact expression for the effective potential of massless fermions when the eigenvalues of P are complex was derived using zeta function methods in [71]. The

finite temperature contribution to the effective potential from quarks is given by

$$V_f^T(P) = -2TN_f \int \frac{d^3k}{(2\pi)^3} \mathrm{Tr}_F \left[\log\left(1 + e^{\beta\mu - \beta\omega_k} P\right) + \log\left(1 + e^{-\beta\mu - \beta\omega_k} P^\dagger\right) \right] \tag{3.18}$$

where $\omega_k = +\sqrt{k^2 + m^2}$ with m the fermion mass. We have evaluated $V_f(P)$ analytically for the case of massless quarks [79]. The result for quarks in a $\mathcal{CK}$-symmetric $SU(3)$ background Polyakov loop is

$$V_f^T(\theta, \psi, \mathrm{T}, \mu) = N_f \left(v_f\left(\theta - i\psi - \frac{i\mu}{T}\right) + v_f\left(-\theta - i\psi - \frac{i\mu}{T}\right) + v_f\left(2i\psi - \frac{i\mu}{T}\right)\right) \tag{3.19}$$

where

$$v_f(\theta) = -\frac{4T^4}{\pi^2}\left(\frac{\theta^4}{48} - \frac{\pi^2\theta^2}{24} + \frac{7\pi^4}{720}\right). \tag{3.20}$$

Explicitly, this is

$$\begin{aligned} V_f^T(\theta, \psi, \mathrm{T}, \mu) &= -\frac{\mu^4}{2\pi^2} + T^2\left(-\mu^2 + \frac{2\theta^2\mu^2}{\pi^2} - \frac{6\mu^2\psi^2}{\pi^2}\right) + \frac{4T^3\left(\theta^2\mu\psi + \mu\psi^3\right)}{\pi^2} \\ &\quad + \frac{T^4\left(-7\pi^4 + 20\pi^2\theta^2 - 10\theta^4 - 60\pi^2\psi^2 + 60\theta^2\psi^2 - 90\psi^4\right)}{30\pi^2}. \end{aligned} \tag{3.21}$$

for two flavors of massless quarks. This is manifestly real. Because we are interested in the analytic continuation of Polyakov loop eigenvalues into the complex plane, we need expressions for the gauge bosons as well as for fermions. In our previous work, we have shown that for $SU(3)$

$$V_g(P) = \frac{T^4\left(135\left(\theta^2-3\psi^2\right)^2+180\pi^2\left(\theta^2-3\psi^2\right)+60\pi\theta\left(27\psi^2-5\theta^2\right)-16\pi^4\right)}{90\pi^2} \tag{3.22}$$

which is also manifestly real. Note that the valid range of θ is $(0,\pi)$ due to the appearance of 2θ as an eigenvalue in the adjoint representation. The one-loop effective potential is simply the sum of $V_g(\theta)$ and $V_f(\theta)$. As is the case when $\mu = 0$, the dominant saddle point remains at $\theta = 0$ when $\mu \neq 0$: the one-loop effective potential incorrectly predicts that QCD is always in the extreme deconfined phase with $\mathrm{Tr}_F P = \mathrm{Tr}_F P^\dagger = 3$ because there is no confinement mechanism included.

3.4 Models

We now consider a class of phenomenological models that combines the one-loop result with the effects of confinement for the case of $SU(3)$ gauge bosons and two flavors of quarks at finite temperature and density. The model is described by an effective potential which is the sum of three terms:

$$V_{eff}(P) = V_g(P) + V_f(P) + V_d(P). \tag{3.23}$$

The potential term $V_g(P)$ is the one-loop effective potential for gluons given by eqn. (3.22). The potential term $V_f\,(P)$ contains all quark effects, including the one-loop expression defined above in eqn. (3.18). The potential term $V_d\,(P)$ represents confinement effects. We will consider three different forms for $V_f\,(P)$ and two different forms for $V_d\,(P)$ for a total of six different models. The formulas and parameters we use for these models are summarized in

Tables 3.1 and 3.2.

The potential term $V_d(P)$ acts to favor the confined phase at low temperature and density [24, 66, 73, 74]. There are two different points of view that can be taken on this potential. In one view, $V_d(P)$ represents a deformation added to the original model, and hence the subscript d. In typical applications, the temperature T is taken to be large such that perturbation theory is reliable in the chromoelectric sector because the running coupling $g^2(T)$ is small. The deformation term is taken to respect center symmetry and is used to move between the confined and deconfined phases in a controlled way. The gauge contribution $V_g(P)$ favors the deconfined phase, and in the pure gauge theory ($N_f = 0$) the deconfinement transition arises out of the competition between $V_g(P)$ and $V_d(P)$. The confined phase arising in models of this type is known to be analytically connected to the usual low-temperature confined phase of $SU(3)$ gauge theory [66]. This point of view emphasizes analytic control at the price of deforming the original gauge theory by the addition of $V_d(P)$. In the second point of view, V_d is phenomenological in nature and models the unknown confining dynamics of the pure gauge theory. The parameters of $V_d(P)$ are set to reproduce the deconfinement temperature of the pure gauge theory, known from lattice simulations to occur at $T_d \approx 270\,\mathrm{MeV}$.

We will take the second point of view, using simple expressions for $V_d(P)$ that reproduces much of the thermodynamic behavior seen in lattice simulations of the pure gauge theory. The specific form used are Model A and Model B of [73]. In Model A, $V_d(P)$ can be written as

$$V_d^A(P) = \sum_{j,k=1}^{N} (1 - \frac{1}{N}\delta_{jk}) \frac{M_A^2}{2\beta^2} B_2\left(\frac{\Delta\theta_{jk}}{2\pi}\right) \tag{3.24}$$

where $\Delta\theta_{jk} = |\theta_j - \theta_k|$ are the adjoint Polyakov loop eigenvalues and B_2 is the second Bernoulli polynomial. This expression gives a simple quartic polynomial in the Polyakov loop eigenvalues for $V_g(P) + V_d^A(P)$ and thus can be thought of as a form of Landau-Ginsburg potential for the Polyakov loop eigenvalues. For the $SU(3)$ parametrization used here, $V_d^A(P)$ takes the simple form

$$V_d^A(P) = \frac{M_A^2 T^2 \left((2\pi - 3\theta)^2 - 27\psi^2\right)}{6\pi^2}. \tag{3.25}$$

The parameter M_A controls the location of the deconfinement transition in the pure gauge theory, and is set to 596 MeV. At low temperatures, this term dominates the pure gauge theory effective potential. The variable ψ is zero, and $V_d(P)$ is minimized when $\theta = 2\pi/3$. For this value of θ, the eigenvalues of P are uniformly spaced around the unit circle, respecting center symmetry, and $\mathrm{Tr}_F P = \mathrm{Tr}_F P^\dagger = 0$. As the temperature increases, $V_g(P)$ becomes relevant, and gives rise to the deconfined phase where center symmetry is spontaneously broken. The addition of light fundamental quarks via $V_f(P)$ explicitly breaks center symmetry. For all nonzero temperatures, center symmetry is broken and $\langle \mathrm{Tr}_F P \rangle \neq 0$. However, a remnant of the deconfinement transition remains in the form of a rapid crossover from

smaller value of $\mathrm{Tr}_F P$ to larger ones as T and μ are varied. We also use Model B, defined as

$$V_d^B(P) = -\frac{T}{R^3}\log\left[\prod_{j<k}\sin^2\left(\frac{\theta_j-\theta_k}{2}\right)\right]. \tag{3.26}$$

This form for V_d is motivated by Haar measure, representing a determinantal term that tries to keep a space-time volume of order βR^3 confined. For the $SU(3)$ parametrization, $V_d^B(P)$ takes the form

$$V_d^B(P) = -\frac{T}{R^3}\log\left[\frac{1}{4}\left\{\cos\theta - \cosh\left(3\psi\right)\right\}^2\sin^2\theta\right]. \tag{3.27}$$

In order to reproduce the correct deconfinement temperature for the pure gauge theory, R must be set to $R = 1.0028$ fm. We plot the Polyakov loop for both Model A and Model B in Fig. 3.1.

Although V_d^A and V_d^B appear to be very different, and are motivated in different ways, they are actually closely related. The deformation potential V_d^A can also be written as

$$V_d^A = \frac{M_A^2T^2}{2\pi^2}\sum_{n=1}^{\infty}\frac{1}{n^2}\mathrm{Tr}_A P^n \tag{3.28}$$

while V_d^B can be written as

$$V_d^B = \frac{T}{R^3}\sum_{n=1}^{\infty}\frac{1}{n}\mathrm{Tr}_A P^n. \tag{3.29}$$

Using $\mathrm{Tr}_A P = \mathrm{Tr}_F P^n \mathrm{Tr}_F P^{\dagger n} - 1$, it is easy to prove that minimizing either V_d^A or V_d^B yields a confining phase where $\mathrm{Tr}_F P^n = 0$ for all $n \neq 0 \,\mathrm{mod}(N)$.

We consider three different cases of quarks. The first is heavy quarks, with a fixed mass

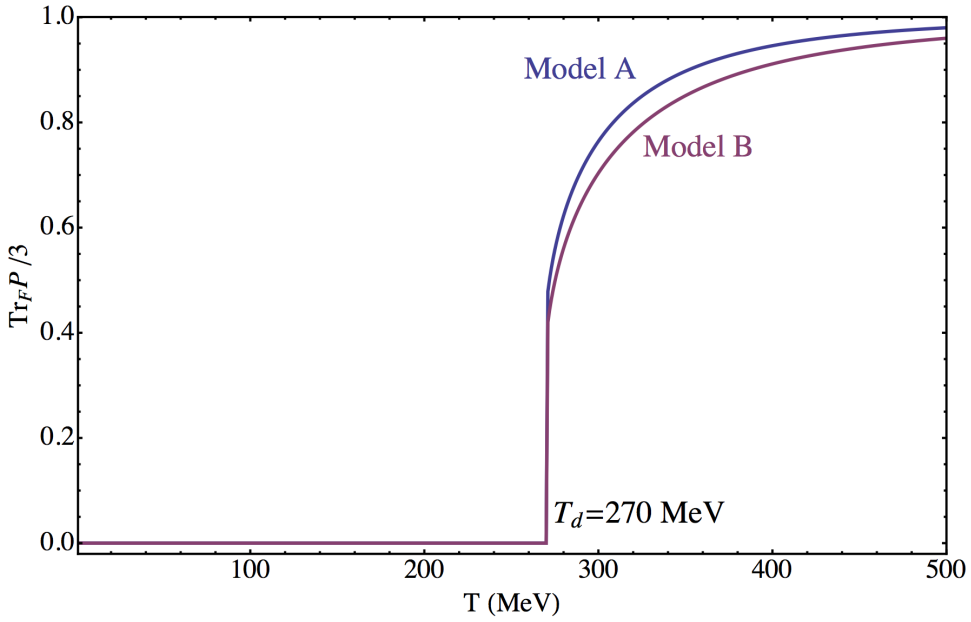

Figure 3.1: $\langle \mathrm{Tr}_F P \rangle$ as a function of T for pure $SU(3)$ with Model A and Model B for confinement effects.

of 2 GeV. The form of $V_f(P)$ is precisely that of Eq. (3.18) with the fermion mass set to a large value. In this model, the quarks are essentially irrelevant for the deconfinement transition, which occurs at essentially the same temperature as if no quarks were present at all. The effect of spontaneous chiral symmetry breaking is not included, as it would only contribute a small amount to the quark mass. This case is in some sense the simplest, and perhaps would be the easiest for which to obtain reliable simulation results. The second case considered is massless quarks, where the fermion mass in Eq. (3.18) is set equal to zero. This case cannot be easily simulated using lattice methods, because it ignores chiral symmetry breaking effects which do occur in lattice simulations. It is thus useful only for sufficiently large values of T and μ such that chiral symmetry is essentially restored. Our most realistic treatment of quarks uses a Nambu-Jona Lasinio four-fermion interaction to model chiral

Model of confinement	Confining potential V_d	Parameter
A	Eq. (3.25)	$M_A = 596$ MeV
B	Eq. (3.27)	$R = 1.0028$fm

Table 3.1: Potential term and parameters for modeling confinement effects. Parameters are determined from the deconfinement temperature for pure $SU(3)$ gauge theory.

Model of $N_f = 2$ fermions	Quark potential V_f	m_0	g_S	Λ
Heavy Quarks	Eq. (3.40)	2000 MeV	0	-
Massless Quarks	Eq. (3.21)	0	0	-
PNJL	Eq. (3.38) + Eq. (3.40)	5.5 MeV	5.496 GeV^{-2}	631.4 MeV

Table 3.2: Potential term and parameters for quark sector. All numerical values are for two-flavor QCD.

symmetry breaking effects, so these models are of Polyakov-Nambu-Jona Lasinio (PNJL) type [65].

In our PNJL models, we write the fermionic part of the partition function as

$$Z_f = \int \mathcal{D}\bar{\psi}\mathcal{D}\psi e^{i\int d^4x\,\mathcal{L}_f} \tag{3.30}$$

using $N_f = 2$ Nambu-Jona-Lasinio-type Lagrangian with the constant Polyakov loop [65]

$$\mathcal{L}_f = \bar{\psi}(i\gamma\cdot D - m_0)\psi + g_S\left\{\left(\bar{\psi}\psi\right)^2 + \left(\bar{\psi}i\gamma_5\lambda^a\psi\right)^2\right\} \tag{3.31}$$

where m_0 is the current mass of the quarks, g_S is the four-fermion coupling, and λ^a's are the generators of the flavor symmetry group $SU(2)$. The covariant derivative D_μ couples the fermions to a background Polyakov loop via the component of the gauge field in the

temporal direction. Introducing auxiliary fields, a scalar field σ and triplet of pseudoscalar fields π^a,

$$\mathcal{L}_{aux} = -g_S \left\{\sigma^2 + (\pi^a)^2\right\} + 2g_S\bar{\psi}\left\{\sigma + i\gamma_5\lambda^a\pi^a\right\}\psi, \tag{3.32}$$

and integrating over the fermion fields, we can write the partition function in terms of the boson fields (i.e. bosonization)

$$Z_f = \int \mathcal{D}\sigma\mathcal{D}\pi^a \exp\left[i\int d^4x \left\{\mathrm{tr}\log\left[i\gamma\cdot D - m_0 + 2g_S(\sigma + i\pi^a\lambda^a)\right] - g_S\left(\sigma^2 + (\pi^a)^2\right)\right\}\right]. \tag{3.33}$$

We use the background field method for the scalar field, $\sigma(x) = \sigma_0 + s(x)$ and write the partition function as

$$Z_f = \exp\left[i\int d^4x \left\{\mathrm{tr}\log\left[i\gamma\cdot D - m\right] - g_S\sigma_0^2\right\}\right]\int \mathcal{D}s\mathcal{D}\pi^a \exp\left[i\int d^4x\,\mathcal{L}_b\right] \tag{3.34}$$

where $m = m_0 - 2g_S\sigma_0$ is the constituent quark mass m , tr denotes the trace over the color, flavor, and Dirac space, and the bosonized Lagrangian is

$$\mathcal{L}_b = \mathrm{tr}\log\left[1 + \frac{1}{i\gamma\cdot D - m}2g_S(s + i\pi^a\lambda^a)\right] - g_S\left(s^2 + (\pi^a)^2\right). \tag{3.35}$$

We perform a Wick rotation and consider the theory in Euclidean space from now on. The first term in the partition function (3.34) gives the effective potential,

$$V_f = V_f^T(P, m) + V_f^0(m, m_0), \tag{3.36}$$

which consists of the finite-temperature part V_f^T, which is given by Eq. (3.18) and the vaccum part V_f^0,

$$V_f^0(m, m_0) = \frac{(m-m_0)^2}{4g_S} - 2N_f \mathrm{Tr}_F \int \frac{d^3k}{(2\pi)^3}\omega_k. \tag{3.37}$$

We note that the finite-temperature contribution V_f^T is finite for any values of P, m, μ, and T, while the zero-point energy, the integral in V_f^0, is divergent and needs a regularization. We use a noncovariant three-dimensional cutoff, Λ [84] and write it as [85]

$$\begin{aligned} V_f^0(m, m_0) &= \frac{(m-m_0)^2}{4g_S} - \frac{N_c N_f \Lambda^4}{8\pi^2}\left\{\sqrt{1+(m/\Lambda)^2}\left[2+(m/\Lambda)^2\right]\right. \\ &\left. +(m/\Lambda)^4 \log\frac{m/\Lambda}{1+\sqrt{1+(m/\Lambda)^2}}\right\}. \end{aligned} \tag{3.38}$$

For V_f^T, it is often convenient to combine the arguments of the logarithms into a single product that is manifestly real. Using Eq. (3.18), we can write the finite-temperature effective potential in terms of Polyakov loop eigenvalues as

$$\begin{aligned} V_f^T &= -2TN_f \sum_{j=1}^{N_c} \int \frac{d^3k}{(2\pi)^3}\left[\log\left(1+e^{-(\omega_k-\mu)/T+i\theta_j}\right)+\log\left(1+e^{-(\omega_k+\mu)/T-i\theta_j}\right)\right] \\ &= -2TN_f \int \frac{d^3k}{(2\pi)^3}\left\{\log\left[1+2\cos\theta\, e^{-(\omega_k-\mu)/T+\psi}+e^{-2(\omega_k-\mu)/T+2\psi}\right]\right. \qquad (3.39) \\ &\left. +\log\left[1+e^{-(\omega_k-\mu)/T-2\psi}\right]+(z\to -z)\right\} \qquad (3.40) \end{aligned}$$

where the last part denotes the antiparticle contribution which has the opposite sign for the chemical potential and the Polyakov loop eigenvalues, $z = \mu - igA_\mu$. From this expression, we can see explicitly that the one-loop fermionic effective potential at the complex saddle

point is real, independent of any approximation. We use Eqs. (3.38) and (3.40) for the effective potential of the fermionic part of PNJL model with the $T = 0$ parameters taken from [86].

In principle, the coupling of P and $\bar{\psi}\psi$ which is a prominent feature of PNJL models can lead to an extended mass matrix that incorporates mixing of $\bar{\psi}\psi$ with excitations of the Polyakov loop. The kinetic term of the scalar field s in the bosonized Lagrangian is needed for a full treatment. Using the log expansion and the derivative expansion for Eq. (3.35) [84, 87], we can obatin the kinetic term for the scalar field in the form

$$\mathcal{L}_b \supset 4N_f g_S^2 \mathrm{Tr}_F I_s^{\mu\nu} \partial_\mu s \partial_\nu s$$

where $I_s^{\mu\nu}$ is, for example, given as the momentum integral in Eq. (7.54) of [84] but the four-momentum k_μ is replaced by $k_\mu + gA_4\delta_{\mu 4}$ for the PNJL model. Using the identity

$$\int \frac{d^3k}{(2\pi)^3} k_i k_j = \int \frac{d^3k}{(2\pi)^3} \frac{k^2 \delta_{ij}}{3}$$

and rescaling s for the physical constituent mass, we can write the spatial part of the kinetic term as

$$\mathcal{L}_b \supset \frac{1}{2} I_s \left[\partial_i \left(-2g_S s\right)\right]^2$$

with

$$I_s = N_f T \sum_{n=-\infty}^{\infty} \int \frac{d^3k}{(2\pi)^3} \mathrm{Tr}_F \left[\left\{ \frac{2}{\left[(\omega_n + iz)^2 + \omega_k^2 \right]^2} - \frac{\frac{4}{3}k^2 + 4m^2}{\left[(\omega_n + iz)^2 + \omega_k^2 \right]^3} + \frac{\frac{16}{3}k^2 m^2}{\left[(\omega_n + iz)^2 + \omega_k^2 \right]^4} \right\} + (z \to -z) \right] \tag{3.41}$$

where $z = \mu - igA_4$ and the summation is over the Matsubara frequencies, $\omega_n = (2n+1)\pi$. A similar expression for I_s is obtained in [88] for the PNJL model. We first use the prescription (3.12) for the Polyakov loop and sum over the Matsubara frequencies and integrate over the three-momentum in Eq. (3.41). However, the integral is divergent, and we use the same non-covariant three-dimensional cutoff Λ used for the zero-point energy (3.38). With the s kinetic term given in terms of I_s, we can in principle compute the eigenvalues of an extended mass matrix. It turns out, however, that the off-diagonal coupling of the chiral component of the mass matrix is numerically negligible compared to the Polyakov-loop parts of the mass matrix, and thus we ignore the chiral component in the remainder of this paper.

3.5 Heavy quarks

We consider the case of heavy quarks propagating in constant Polyakov loop background. For such quark, the chiral symmetry effects are negligible and a first-order deconfinement transition line is the only true critical behavior found in the phase diagram. Our study of heavy quarks is perhaps most relevant for lattice studies of static quarks at non-zero μ; this approximation is particularly tractable [89].

The center symmetry of pure gauge theory is exact for infinitely heavy quarks. However,

quarks with finite mass break the center symmetry explicitly and weaken the first order transition of pure gauge theory. At sufficiently low quark mass the first order transition for deconfinement vanishes at a critical end point. The location of this critical end point is model dependent and has been proposed as a useful way to differentiate between different models of confinement [90]. In both Model A and Model B, the first order deconfinement transition vanishes for quark mass of around 1.5 GeV or less. Therefore we set the quark mass to be 2 GeV so that the deconfinement transition still persists. The end point of the deconfinement transition line lies at smaller values of μ, and appears to play no direct role in the behavior of ψ and κ_I. The quark mass is large compared to the confinement scale, so asymptotic freedom applies in the region $\mu \simeq m$. In this region, perturbation theory is a reliable guide when $T \gg T_d$, the pure gauge deconfinement temperature. However, below T_d, non-perturbative confinement effects cannot be neglected, hence the importance of the potential term V_d beyond what is usually considered the confining region at low T and μ. A useful expansion for $\beta\,(m-\mu) \gg 1$ for can be generated by expanding the logarithm in Eq. (3.18) and integrating term by term [72]. Such an expansion gives

$$V_f\,(P) = \sum_{n=1}^{\infty} \frac{(-1)^n m^2 T^2}{n^2 \pi^2} K_2(n\beta m)(e^{\frac{n\mu}{T}} \mathrm{Tr}_F P^n + e^{-\frac{n\mu}{T}} \mathrm{Tr}_F P^{\dagger n}). \tag{3.42}$$

At low temperature and density the effects of heavy quarks can be obtained approximately from the $n = 1$ term of Eq. (3.42). However, this expansion fails in the high density region ($\mu > 1.5$ GeV) in case of Model A as can be seen in Fig. 3.6. In our analysis we have therefore numerically integrated the full one loop expression for heavy quark potential.

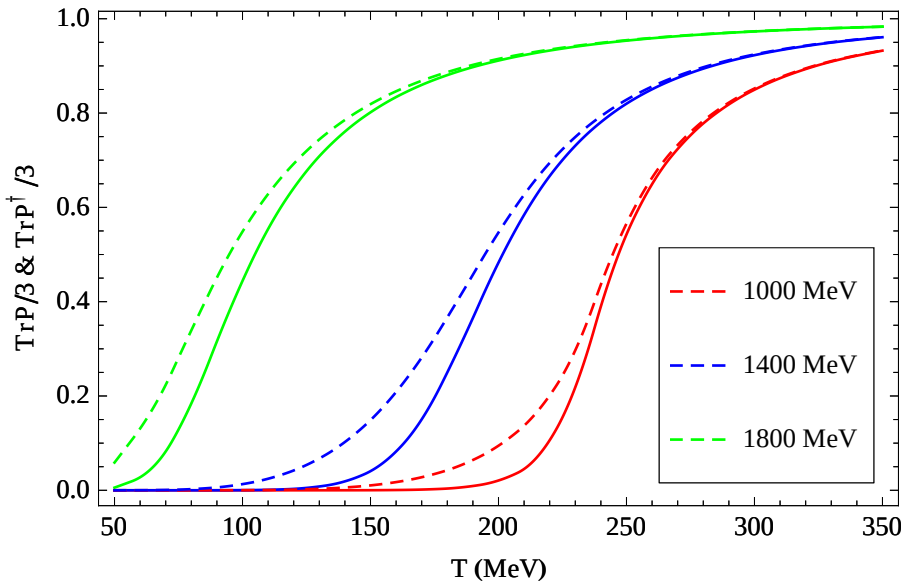

Figure 3.2: $\langle \mathrm{Tr}_F P \rangle$ and $\langle \mathrm{Tr}_F P^\dagger \rangle$ as a function of T for $\mu = 1000$, 1400 and 1800 MeV for heavy quarks using Model A for confinement effects. The Polyakov loops are normalized to one as the temperature becomes large.

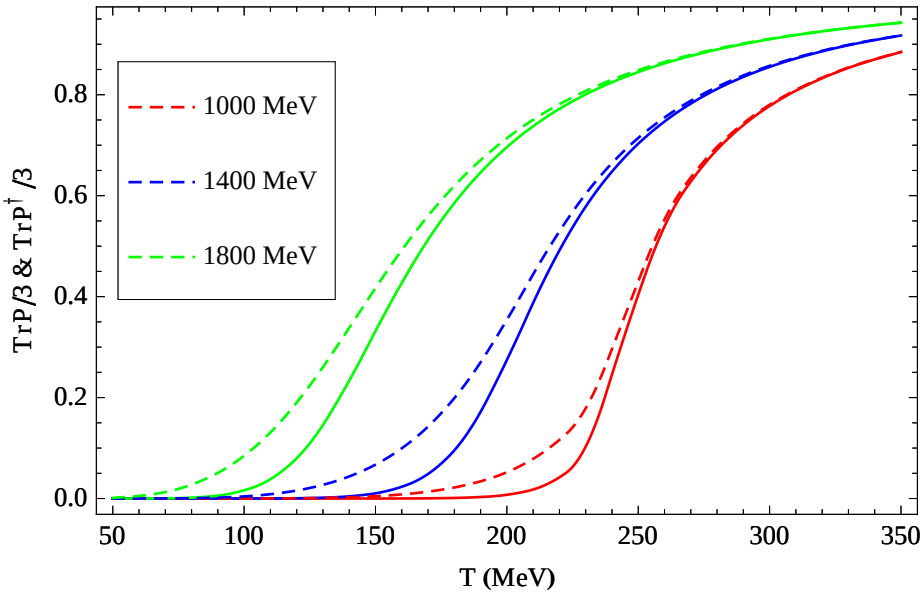

Figure 3.3: $\langle \mathrm{Tr}_F P \rangle$ and $\langle \mathrm{Tr}_F P^\dagger \rangle$ as a function of T for $\mu = 1000$, 1400 and 1800 MeV for heavy quarks using Model B for confinement effects. The Polyakov loops are normalized to one as the temperature becomes large.

In Fig. 3.2 we show $\mathrm{Tr}_F P$ and $\mathrm{Tr}_F P^\dagger$ as a function of T for various values of μ when the heavy quark has a mass of 2 GeV. In aggreement with our general argument above, the crossover moves toward lower values of T as μ increases. The separation between $\mathrm{Tr}_F P$ and $\mathrm{Tr}_F P^\dagger$ is largest in the crossover region, and is negligible at higher temperatures. As shown in the figure, the separation is largest for some intermediate value of μ less than the heavy quark mass. The behavior of $\mathrm{Tr}_F P$ and $\mathrm{Tr}_F P^\dagger$ for Model B is similar to Model A, as may be seen from Fig. 3.3. The crossover happenes at higher temperature for Model B, showing that the confining effect for Model B is smaller than Model A. Because ψ is non-zero in both models, there is a difference between $\mathrm{Tr}_F P$ and $\mathrm{Tr}_F P^\dagger$.

In Fig. 3.4, we show for Model A a contour plot for ψ along with a shaded region showing where $\kappa_I \neq 0$. The boundary of the shaded region is thus the disorder line. From this graph, we see that values of ψ are very small, but peak in a region centered roughly around $\mu = 1500$ MeV and $T = 150$ MeV. There is no obvious relation between the region where ψ is largest and the region where $\kappa_I \neq 0$. However, the peak in ψ is located near the point where the disorder line abruptly changes.

Figure 3.5 again shows the region where $\kappa_I \neq 0$ and the associated disorder line, but now with contour lines for κ_I added. As with all the contour plots of this type, we have set the running coupling $\alpha_s(T, \mu) = 1$. In other words, conversion to the actual one-loop values requires multiplying these values by appropriate values for $\sqrt{\alpha_s(T, \mu)}$. The region where the mass eigenvalues κ_1 and κ_2 form a complex conjugate pair has a complicated shape. The mass matrix eigenvalues are real for μ below about 600 MeV. There is a roughly rectangular

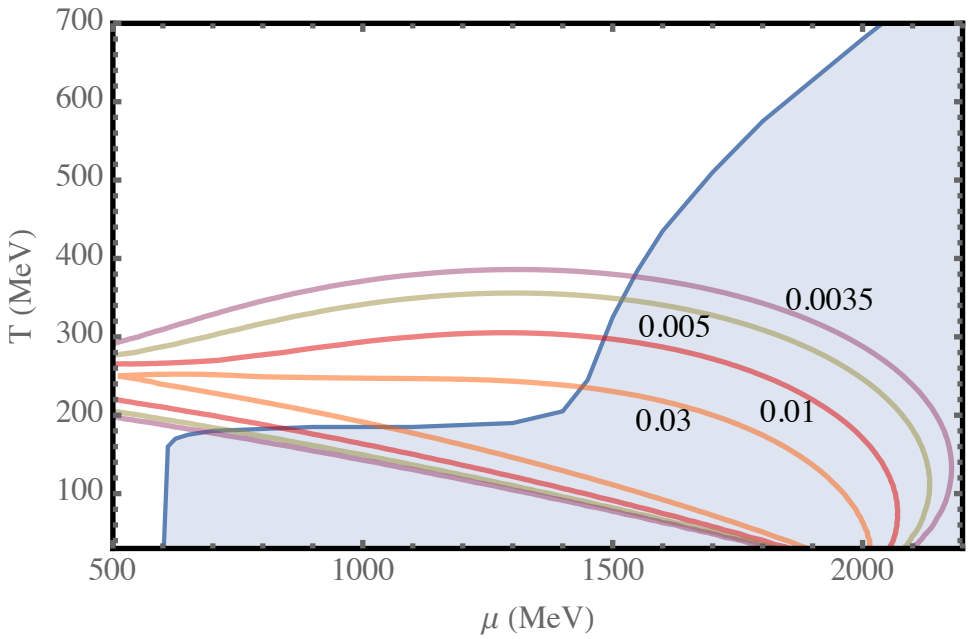

Figure 3.4: Contour plot of ψ in the $\mu - T$ plane for heavy quarks ($m = 2000\,\mathrm{MeV}$) using Model A for confinement effects. The region where $\kappa_I \neq 0$ is shaded.

region for $600\,\mathrm{MeV} \lesssim \mu \lesssim 1450\,\mathrm{MeV}$. This is followed by a region where the boundary rises roughly linearly with μ , similar to the behavior of Model A with massless quarks.

Figure 3.6 shows the physics associated with this behavior. The boundary using the complete one-loop expression is compared with both the massless boundary and the boundary obtained using the $n = 1$ approximation from Eqn. 3.42 to the full one-loop expression. As may be seen, the $n = 1$ term accounts very well for the low-temperature behavior of the boundary, while the massless quark result is accurate for μ above the heavy quark mass. It is clear that the abrupt change of the shaded region represents a rapid crossover from the behavior of a heavy quark to the behavior of a massless quark, occuring over a range of roughly $3M/4 < \mu < 5M/4$, with most of the change occuring before μ reaches M .

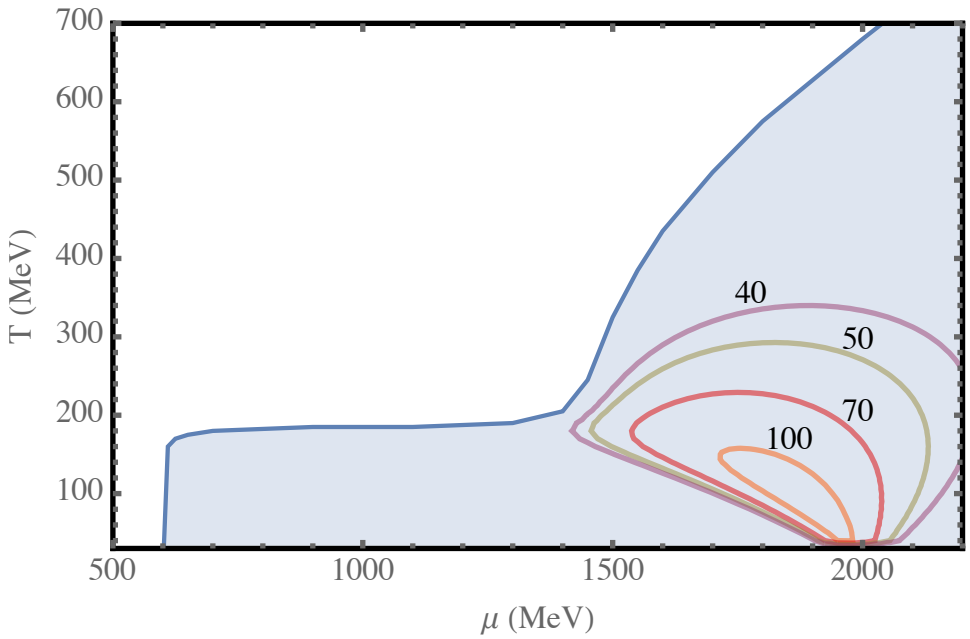

Figure 3.5: Contour plot of κ_I in the $\mu - T$ plane for heavy quarks ($m = 2000\,\text{MeV}$) using Model A for confinement effects. Contours are given in MeV with α_S set to one. The region where $\kappa_I \neq 0$ is shaded.

The behavior of ψ for Model B, as shown in Figure 3.7, is similar to the behavior of ψ for Model A, but the values of ψ are somewhat larger. The region where the eigenvalues of the mass matrix are complex is shown in Fig. 3.8. The shape and size of the region is very similar to the rectangular region found for Model A in Fig. 3.5. However, in the high-temperature region, where μ is greater than the quark mass, the region of complex mass eigenvalues is completely missing for Model B. This is consistent with the behavior of Model B for massless quarks, where no complex eigenvalues of the mass matrix were found.

Figure 3.9 shows a comparison of the regions where κ_I is non-zero for both Model A and Model B. Their shape is very similar for smaller values of μ, suggesting that some universal behavior occurs in this region. However, the behavior is very different in the region where

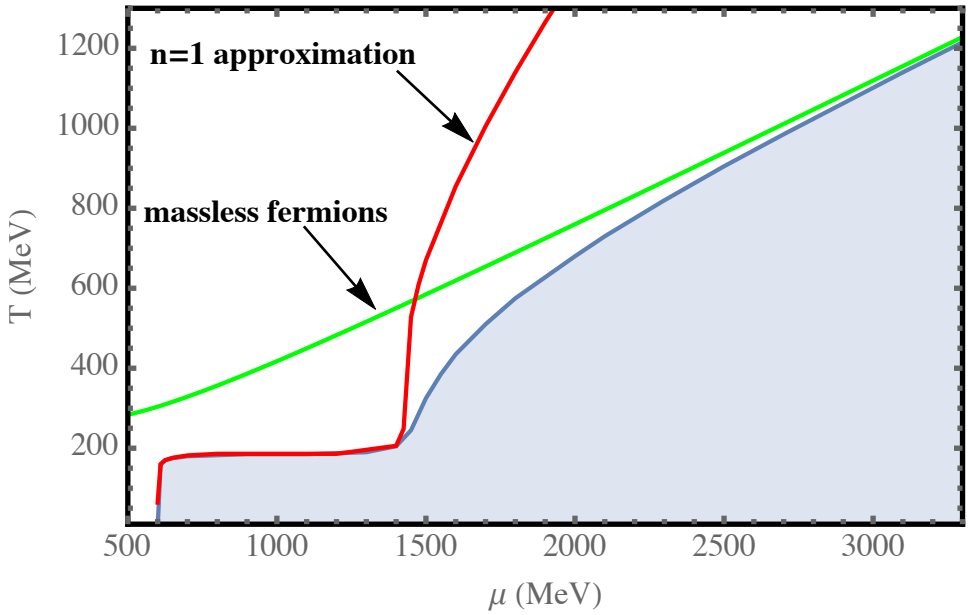

Figure 3.6: The shaded region indicates where $\kappa_I \neq 0$ for heavy quarks ($m = 2000\,\text{MeV}$) using Model A for confinement effects. The boundary of this region is also shown using an approximation appropriate for very heavy quarks ($\beta m \gg 1$) as well as for massless quarks, appropriate when $\beta m \ll 1$.

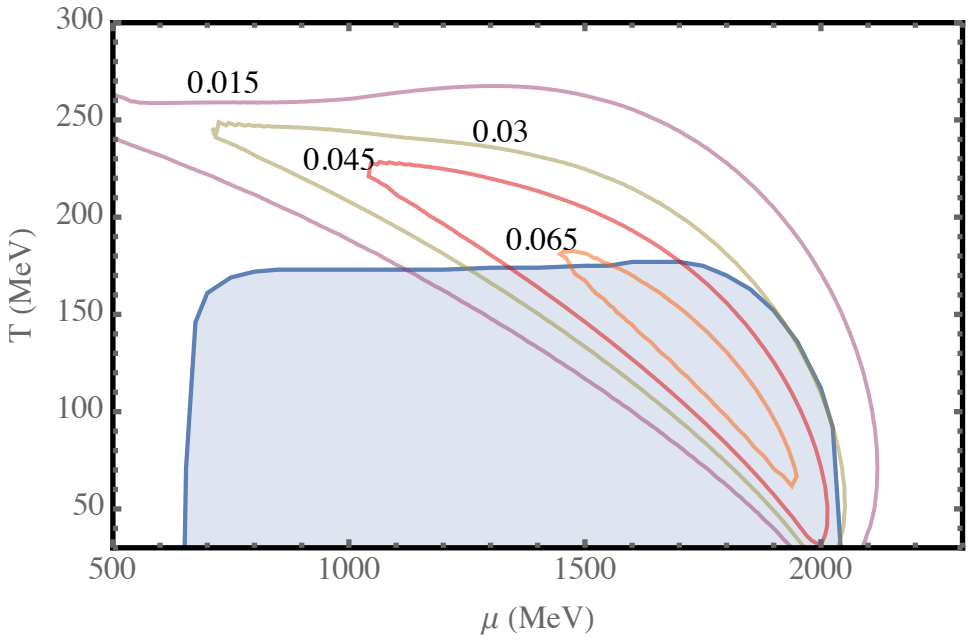

Figure 3.7: Contour plot of ψ in the $\mu - T$ plane for heavy quarks ($m = 2000\,\text{MeV}$) using Model B for confinement effects. The region where $\kappa_I \neq 0$ is shaded.

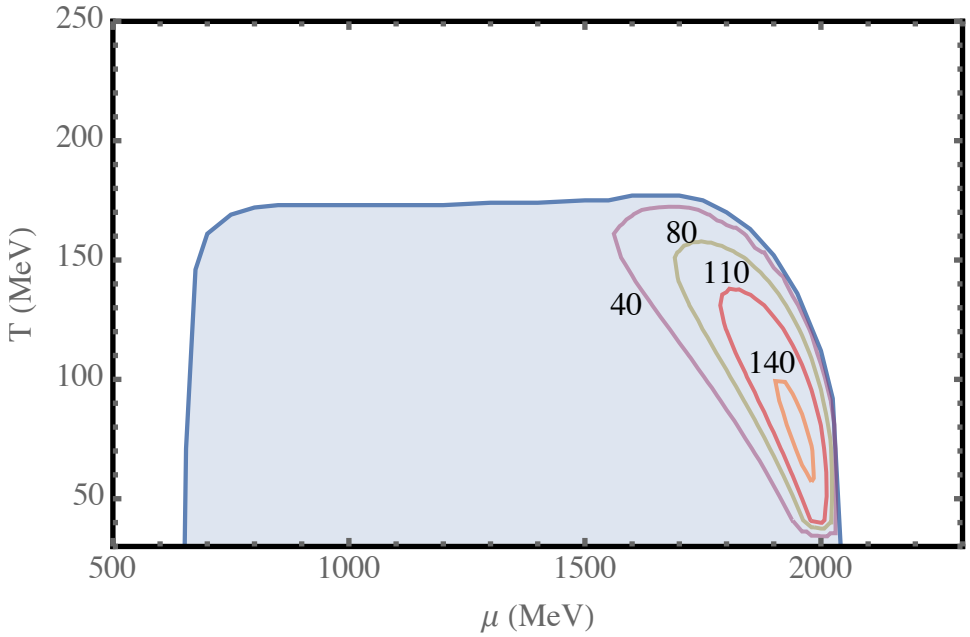

Figure 3.8: Contour plot of κ_I in the $\mu - T$ plane for heavy quarks ($m = 2000\,\text{MeV}$) using Model B for confinement effects. Contours are given in MeV with α_S set to one. The region where $\kappa_I \neq 0$ is shaded.

both T and μ are becoming large. Model A shows a continuation of the disorder line that follows the behavior for massless quarks, while for Model B the disorder line covers a finite region in $\mu - T$ space.

3.6 Massless quarks without chiral effects

In this section we extend the results of our previous work on massless quarks using Model A [79], including more detail and providing a comparison with Model B. This simple model where the quark mass m is set to zero neglects chiral symmetry breaking, relevant at low T and low μ. It should not be expected to reproduce exactly the features seen in lattice simulations. Nevertheless, comparison with PNJL model results, *e.g.*, [75], show that the

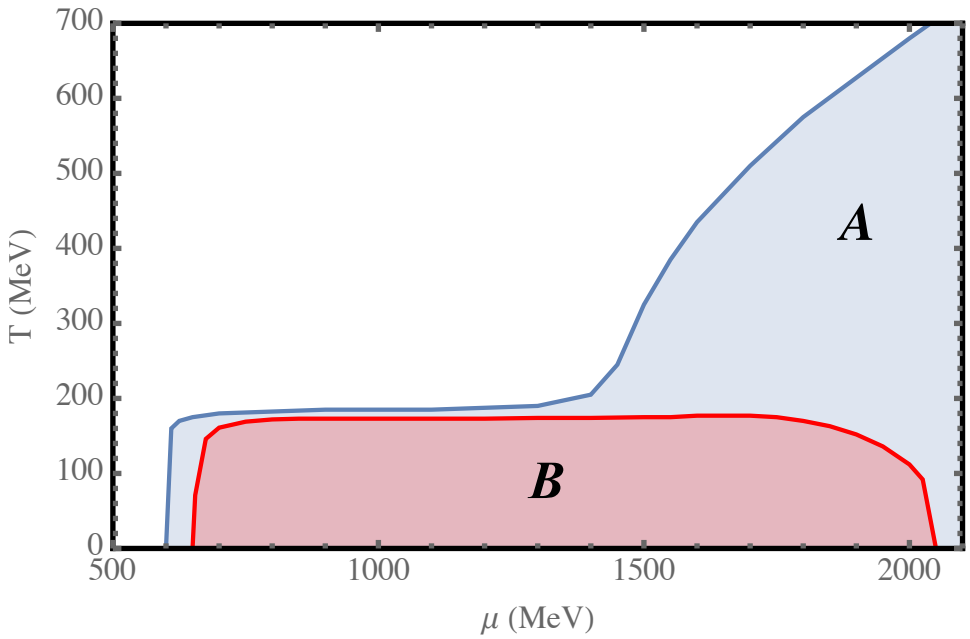

Figure 3.9: A comparison of the regions where $\kappa_I \neq 0$ for heavy quarks with Model A and Model B along with the corresponding disorder lines.

model is quantitatively similar to the behavior of models with many more free parameters that include chiral symmetry effects. For Model A, $\mathrm{Tr}_F P$ shows a slightly larger initial rise in $\mathrm{Tr}_F P$ with temperature than does the model studied in [75]. This is consistent with the role that chiral symmetry breaking plays in diminishing the explicit breaking of $Z(3)$ symmetry by quarks.

Figure 3.10 shows the region for Model A where κ_I is non-zero superimposed on a contour plot of ψ, while 3.11 shows contour lines for κ_I. Comparison of the two figures shows that the peak in ψ occurs at a lower value of μ than the peak in κ_I, with the peak in ψ occuring near ($\mu = 200$ MeV, $T = 110$ MeV). The behavior of the disorder line for large T and μ is

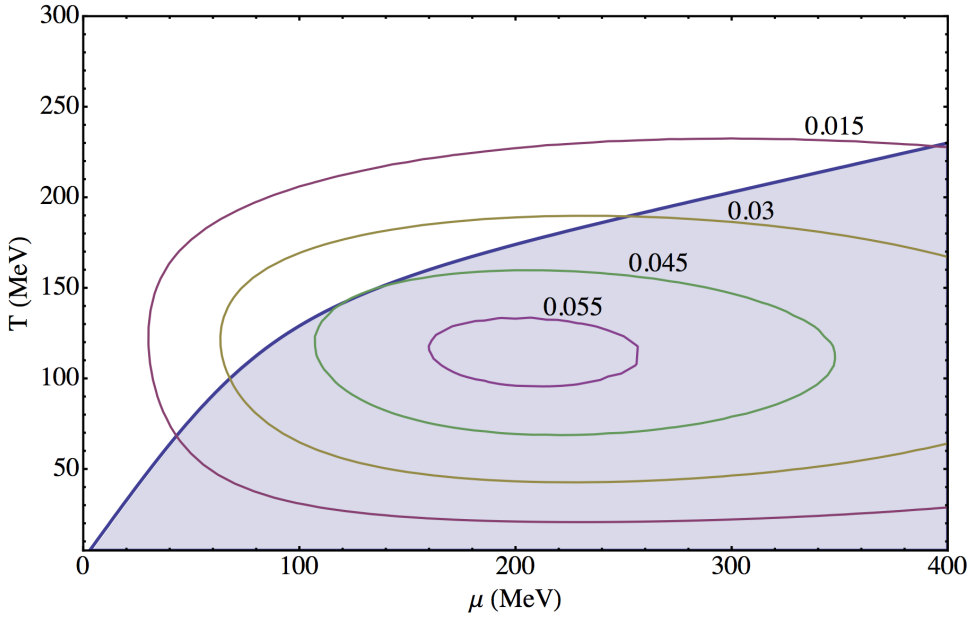

Figure 3.10: Contour plot of ψ in the $\mu - T$ plane for Model A with massless quarks, showing where $\mathrm{Tr}_F P$ is most different from $\mathrm{Tr}_F P^\dagger$. The region where $\kappa_I \neq 0$ is shaded.

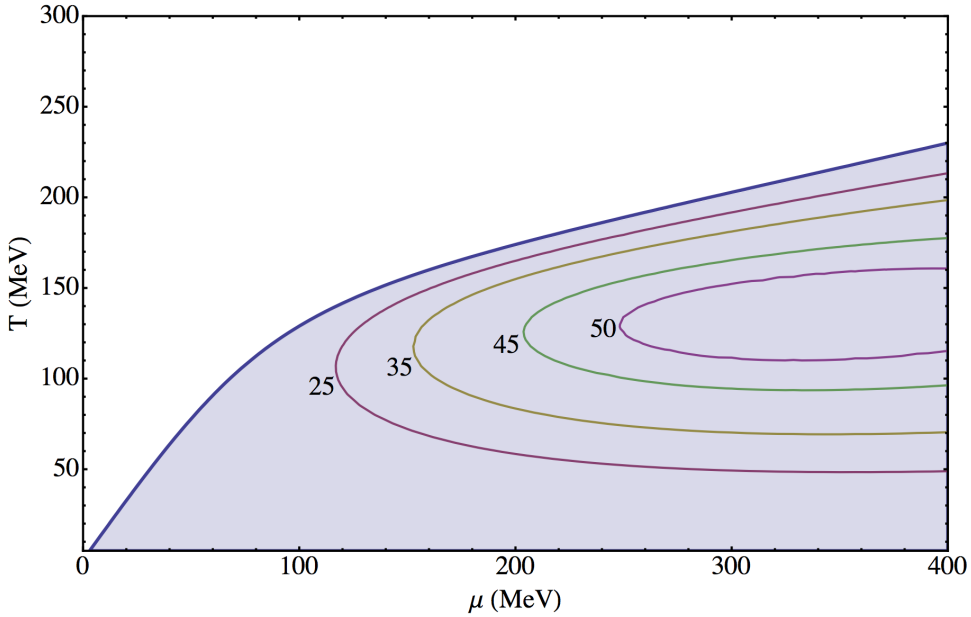

Figure 3.11: Contour plot of κ_I in the $\mu - T$ plane for Model A with massless quarks. Contours are given in MeV, with α_s set to one. The region where $\kappa_I \neq 0$ is shaded.

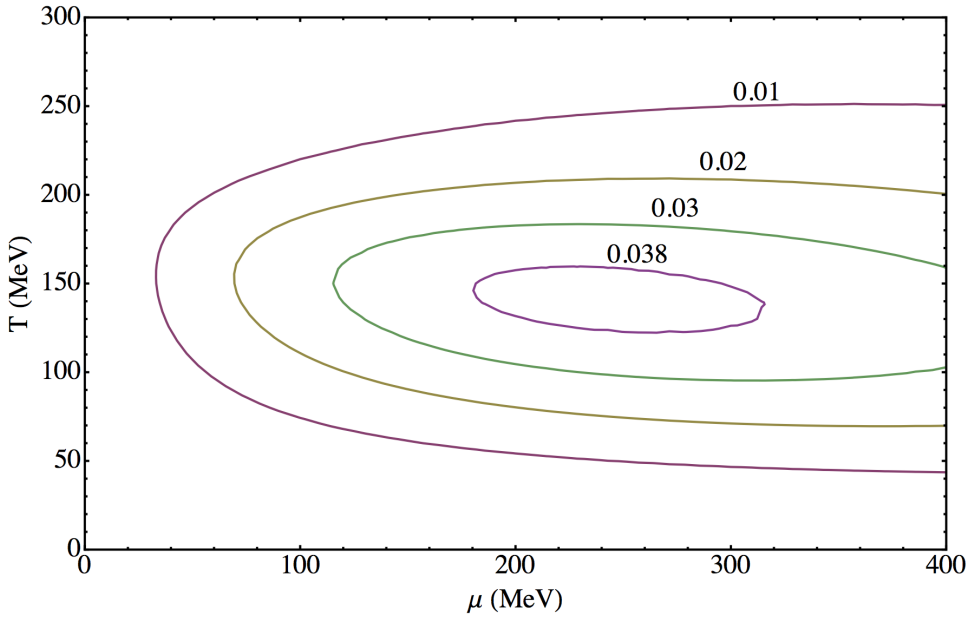

Figure 3.12: Contour plot of ψ in the $\mu - T$ plane for Model B with massless quarks, showing where $\mathrm{Tr}_F P$ is most different from $\mathrm{Tr}_F P^\dagger$.

known analytically [79]:

$$T = \frac{2\mu}{\sqrt{3}\pi}. \tag{3.43}$$

This behavior is generic to Model A when $T, \mu \gg m$, as we have seen for heavy quarks in the previous section.

The most interesting feature of Model B with massless quarks is that there is no region where κ_I is non-zero. Nevertheless, as shown in Fig. 3.12, ψ is non-zero, with a peak value near ($\mu = 250$ MeV, $T = 140$ MeV). This is the only case we have considered where there is no disorder line.

3.7 PNJL models

In this section we consider our most realistic models of QCD at finite temperature and density, PNJL models evaluated at complex saddle points. These models have a much richer structure because the effects of chiral symmetry breaking are included. Because the effective quark mass varies with T and μ, the behavior of the PNJL models in some sense lies between that of the heavy quarks and $m = 0$ quarks considered in the previous two sections, with a constituent quark mass that varies with T and μ. Figures 3.13 and 3.14 show the values of $\langle \mathrm{Tr}_F P \rangle$, $\left\langle \mathrm{Tr}_F P^\dagger \right\rangle$ and m for a PNJL model using V_d^A to implement confinement. In all figures of this type, the constituent quark mass m is normalized to its value at ($\mu = 0$, $T = 0$), while $\langle \mathrm{Tr}_F P \rangle$ and $\left\langle \mathrm{Tr}_F P^\dagger \right\rangle$ are normalized so that they go to one as T goes to infinity. As is typical of PNJL models with appropriately chosen parameters, only crossover behavior is seen at $\mu = 0$. There is a critical line starting at $\mu \approx 350$ MeV when $T = 0$ and ending at a critical point at approximately ($\mu \simeq 320$ MeV, $T \simeq 75$ MeV). This first-order line manifests itself in Fig. 3.13 in the discontinuous behavior of $\langle \mathrm{Tr}_F P \rangle$, $\left\langle \mathrm{Tr}_F P^\dagger \right\rangle$ and m at $T = 50$ MeV.

Figures 3.15 and 3.16 show the corrsponding behavior of $\langle \mathrm{Tr}_F P \rangle$, $\left\langle \mathrm{Tr}_F P^\dagger \right\rangle$ and m using V_d^B to implement confinement. In all figures of this type, m is normalized to its value at ($\mu = 0, T = 0$), while $\langle \mathrm{Tr}_F P \rangle$ and $\left\langle \mathrm{Tr}_F P^\dagger \right\rangle$ are normalized so that they go to one as T goes to infinity. As is Model A, only crossover behavior is seen at $\mu = 0$. The critical line starting at $\mu \approx 350$ MeV when $T = 0$ ends at a critical point at approximately ($\mu = 320\, MeV$, $T = 100\, MeV$). The first-order line again manifests itself in Fig. 3.15 in the discontinuous behavior of $\langle \mathrm{Tr}_F P \rangle$, $\left\langle \mathrm{Tr}_F P^\dagger \right\rangle$ and m at $T = 50$ MeV.

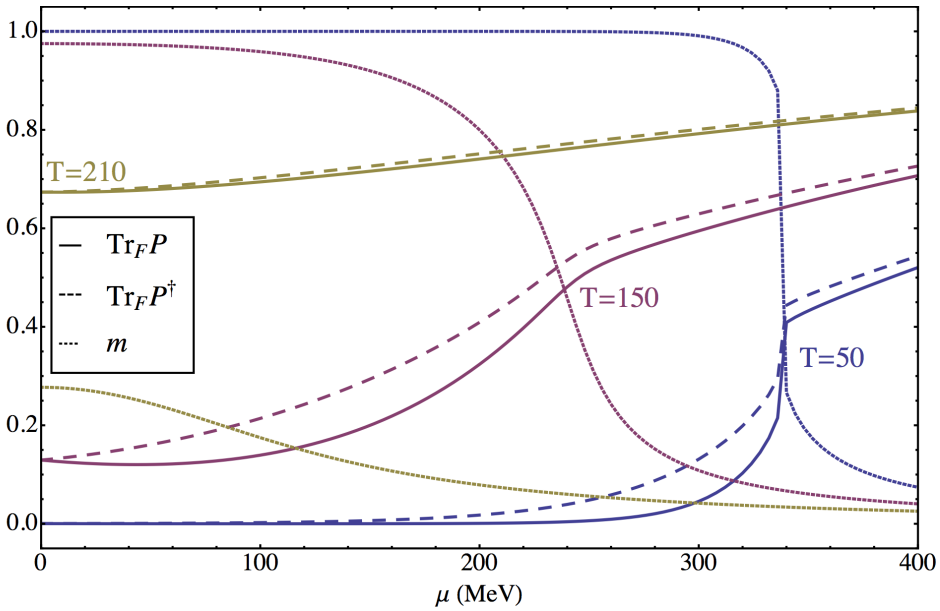

Figure 3.13: The constituent mass m, $\langle \mathrm{Tr}_F P \rangle$ and $\langle \mathrm{Tr}_F P^\dagger \rangle$ as a function of μ for $T =$ 50, 150, and 210 MeV for a PNJL model using Model A for confinement effects. The constituent mass m is normalized to one at $T = 0$, and the Polyakov loops are normalized to one as the temperature becomes large.

Figure 3.17 shows contour lines for ψ in the $\mu - T$ plane along with the region where $\kappa_I \neq 0$ as well as the critical line. The overall shape of the disorder line is similar to that found in the previous section for heavy quarks, but of course shifted to a much lower value μ. The critical line lies completely within the region $\kappa_I \neq 0$. Figure 3.18 shows a contour plot for κ_I. In both figures, a jump in ψ and κ_I is visible as the critical line is crossed.

As with Model A, the PNJL model using V_d^B shows many of the same features found for heavy quarks. Figure 3.19 contour lines for ψ in the $\mu - T$ plane along with the region where $\kappa_I \neq 0$ as well as the critical line, and Figure 3.20 shows a contour plot for κ_I. A striking difference between Model A and Model B is that the critical line now lies on the boundary of the region $\kappa_I \neq 0$, and the disorder line appears to be a smooth continuation of the critical

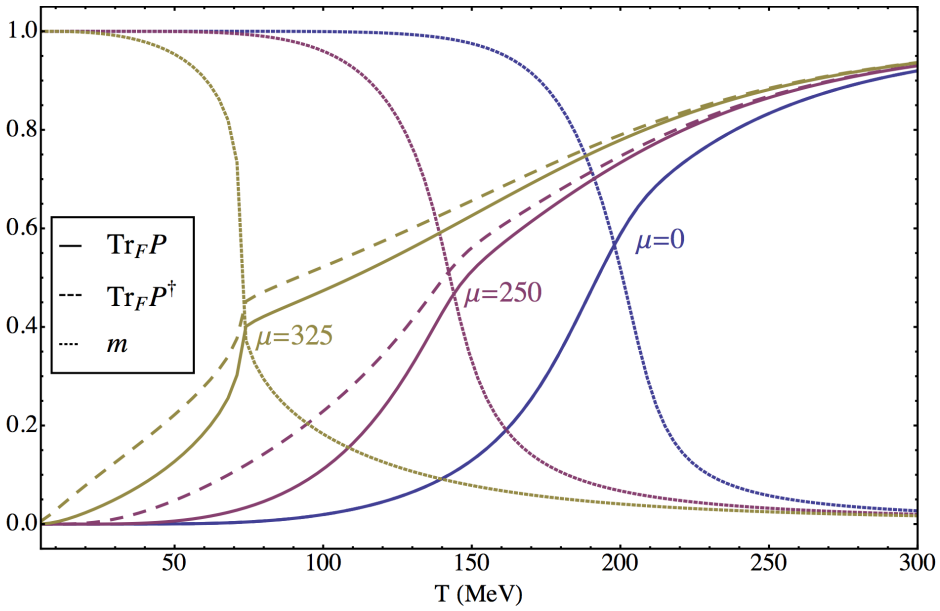

Figure 3.14: The constituent mass m, $\langle \mathrm{Tr}_F P \rangle$ and $\langle \mathrm{Tr}_F P^\dagger \rangle$ as a function of T for $\mu = 0$, 250 and 325 MeV for a PNJL model using Model A for confinement effects. The constituent mass m is normalized to one at $T = 0$, and the Polyakov loops are normalized to one as the temperature becomes large.

line out of the critical end-point.

3.8 Conclusions

As we have shown, the sign problem in QCD at finite density makes it very desirable to extend real fields into the complex plane. This extension is certainly necessary for steepest descents methods to yield correct results. Complex saddle points lead naturally to $\langle TrP \rangle \neq \langle TrP^\dagger \rangle$, a result that is much more difficult to obtain when fields are restricted to the real axis. The nature of these saddle points are restricted by $\mathcal{CK}$ symmetry. The case of a single dominant saddle point is particularly tractable in theoretical analysis. In the class of models we have examined, the saddle point is not far from the real axis, as indicated by the small values of ψ

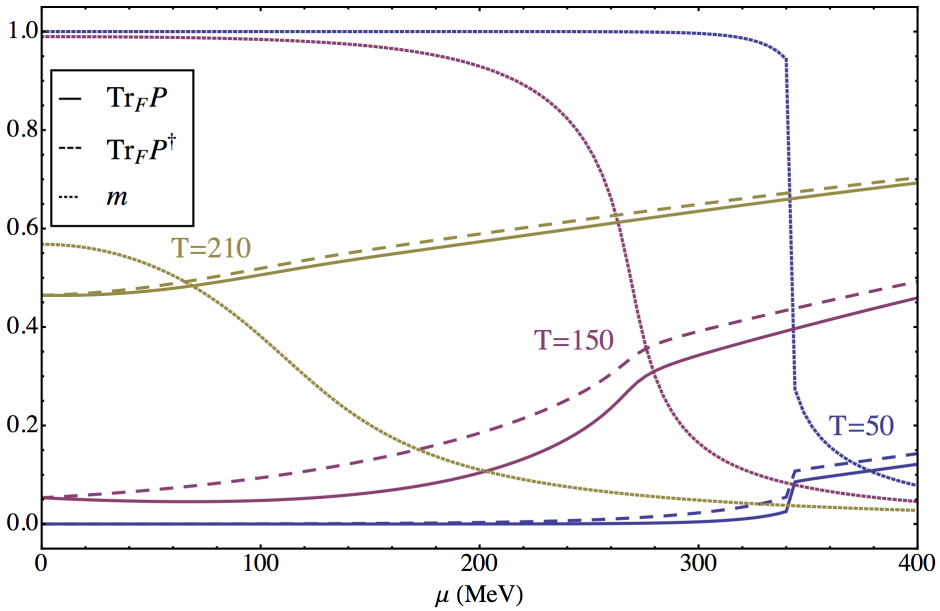

Figure 3.15: The constituent mass m, $\langle \mathrm{Tr}_F P \rangle$ and $\langle \mathrm{Tr}_F P^\dagger \rangle$ as a function of μ for $T =$ 50, 150, and 210 MeV for a PNJL model using Model B for confinement effects. The constituent mass m is normalized to one at $T = 0$, and the Polyakov loops are normalized to one in the limit as the temperature becomes large.

and corresponding small differences between $\langle TrP \rangle$ and $\langle TrP^\dagger \rangle$. This is good news for lattice simulation efforts, as it suggests only a modest excursion into the complex plane is needed. The small value of ψ also indicates a small difference for thermodynamic quantities such as pressure and internal energy between our work and previous work on phenomenological models where only real fields were used. For all six cases studied here, the maximum value of ψ occurs in the region where quark degrees of freedom are "turning on," as indicated by crossover or critical behavior. In our previous work on Model A for massless quarks [79], we were able to show analytically how $\psi \neq 0$ can arise from the interplay of confinement and deconfinement when $\mu \neq 0$, and our results here are consistent. For the two PNJL models, it is striking that the largest values of ψ occur near the critical end point. These predictions

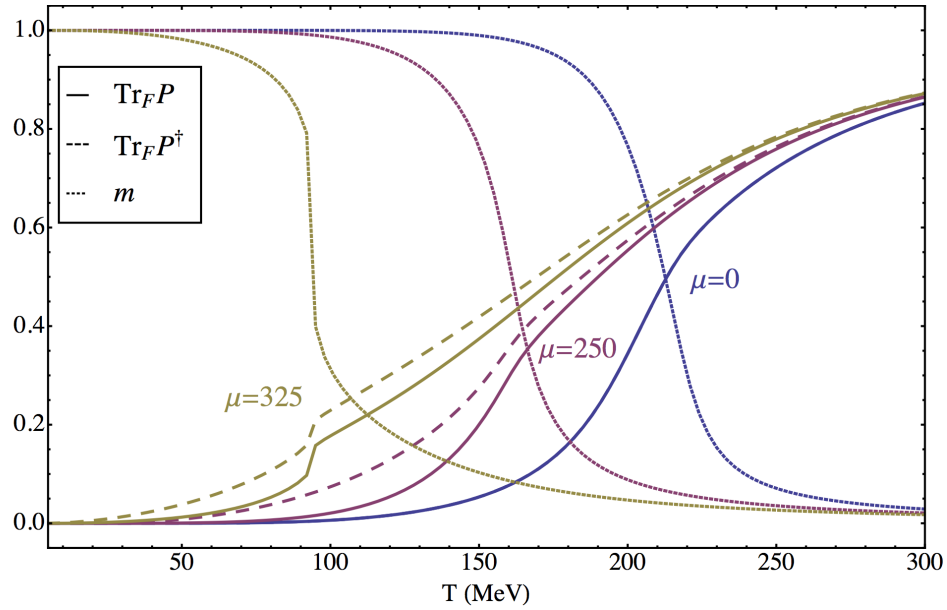

Figure 3.16: The constituent mass m, $\langle \mathrm{Tr}_F P \rangle$ and $\langle \mathrm{Tr}_F P^\dagger \rangle$ as a function of T for $\mu = 0$, 250 and 325 MeV for a PNJL model using Model B for confinement effects. The constituent mass m is normalized to one at $T = 0$, and the Polyakov loops are normalized to one in the limit as the temperature becomes large.

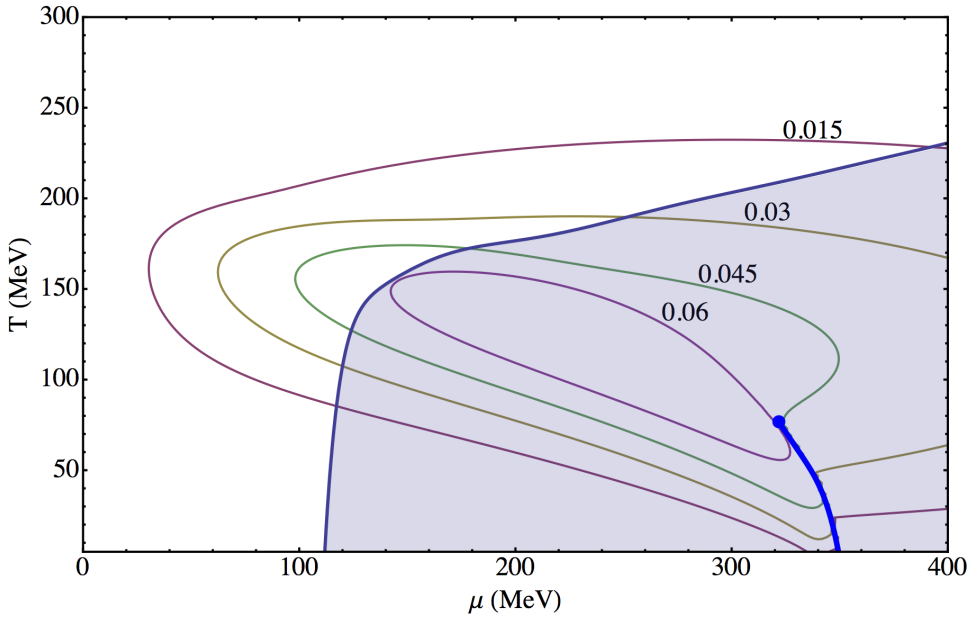

Figure 3.17: Contour plot of ψ in the $\mu - T$ plane for a PNJL modle using Model A for confinement effects. The region where $\kappa_I \neq 0$ is shaded. The critical line and its endpoint are also shown.

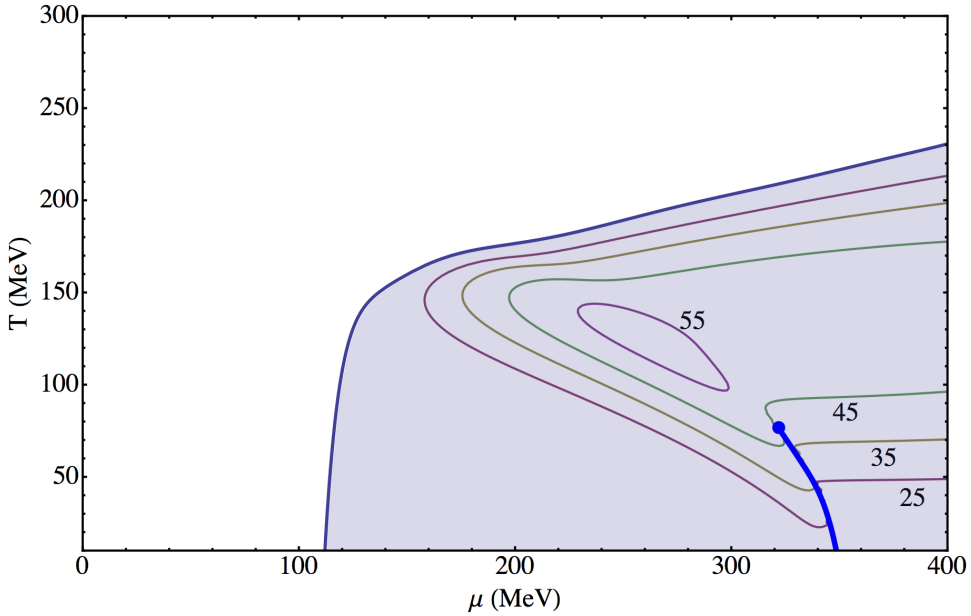

Figure 3.18: Contour plot of κ_I in the $\mu - T$ plane for a PNJL modle using Model A for confinement effects. Contours are given in MeV, with α_s set to one. The region where $\kappa_I \neq 0$ is shaded. The critical line and its endpoint are also shown.

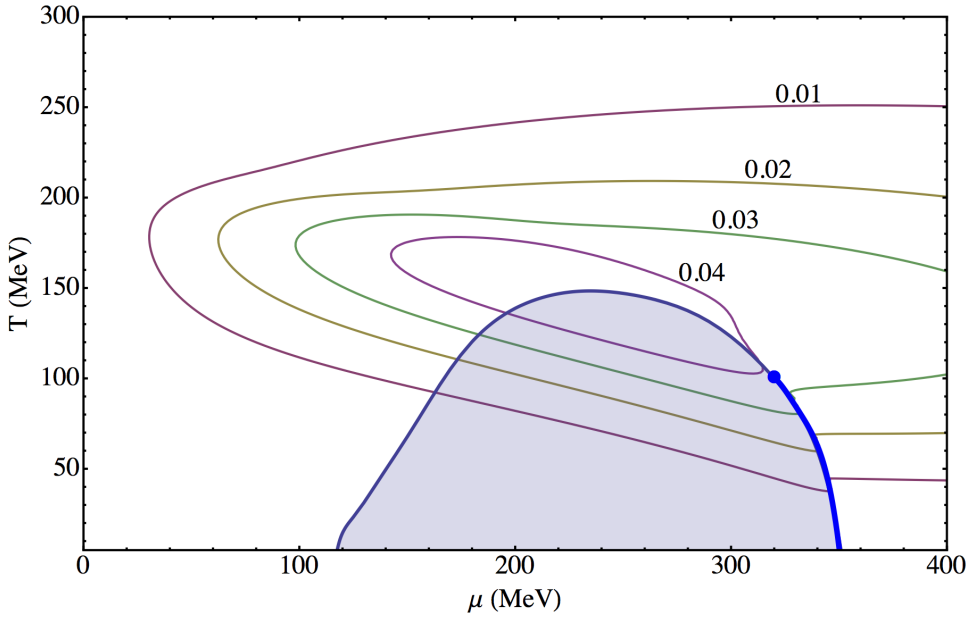

Figure 3.19: Contour plot of ψ in the $\mu - T$ plane for a PNJL modle using Model B for confinement effects. The region where $\kappa_I \neq 0$ is shaded. The critical line and its endpoint are also shown.

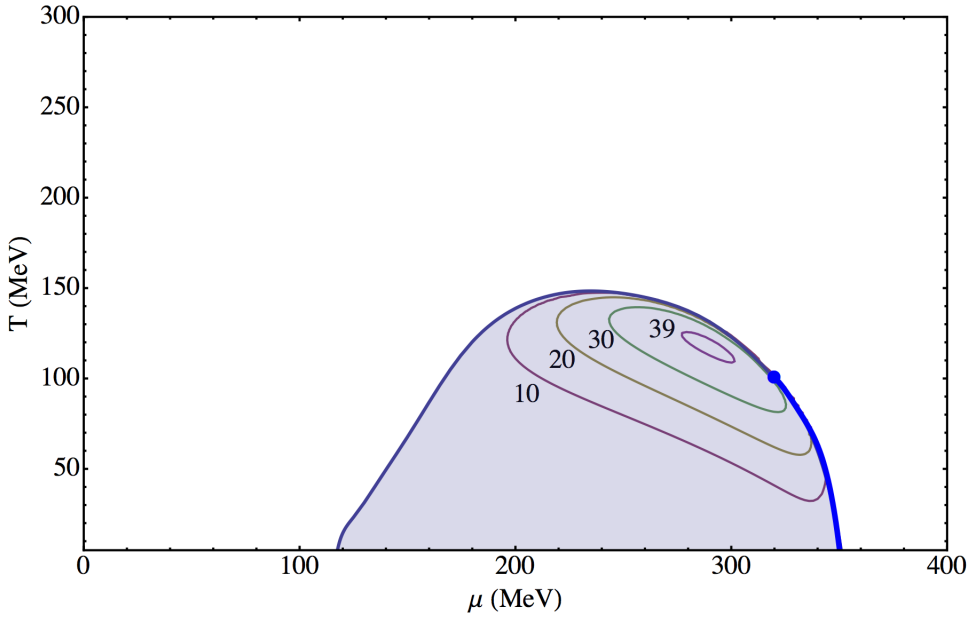

Figure 3.20: Contour plot of κ_I in the $\mu - T$ plane for a PNJL modle using Model B for confinement effects. Contours are given in MeV, with α_s set to one. The region where $\kappa_I \neq 0$ is shaded. The critical line and its endpoint are also shown.

can be checked in lattice simulations by the direct measurement of $\langle TrP \rangle$ and $\langle TrP^\dagger \rangle$ once sufficiently effective simulation algorithms are developed.

In all six cases studied, $\psi \neq 0$ leads to two different eigenvalues for the A_4 mass matrix. In five of the six cases studied, a disorder line is found. This disorder line marks the boundary of the region where the real parts of the mass matrix eigenvalues become degenerate as the eigenvalues form a complex conjugate pair. In the PNJL models, the disorder line is closely associated with the critical line. Inside the region bounded by the disorder line, the complex conjugate pairs gives rise to color charge density oscillations. Patel has developed a scenario in which such oscillations might be observed experimentally [76, 77]. Our results indicate that the oscillations may have too large a wavelength to be directly observable

in experiment, although estimates based on phenomenological models should be applied cautiously. The mass matrix eigenvalues are in principle accessible in lattice simulations via the measurement of Polyakov loop correlation functions. A direct determination of κ_I may be difficult, but the disorder line itself could be determined from the merging of the values of $Re\,(\kappa_1)$ with $Re\,(\kappa_2)$.

While the behavior of $\langle TrP \rangle$, $\left\langle TrP^\dagger \right\rangle$ and $\left\langle \bar{\psi}\psi \right\rangle$, as determined by lattice simulations, do not strongly differentiate between the two confining potential terms, Model A and Model B, the corresponding two-point correlation functions do. The most physically relevant case of PNJL models show both common features as well as clear differences in the behavior of the disorder line between Model A and Model B. In both cases, the maximum value of κ_I occurs slightly above and to the left of the critical end point in the $\mu - T$ plane, in the vicinity of the region where the ratio $Tr_F P^\dagger / Tr_F P$ is largest. In Model A, the critical line is contained within the boundary of the disorder line, but in Model B the disorder line appears to come out of the critical end point as a continuation of the critical line, a common behavior for disorder lines. Furthermore, in Model A the disorder line continues diagonally in the $\mu - T$ plane for large μ and T, but for Model B, the line bends over into the critical line. With Model A there is thus a possibility that the effects of the disorder line might be visible in the results of the Compressed Baryonic Matter (CBM) experiment at FAIR. The disorder line also strongly differentiates between Model A and Model B in the case of heavy quarks, so lattice simulations of either light or heavy quarks that can locate the disorder line have the potential to discriminate between the two models.

Chapter 4

COMPLEX SPECTRUM OF FINITE-DENSITY LATTICE QCD WITH STATIC QUARKS AT STRONG COUPLING

This chapter contains the materials published under the same title [1]*. This work was done in collaboration with Dr. Hiromichi Nishimura under the supervision of my advisor, Prof. Michael Ogilvie*

4.1 Introduction

Although lattice simulations have given excellent first-principles results for many observables of finite-temperature QCD, there has been less clear success when the chemical potential μ is nonzero. Finite-density QCD is one of the class of theoretical models that has a sign problem: the partition function is a sum over complex weights which cannot be interpreted as relative probabilities [41–43]. Many methods have been used in attempts to overcome the sign problem in finite-density QCD. Two methods that have received significant attention recently are the complex Langevin technique [91–96] and the Lefschetz thimble approach [56–59, 97–101]. We have recently explored the implications of complex saddle points in phenomenological models of QCD at finite temperature and density [79, 102]. These models postulate effective potentials for the Polyakov loop $Tr_F P_x$ and other order parameters in such a way that the confinement-deconfinement transition of quenched QCD is incorporated. The most realistic of these models are Polyakov-Nambu-Jona Lasinio (PNJL) models, and include

[1] Nishimura, H., Ogilvie, M.C. and Pangeni, K., 2016. Complex spectrum of finite-density lattice QCD with static quarks at strong coupling. Physical Review D, 93(9), p.094501.

the effects of chiral symmetry restoration [65]. In all the cases studied in [79, 102], a nonzero μ resulted in a complex saddle point for the eigenvalues of the Polyakov loop. A number of desirable results emerge from this. For example, the free energy is real at the complex saddle point and $\langle Tr_F P \rangle \neq \langle Tr_F P^\dagger \rangle$. The mass matrix for Polyakov loops exhibits a new feature: the mass eigenvalues may form a complex conjugate pair, indicating the occurrence of spatially-modulated sinusoidal decay. Such behavior is forbidden by spectral positivity for $\mu = 0$, but is possible when $\mu \neq 0$. In the case of PNJL models, complex conjugate pairs occur in regions around the first-order line that emerges from $T = 0$, terminating at a critical end-point.

Here we address the generality of this phenomenon by showing similar behavior in lattice QCD with static quarks in the strong-coupling limit. We will use a transfer matrix formalism to determine the behavior of Polyakov loop correlation functions as a function of spatial separation. These results are exact for any gauge coupling in $1 + 1$ dimensions, but also represent the leading-order result in the character expansion in higher dimensions. As the chemical potential of the static quarks is varied, we will show that there are large regions of parameter space where the eigenvalues of the transfer matrix form complex conjugate pairs, leading to damped oscillatory behavior of Polyakov loop correlation functions. The boundary of such a region in parameter space is referred to as a disorder line in condensed matter physics. The method used is completely different from the saddle point technique employed in [79, 102], applied to a very different model, illustrating the generality of the behavior. Any reliable simulation method for finite-density lattice QCD should be able to

reproduce our results, which thus can serve as a benchmark for the validation of algorithms.

Section II describes the strong-coupling formalism underlying our calculation. We give a graphical demonstration of the non-hermiticity of the correlation function matrix in character space when the chemical potential is nonzero. We also discuss the symmetries of the model, paying particular attention to particle-hole symmetry. Section III explains how the transfer matrix for Polyakov loops can be realized in the character basis in a form suitable for numerical diagonalization. In section IV, we present our results for the Polyakov loop spectrum. A final section gives our conclusions.

4.2 Strong-coupling formalism

4.2.1 Setup

Strong-coupling expansions and character expansions are well-developed methods for exploring the properties of lattice gauge theories [103]. Strong-coupling expansions are typically expansions in inverse powers of some coupling g^2 around $1/g^2 = 0$. Generally such expansions have a finite radius of convergence in an $1/g^2$, and thus are not directly relevant for the continuum limit of non-Abelian gauge theories at $g^2 = 0$. Nevertheless, they have often given important insight into mechanisms and critical behavior. Character expansions are closely related to strong-coupling expansions, but have many advantages. Consider the case of $SU(3)$ lattice gauge fields in $1 + 1$ dimensions at some finite temperature. In the absence of non-gauge fields, *i.e.*, the quenched approximation, this model is exactly solvable. The

action S_p of a single plaquette U_p can be expanded in character expansion

$$e^{S_p[U_p]} = \sum_R d_R c_R \chi_R (U_p) \tag{4.1}$$

where χ_R is the character of an irreducible representation R of the gauge group G, d_R is the dimensionality of R, and c_R is a coefficient that depends on the parameters of the gauge action S_p. The character expansion is an expansion in the ratios c_R/c_0, where c_0 is the coefficient of the trivial (identity) representation. A strong-coupling expansion in $1/g^2$ may be obtained by expanding these ratios. We will be using the character expansion in what follows.

Our principle observable is the trace of the Polyakov loop operator P_x in irreducible representations of $SU(3)$. The Polyakov loop operator P_x is the time-ordered product of the time-like links starting at a given point x and returning to that point due to the periodic boundary conditions of finite-temperature lattice gauge theories. The trace of P_x in an irreducible representation R measures confinement for that representation: $\langle Tr_R P \rangle = \exp(-\beta F_R)$, where F_R is the free energy required to insert a static particle in a representation R into the system and β is the inverse of the temperature T. In a pure gauge theory, the trace in the fundamental representation, $Tr_F P$, is an order parameter for confinement.

We will begin by giving simple arguments that show that the Polyakov loop propagator matrix is not Hermitian at finite density, indicating the possibility of complex eigenvalues. The correlation function of Polyakov loops in a representation R, $\left\langle Tr_R P_x Tr_R P_y^\dagger \right\rangle$ is given to lowest order in the character expansion by tiling space with plaquettes in the representation

R between x and y. We now introduce static quarks into this system. Each quark carries with it a factor of $Tr_F P$ with an additional factor of $\exp(\beta\mu)$ when the chemical potential $\mu \neq 0$. As shown in Fig. 4.1, this generates a new interaction not present in the quenched case that couples $Tr_F P$ to itself. Correlation functions of the form $\langle Tr_R P_x Tr_R P_y \rangle$ have been measured in lattice simulation of full QCD at $\mu = 0$ [104]. When $\mu \neq 0$, the lowest-order contribution to $\langle Tr_R P_x Tr_R P_y \rangle$ is enhanced by a weight factor $\exp(\beta\mu)$. On the other hand, the coupling of $Tr_F P^\dagger$ to itself, as represented in Fig. 4.2, is suppressed by a corresponding factor of $\exp -\beta\mu$. The only difference between the two graphs is the factor of $\exp(\beta\mu)$ versus $\exp(-\beta\mu)$ so $\langle Tr_R P_x Tr_R P_y \rangle \neq \left\langle Tr_R P_x^\dagger Tr_R P_y^\dagger \right\rangle$. Thus when $\mu \neq 0$ the matrix of two-point correlation functions is no longer Hermitian. In order to find masses, that matrix of correlation functions must be diagonalized. However, if the correlation matrix is not Hermitian, the masses need not be real. The asymmetry between $Tr_F P$ and $Tr_F P^\dagger$ is a consequence of the explicit breaking of charge conjugation $\mathcal{C}$ by the chemical potential. However, the symmetry of finite-density QCD under the combined action of $\mathcal{C}$ and complex conjugation $\mathcal{K}$ remains intact [79, 102, 105, 106]. Thus the combined action of $\mathcal{CK}$ leaves $Tr_F P$ and $Tr_F P^\dagger$ invariant. For our purposes, the most important consequence of the $\mathcal{CK}$ symmetry is that the masses are either real or are part of a complex conjugate pair, as we discuss below.

A comprehensive treatment of Polyakov loop correlation functions at strong coupling is most conveniently carried out using a version of Svetitsky-Yaffe universality [107, 108]. This fundamental result for gauge theories at finite temperature links the critical behavior

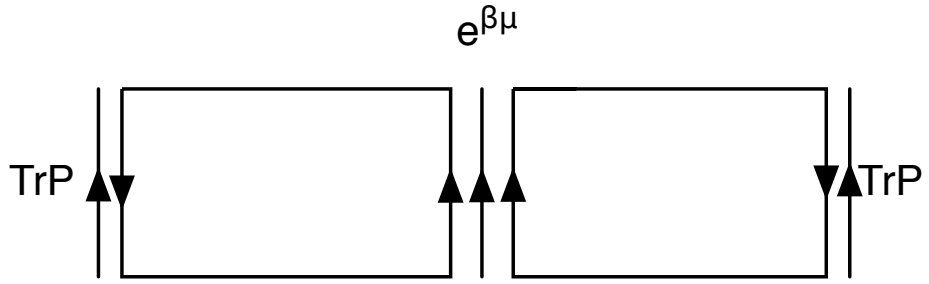

Figure 4.1: Graphical representation of a contribution of fermions to $\langle Tr_F P\, Tr_F P\rangle$

.

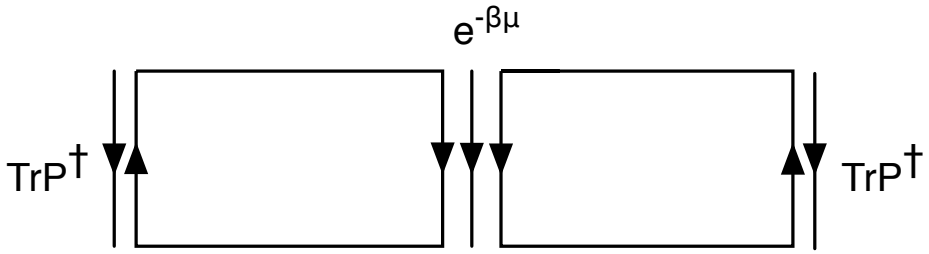

Figure 4.2: Graphical representation of a contribution of fermions to $\left\langle Tr_F P^\dagger\, Tr_F P^\dagger\right\rangle$.

of Polyakov loops in pure gauge theories in d dimensions with the behavior of spin systems in $d-1$ dimensions. Furthermore, the effect of introducing quarks into the gauge theory is similar to the effect of an external magnetic field on a spin system. It is easy in strong coupling to show that the effective action for the interaction of Polyakov loops is similar to that found in a spin system. If we consider two adjacent Polyakov loops on a lattice, they share a "belt" of plaquettes running up the time axis. Integrating over the spatial links of this belt leads to an effective interaction between the Polyakov loops of the form

$$\sum_R c_R^{N_t} \chi_R\left(P_x\right) \chi_R\left(P_y^\dagger\right) \tag{4.2}$$

where P_x and P_y are Polyakov loops on adjacent spatial lattice sites x and y. The parameter N_t is the temporal size of the lattice, so $\beta = N_t a$, where a is the lattice spacing. To leading order in a strong-coupling expansion, the exponential of the effective action is

$$e^{S_{eff}} = \prod_{\langle xy \rangle} \left[\sum_R c_R^{N_t} \chi_R \left(P_x \right) \chi_R \left(P_y^\dagger \right) \right] \tag{4.3}$$

where the product is taken over all nearest-neighbor spatial lattice sites. For very strong coupling, the contribution of the fundamental representation usually dominates, and the effective action may be written approximately as

$$e^{S_{eff}} \simeq \exp \left\{ \sum_{\langle xy \rangle} J \left[\chi_F \left(P_x \right) \chi_F \left(P_y^\dagger \right) + \chi_F \left(P_x^\dagger \right) \chi_F \left(P_y \right) \right] \right\} \tag{4.4}$$

where the sum over $\langle xy \rangle$ is a sum over nearest-neighbor pairs of spatial points and

$$J = \left(\frac{c_F}{c_0} \right)^{N_t}. \tag{4.5}$$

This is clearly of the form of a spin system, with spins taking on values in G and the interaction respecting global center symmetry.

In order to arrive at a simple model, we consider only the case where quarks are so heavy that move only in time and are static in space. In this case, the effects of quarks at x can

be represented in the partition function by a weight [89]

$$D_x = \det\left[1 + e^{\beta\mu - \beta M} P_x\right] \tag{4.6}$$

while antiquarks give a weight factor

$$\bar{D}_x = \det\left[1 + e^{-\beta\mu - \beta M} P_x^\dagger\right] \tag{4.7}$$

where μ is the chemical potential and M is the heavy quark mass. It will be convenient to associate two different "activities" for quarks and antiquarks:

$$z_1 = e^{\beta\mu - \beta M} \tag{4.8}$$

$$z_2 = e^{-\beta\mu - \beta M}. \tag{4.9}$$

Although z_1 and z_2 may take on any non-negative values, their association with μ and M does impose restrictions: Depending on the sign of μ, either z_1 or z_2 is always less than one. However, it is sometimes convenient to ignore this restriction to display the symmetries of the model. The complete partition function is given by

$$Z = \int [dP] \prod_x \left[D_x \bar{D}_x\right] \prod_{\langle xy \rangle} \left[\sum_R c_R^{N_t} \chi_R\left(P_x\right) \chi_R\left(P_y^\dagger\right)\right] \tag{4.10}$$

where the integral $[dP]$ is over Haar measure for the Polyakov loop P_x on each spatial lattice site x and the sum over $\langle xy \rangle$ is a sum over nearest-neighbor pairs.

4.2.2 Symmetries

The physics of $SU(N)$ static quarks at finite density is invariant under $(z_1, z_2) \to (z_2, z_1)$ provided we also switch our definition of particle and antiparticle operators. However, we need not switch operators at the special points where $z_1 = z_2$. These are the points where $\mu = 0$ and we have particle-antiparticle symmetry. Notice however that the identity

$$\det\left[1 + z_1 P_x\right] = z_1^N \det\left[1 + z_1^{-1} P_x^\dagger\right] \tag{4.11}$$

also leads to an invariance and a symmetry. The factor of z_1^N represents the Boltzmann factor for a completely filled state at a site. Although this factor of z_1^N does contribute to the free energy, it does not affect expectation values. This operation reflects the equivalence between particles and holes: a particle (relative to the vacuum) is equivalent to $N-1$ holes (relative to the completely filled state) at the same site. In the special case where $z_2 = 0$, there is an exact particle-hole symmetry under $z_1 \to 1/z_1$. This extends to an approximate particle-hole symmetry when antiparticle effects are small. If we apply the above identity to antiparticles as well as particles, we obtain an exact symmetry of the complete theory: The model is invariant under the transformation $(z_1, z_2) \to (1/z_2, 1/z_1)$. Note however that this transformation takes the physical region $z_1, z_2 < 1$ into the unphysical region $z_1, z_2 > 1$.

Let us suppose we are in a low-temperature, large μ region where $z_2 \ll 1$ and antiparticle effects can be neglected. Then the fermion determinant D is real and there is no sign problem when $z_1 = 1$; this is precisely the absence of a sign problem at "half-filling" for static quarks.

See [109] for an extensive treatment of this property. These symmetries are easily extended to any representation of the gauge group. Note that an alternative approach to including static quarks at finite density is to add a term

$$\sum_x \left[z_1 \mathrm{Tr}_F P_x + z_2 \mathrm{Tr}_F P_x^\dagger \right] \tag{4.12}$$

directly to the action. However, this is an approximation to lowest order in z_1 and z_2 of the effects of static fermions or bosons. It therefore misses the effects of Pauli blocking as well as the symmetries of the fermion determinant just discussed.

In addition to the invariances associated with z_1 and z_2, this model inherits from finite-density QCD invariance under the combined action of charge conjugation $\mathcal{C}$ and complex conjugation $\mathcal{K}$ [79, 102]. Charge conjugation takes $Tr_F P_x \to Tr_F P_x^\dagger$. It is a symmetry when $\mu = 0$, but not when $\mu \neq 0$. Complex conjugation is an antilinear symmetry, changing not only fields but also complex-conjugating ordinary numbers. Like $\mathcal{C}$, $\mathcal{K}$ is a symmetry of the model only when $\mu = 0$. $\mathcal{K}$ acts on $Tr_F P$ to give $Tr_F P^* = Tr_F P^\dagger$. It is easy to see that the combined effect of $\mathcal{CK}$ is to leave the action invariant. From this, it can be shown that all the eigenvalues of the transfer matrix are either real or are part of a complex conjugate pair. Due to the symmetry of the model, the transfer matrix T_s commutes with $\mathcal{CK}$. If $T_s |\lambda\rangle = \lambda |\lambda\rangle$ it follows that

$$T_s \mathcal{CK} |\lambda\rangle = \mathcal{CK} T_s |\lambda\rangle = \mathcal{CK}\lambda |\lambda\rangle = \lambda^* \mathcal{CK} |\lambda\rangle \tag{4.13}$$

so λ^* is an eigenvalue of T_s if λ is. Correlation functions of operators that couple to eigenstates of T_s with complex eigenvalues will generally exhibit some amount of sinusoidally-modulated exponential decay rather than the usual exponential decay found in models with Hermitian actions [79, 102, 105, 106]. We will show below that this sinusoidal modulation is present in strong-coupling QCD with a finite density of static quarks.

4.3 Strong-coupling calculation of the spectrum

In $1+1$ dimensions, the transfer matrix connecting one Polyakov loop P_x to its nearest neighbor P_y in a pure gauge theory can be written as

$$T_0 = \sum_R c_R^{N_t} \chi_R\left(P_x\right) \chi_R\left(P_y^\dagger\right) \tag{4.14}$$

in the gauge-invariant basis where states are class functions of P:

$$\Psi\left(P\right) = \sum_R b_R \chi_R(P). \tag{4.15}$$

We can regard T_0 as acting on wave functions $\Psi(P)$ or alternately on an infinite vector of coefficients b_R. We refer to the latter representation as the group character basis. We are free to choose the lattice action as reflected by the coefficients c_R, provided they have the correct behavior in the continuum limit. Although the Wilson action is the most common lattice action, there is an infinite class of lattice actions that lead to the same continuum limit. Because we are interested in tracking the behavior of Polyakov loop correlation functions in

many representations, we will need to keep the higher-order terms in the character expansion of the effective action. We will use the heat kernel action, for which the coefficients are

$$c_R = \exp\left(-g^2 C_R a^2/2\right) \tag{4.16}$$

where C_R is the quadratic Casimir invariant for R. This has important advantages for us over the standard Wilson action. The expression for c_R is simple and easy to calculate. In addition, it yields exactly the continuum results for string tensions for pure gauge theories in $1+1$ dimensions. See [108, 110, 111] for an explanation of other properties of the heat kernel action.

Using the identification $\beta = N_t a$, the transfer matrix T_0 has the form

$$T_0 = \sum_R \exp\left(-\beta g^2 a C_R/2\right) \chi_R\left(P_x\right) \chi_R\left(P_y^\dagger\right). \tag{4.17}$$

In the group character basis the Casimir operator is diagonal. For $SU(3)$, its eigenvalues are

$$C(p,q) = \frac{(p+1)^2 + (q+1)^2 + (p+1)(q+1)}{3} - 1 \tag{4.18}$$

where (p,q) specify the particular irreducible representation of R of the gauge group. Here p represents the number of columns of one box and q represents the number of columns of

two boxes in Young tableau. The transfer matrix in the group character basis is

$$T_0 = e^{-\frac{g^2\beta a}{2}C(p_1,q_1)}\delta_{p_1p_2}\delta_{q_1q_2}. \tag{4.19}$$

In the pure gauge theory, the eigenvalues of T_0 determine the exponential decay of correlation functions:

$$\left\langle \mathrm{Tr}_R P_x \mathrm{Tr}_R P_y^\dagger \right\rangle \sim \exp\left(-C(p_1,q_1)\frac{g^2\beta a}{2}\left|x-y\right|\right). \tag{4.20}$$

It is convenient to define the combination $g^2\beta/2$ to be m_0, so that each representation R is associated with a mass $m_{p,q} \equiv C\left(p,q\right)m_0$ in the pure gauge theory. The eigenvalues of the pure gauge theory transfer matrix T_0 are given by

$$\lambda_{p,q} = e^{-\frac{g^2\beta a}{2}C(p_1,q_1)} \tag{4.21}$$

so a mass $m_{p,q}$ can be extracted as

$$m_{p,q} = -\frac{1}{a}\log\left(\frac{\lambda_{p,q}}{\lambda_{0,0}}\right). \tag{4.22}$$

In the more general case where static quarks are present, the eigenvalues of the transfer matrix cannot be associated with a fixed group representation, and the corresponding eigenvectors in character space are linear combinations of group characters. In general, we simply

number the eigenvalues sequentially starting at zero, and define the mass by

$$m_j = -\frac{1}{a}\log\left(\left|\frac{\lambda_j}{\lambda_0}\right|\right) \tag{4.23}$$

taking into account that the eigenvalues may be complex. Note that m_0 is simply a convenient mass scale, and not the mass of the ground state. If we consider m_j/m_0 in the limit where quark effects vanish, we obtain the Casimir operator $C(p,q)$. It is only in this sense that a given mass can be associated with a representation in the general case. In the case where λ_j is complex, $\mathrm{Arg}\,(\lambda_j)$ determines the wavenumber for the oscillations. In general, we define

$$\exp\left(-m_j a + i k_j a\right) = \frac{\lambda_j}{\lambda_0} \tag{4.24}$$

so that $k_j a = Arg\,(\lambda_j/\lambda_0)$ determines the period of oscillation for a given eigenvalue j. In all the cases considered here, the ground state is unique and λ_0 is real and positive, so $k_j a = Arg\,(\lambda_j)$. We will take the lattice spacing a to be 1, and treat m_0 as the fundamental parameter of the pure gauge theory.

In the group character basis, $\mathrm{Tr}_F P$ and $\mathrm{Tr}_F P^\dagger$act as raising and lowering operators and can be expressed in terms of Kronecker deltas

$$\mathrm{Tr}_F P = \delta_{p_1,p_2}\delta_{q_1,q_2-1} + \delta_{p_1,p_2-1}\delta_{q_1,q_2+1} + \delta_{p_1,p_2+1}\delta_{q_1,q_2} \tag{4.25}$$

$$\mathrm{Tr}_F P^\dagger = \delta_{p_1,p_2-1}\delta_{q_1,q_2} + \delta_{p_1,p_2+1}\delta_{q_1,q_2-1} + \delta_{p_1,p_2}\delta_{q_1,q_2+1}. \tag{4.26}$$

The effect of heavy static quarks can in turn be represented in the partition function by the fermion determinant

$$D\left(z_1\right) = 1 + z_1 \mathrm{Tr}_F P + z_1^2 \mathrm{Tr}_F P^\dagger + z_1^3 \tag{4.27}$$

while the effect of antiquarks is represented by

$$\bar{D}\left(z_2\right) = 1 + z_2 \mathrm{Tr}_F P^\dagger + z_2^2 \mathrm{Tr}_F P + z_2^3 \tag{4.28}$$

where z_1 and z_2 are the "activities" for quark and antiquark defined above. The overall transfer matrix including the effect of quarks and antiquarks can be written as

$$T_s = T_0^{1/2} D\left(z_1\right) \bar{D}\left(z_2\right) T_0^{1/2}. \tag{4.29}$$

This particular form is chosen so that T_s is Hermitian when $z_1 = z_2$. While the transfer matrix corresponding to pure gauge fields, T_0, is Hermitian, the final transfer matrix, T_s, that includes the effect of heavy quarks and antiquarks is no longer Hermitian. $\mathrm{Tr}_F P$ and $\mathrm{Tr}_F P^\dagger$ connects between different representations so they introduce off diagonal elements in the transfer matrix. Since $\mathrm{Tr}_F P$ and $\mathrm{Tr}_F P^\dagger$are different for $\mu \neq 0$, the off-diagonal elements are no longer symmetric and the transfer matrix is non-Hermitian.

In $1+1$ dimensions, the results obtained from the transfer matrix are exact at any value of the coupling. In the strong coupling region, the results from $1+1$ dimensions are also valid in higher dimensions to leading order in the character expansion. This result was noted long ago by [112]. Consider the strong-coupling expansion for a free scalar field, as shown

in Fig. 4.3. For on-axis correlation functions, say $\langle \phi(0)\, \phi(r\hat{x}) \rangle$, the leading diagram is a line between the two points, the single path of minimal length. For off-axis correlation functions, there are multiple minimal-length paths in the taxicab metric, e.g. $|x| + |y| + |z|$ in $3+1$ dimensions, but this gives rise to a prefactor that does not change the exponential decay of the correlation function. When looked upon as a spin system, the diagrammatic expansion here behaves similarly, so the leading-order strong-coupling result in $1+1$ dimensions is also the result in $d+1$ dimensions. Higher-order corrections to masses do explicitly depend on d. In any dimension, the strong-coupling expansion is a convergent expansion with a finite radius of convergence, so there will be some region around $g^{-2} = 0$ where the lowest order result is a good approximation.

The analogous behavior for a gauge theory at finite temperature is shown in Fig. 4.4 below. For on-axis correlation functions of widely-separated Polyakov loops, the dominant contribution at strong coupling is a straight sheet, exactly as in $1+1$ dimensions. For the off-axis correlation function, there will be many minimal surfaces connecting the two Polyakov loops, but this will not change the rate of exponential fall-off at leading order in strong coupling. Thus we see that the strong-coupling results in $1+1$ dimensions are also valid in $d+1$ dimensions.

4.4 Results for the mass spectrum

We now discuss our results for the low-lying eigenvalues of T_s. We begin with the case where z_1 and z_2 are set to a common value z, which corresponds to setting μ to zero so that z can be identified with $\exp(-\beta M)$. In this case, the model is Hermitian so the eigenvalues

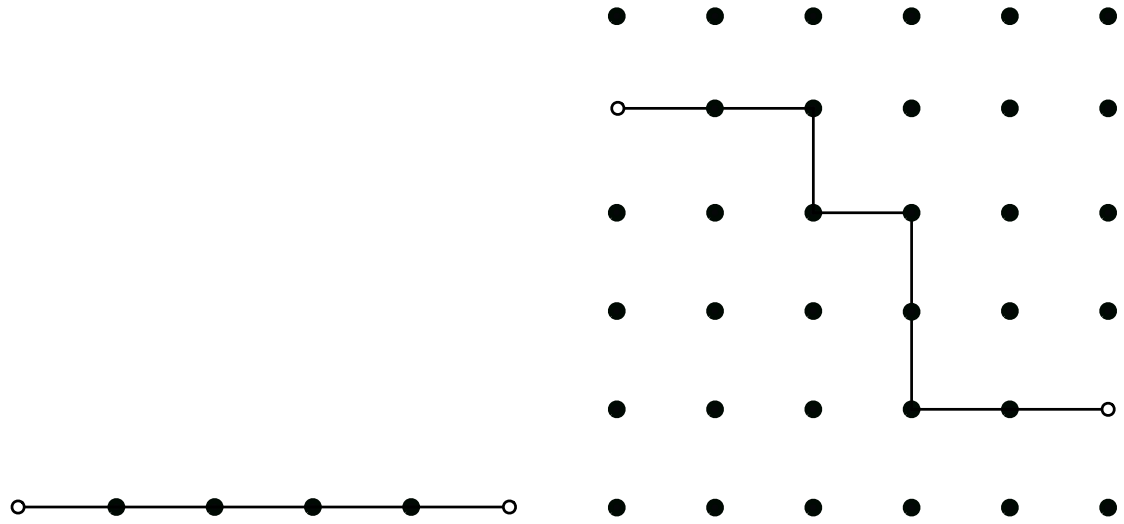

(a) In one dimension, the only graph is a straight line connecting the endpoints (open circles).

(b) In two or more dimensions, off-axis correlation functions typically have many paths of minimal length connecting the endpoints, but this degeneracy does not change the rate of exponential fall-off at leading order in strong coupling.

Figure 4.3: Strong-coupling diagrams for a free scalar theory.

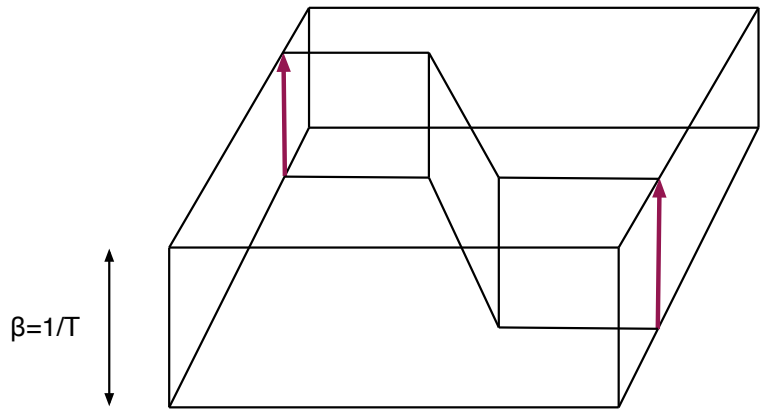

Figure 4.4: A contribution to the off-axis correlation function between two-widely separated Polyakov loops. For clarity, the intermediate staircase has been replaced by a diagonal sheet.

are real and $\langle Tr_F P \rangle = \langle Tr_F P^\dagger \rangle$. Figure 4.5 shows the mass spectrum of the low-lying eigenstates and Polyakov loop expectations values for $m_0 = 1$ and 2. The masses shown in the figures below are always divided by the mass scale m_0; the values of m_j/m_0 at $z = 0$, on the left-hand axis, are thus the values of the Casimir operator for low-lying representations of $SU(3)$. In particular, we can associate the masses shown in Fig. 4.5 with the 3, $\bar{3}$, 8, 6 and $\bar{6}$ representations of $SU(3)$ when $z = 0$. As can be seen in the figure, the values on the left-hand axis at $z = 0$ are precisely 4/3, 3 and 10/3. For $z > 0$, the corresponding eigenvectors contain a mixture of the identity representation, the above five representations and other higher-dimensional representations. Both the spectrum and Polyakov loop expectation values are invariant under $z \to 1/z$. This is reflected in the peaks achieved at $z = 1$ by both the masses and the Polyakov loop expectation values. Physically, quark effects behave as an external magnetic field, and this effect is strongest at $M = 0$, corresponding to $z = 1$. Increasing m_0 from 1 to 2 shortens the correlation length in lattice units, and decreases the effects of the fermions on the spectrum. The peak in the Polyakov loop at $z = 1$ is smaller at $m_0 = 2$ than at $m_0 = 1$ because the interaction between nearest-neighbor Polyakov loops is smaller. At $z = 0$, pairs of complex representations like the 3 and $\bar{3}$ have degenerate masses. Because the quark determinant breaks the $Z(3)$ symmetry of the pure gauge theory, the eigenstates for $z > 0$ do not show any degeneracy, but separate into clear, well-defined levels.

We next consider the case where the effects of antiquarks are neglected, which corresponds to setting $z_2 = 0$. Figure 4.6 shows the real and imaginary parts of the mass spectrum, m_j/m_0

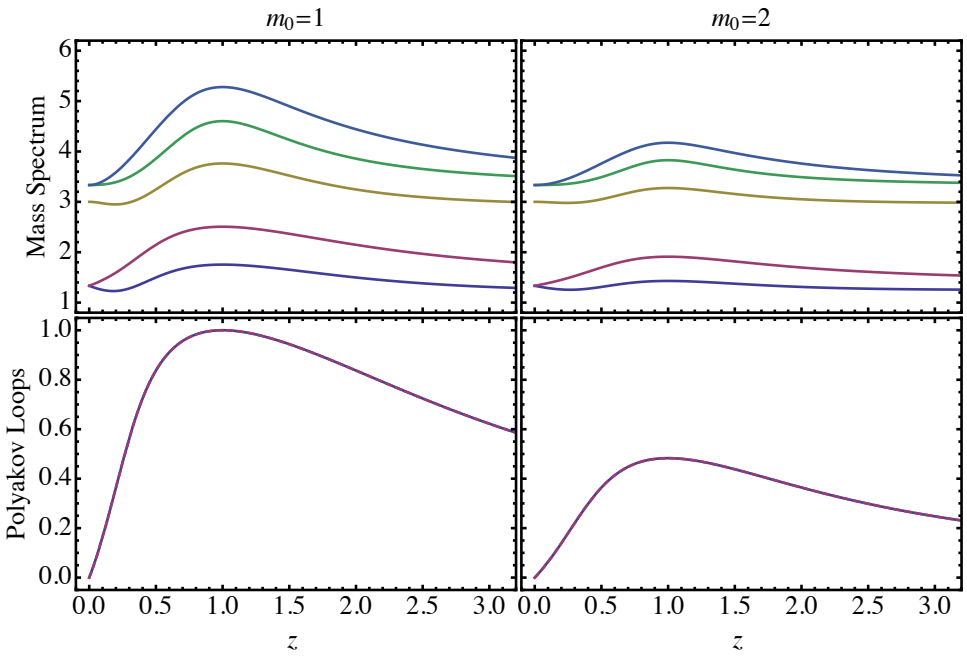

Figure 4.5: The mass spectrum and Polyakov loop expectation values for the $(1+1)$-dimensional $SU(3)$ model as a function of z with $m_0 = 1$ and $m_0 = 2$.

and $Arg\,[\lambda_j]$, for low-lying eigenstates when $m_0 = 1$ and 2. The figure also shows Polyakov loop expectation values. As seen in the plots, the masses start out real for $z_1 = 0$ but quickly take on complex values for non-zero z_1. As z_1 increases, the magnitude of complex part of the mass gradually increases before dropping back to zero. The plots clearly reflect the particle-hole symmetry under $z_1 \to 1/z_1$. The real part of mass spectrum is highest when $z_1 = 1$, which corresponds to $\mu = M$. The point $z_1 = 1$ is special because the theory is Hermitian at half-filling and the mass spectrum must be real. Furthermore, there appears to be a region around $z_1 = 1$ where the mass spectrum is real. The size of this region is largest for the 3 and $\bar{3}$ representations. The 8 representation does not develop an imaginary part. For $z_1 < 1$, $\langle Tr_F P \rangle$ is less than $\langle Tr_F P^\dagger \rangle$, implying that the free energy cost of inserting a fermion into

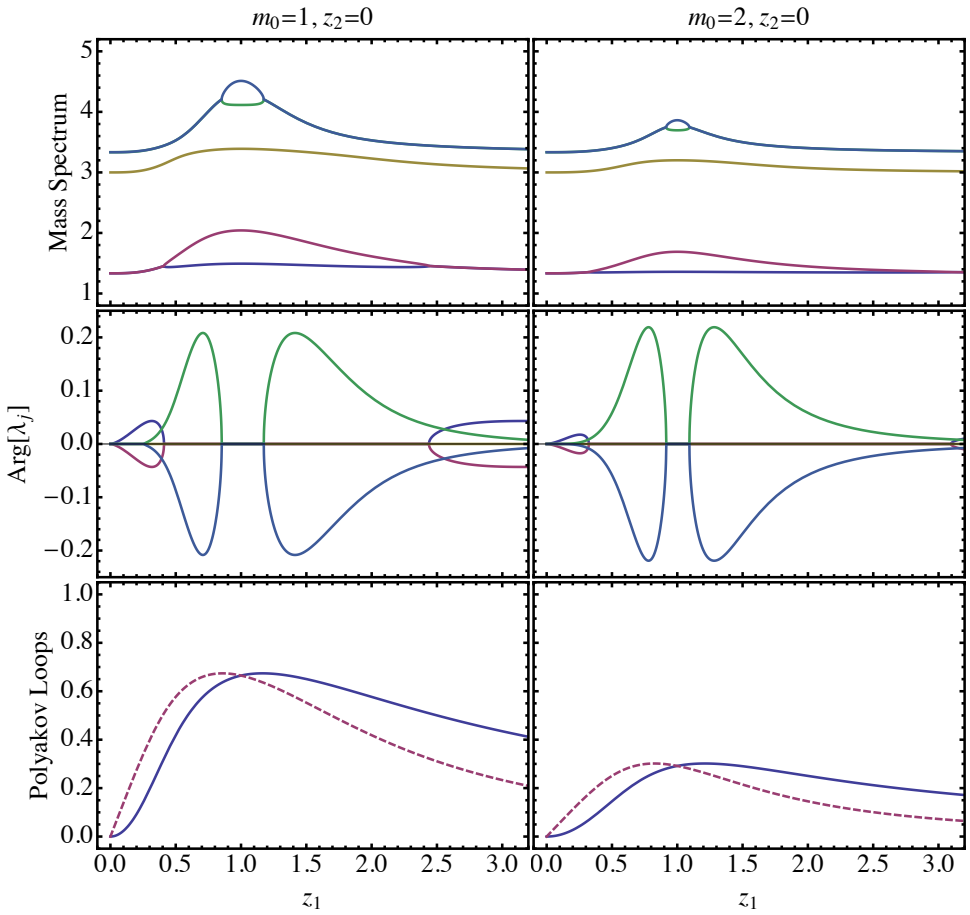

Figure 4.6: The real and imaginary parts of the mass spectrum and Polyakov loop expectation values for the $(1+1)$-dimensional $SU(3)$ model as a function of z_1 with $m_0 = 1$ and $m_0 = 2$ and $z_2 = 0$. The Polyakov loop $\langle Tr_F P \rangle$ is represented by a solid line, and $\langle Tr_F P^\dagger \rangle$ by a dashed line.

the system is greater than that of inserting an antifermion. For $z_1 > 1$, this behavior is reversed in accordance with the $z_1 \to 1/z_1$ symmetry. At $z_1 = 1$, the two expectation values are equal. As in the case $z_1 = z_2$, moving from $m_0 = 1$ to $m_0 = 2$ lessens the impact of fermions on the spectrum and on Polyakov loop expectation values. As mentioned earlier, this increase in scale of pure gauge theory lessens the effects of fermions as seen in the plots.

We next consider the effects of antiquarks as gradually "turned on" by making z_2 non-

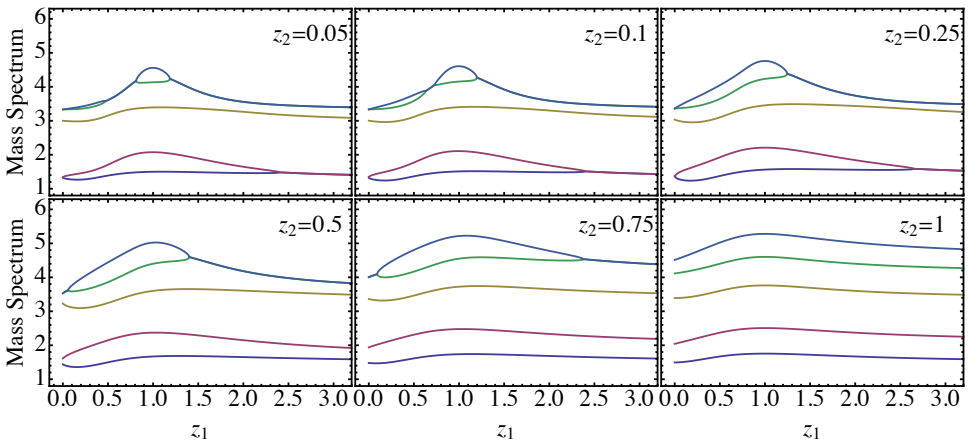

Figure 4.7: The real part of the mass spectrum of the $(1+1)$-dimensional $SU(3)$ model as a function of z_1 with $m_0 = 1$ and z_2 increasing.

zero. We fix the value of m_0 to 1. The region where $Arg\,[\lambda_j] = 0$ can be inferred from the non-degeneracy of the real parts. As seen from Fig. 4.7, increasing the effect of antiparticles by making z_2 bigger gradually shrinks the region of complex mass. The region of complex mass are completely washed out for high enough value of z_2 and the mass spectrum is completely real. The value of z_2 for which the eigenvalues are real is smaller for low-lying eigenstates. For example, the 3 and $\bar{3}$ eigenstates are real even when z_2 is around 0.5 but we need z_2 to be around 1 for the eigenstates corresponding to 6 and $\bar{6}$ to be completely real. When z_2 is much larger than 1, the mass spectrum will again show regions where $Arg\,[\lambda_j] \neq 0$. This can be understood from the properties of the fermion determinants: the antifermion determinant at large z_2 is equivalent to a fermion determinant whose $z_1 = 1/z_2$ is small. The spectrum at large z_2 is thus similar to that at small z_2.

We now turn to a more physical analysis of the spectrum in terms of the quark mass M and the chemical potential μ. In all cases, we set the fundamental scale-setting parameter

$m_0 = 1$. The ratio M/T is fixed at values between 0 to 5 and μ/T is varied from 0 to 6. As shown in Figs. 4.8 and 4.9, the behaviors of the mass spectrum and Polyakov loop expectation values are similar to what has been seen before, but the peak in the real part of the mass spectrum occurs near $\mu = M$, corresponding to $z_1 = 1$. As before, the eigenvalue associated with the 8 remains real throughout. When M is large compared to m_0 and μ, the spectrum is essentially that of the pure gauge theory. When μ is close to M there is again a clear region where the low-lying eigenstates are real. In this region, there are well-defined eigenvalues associated with the 3 and $\bar{3}$, and with the 6 and $\bar{6}$. Near $\mu = M$, there are also clear maxima and minima in many of the mass values. This is presumably due to a relative maximum in the overall strength of $Z(3)$ breaking at that point. Furthermore, $Tr_F P$ and $Tr_F P^\dagger$ both peak near $\mu = M$, and also cross near this point. We attribute much of the observed behavior for $M \simeq \mu$ to an approximate particle-hole symmetry associated with the transformation $z_1 \leftrightarrow 1/z_1$. In the cases we are considering $z_2 = \exp(-\beta\mu - \beta M)$ is typically less than 1. This leads to an approximate $z_1 \leftrightarrow 1/z_1$ symmetry with small corrections coming from $z_2 < 1$, with the effects of the symmetry most pronounced in the region $M \simeq \mu$. For M/T large, z_2 is always much less than one, leading to an approximate particle-hole symmetry for all μ; crossing of the Polyakov loops occurs at approximately the same value of μ/T as half-filling. For large μ, Polyakov loop expectation values go to zero, also as a consequence of the approximate symmetry. Equivalently, one can view this as due to the saturation of the quark number density at large μ. For $M/T \lesssim 0.55$, antiquark effects are significant and cannot be neglected: the low-lying spectrum is complex at half-filling.

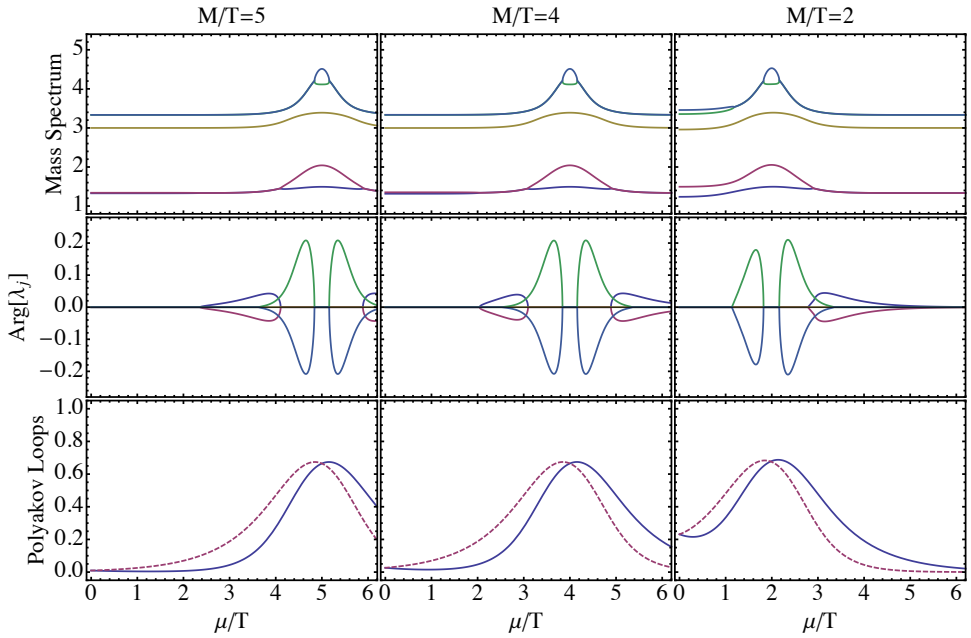

Figure 4.8: The real and imaginary parts of the mass spectrum and Polyakov loop expectation values for the $(1+1)$-dimensional $SU(3)$ model as a function of μ/T with $m_0 = 1$ and M/T between 5 and 2. The Polyakov loop $\langle Tr_F P \rangle$ is represented by a solid line, and $\langle Tr_F P^\dagger \rangle$ by a dashed line.

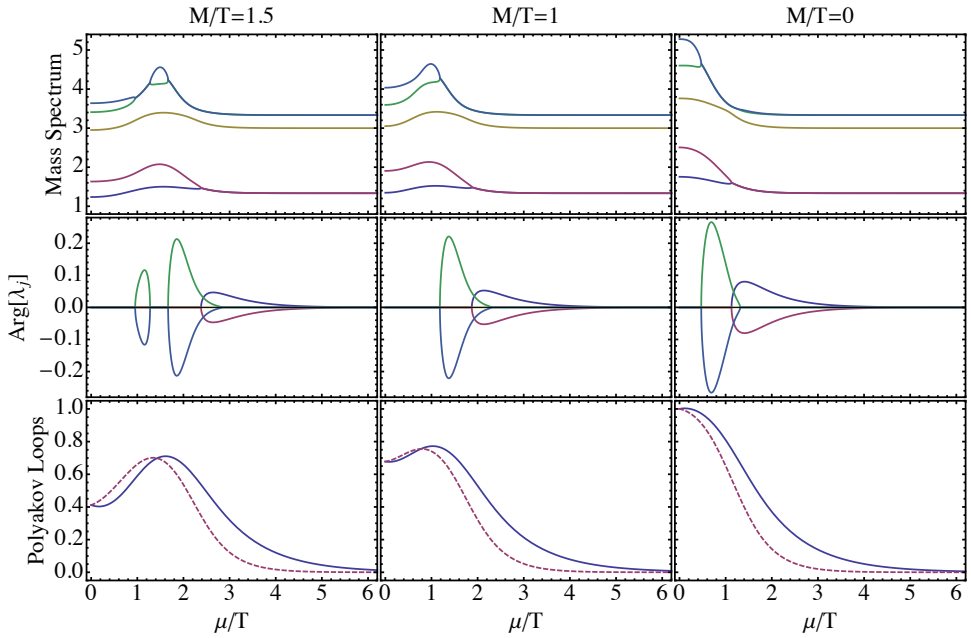

Figure 4.9: The real and imaginary parts of the mass spectrum and Polyakov loop expectation values for the $(1+1)$-dimensional $SU(3)$ model as a function of μ/T with $m_0 = 1$ and M/T between 1.5 and 0. The Polyakov loop $\langle Tr_F P \rangle$ is represented by a solid line, and $\langle Tr_F P^\dagger \rangle$ by a dashed line.

On either side of the region including $M = \mu$, where the 3 and $\bar{3}$ are real, there are regions where the value of $|Arg[\lambda_j]|$ for the 3 and $\bar{3}$ representation reaches a maximum. These regions also include the value of μ/T where $Tr_F P$ and $Tr_F P^\dagger$ are most different. A similar correlation of $|Arg[\lambda_j]|$ with $\left|\left\langle Tr_F\left(P - P^\dagger\right)\right\rangle\right|$ was seen in PNJL models [102]. As in Fig. 4.7, there is a second region where the low-lying eigenvalues are all real. This region is separate from the region around $M = \mu$ where the eigenvalues are real, and appears here for low μ/T. This behavior is clearly visible for $M/T = 2$, but is present for $M/T = 4$ and even higher values.

As may be seen from Figs. 4.8 and 4.9, the magnitude of the imaginary part of any eigenvalue is generally substantially smaller than the real part and may be difficult to observe directly in simulations. Nevertheless, it may be possible to observe the modulated decay directly in some circumstances. Figure 4.10 shows the $3 - \bar{3}$ Polyakov loop correlation function $\left\langle Tr_F P^\dagger(r)\, Tr_F P(0)\right\rangle$ as a function of r for $m_0 = 0.1$ and $z_1 = 0.08$ with $z_2 = 0$. The clear minimum at $r \simeq 22$ is a consequence of sinusoidal modulation and reminiscent of the behavior of density-density correlation functions in liquids. Note also that the correlation function drops below zero, also as a consequence of the spatial modulation.

The quark number density also may be calculated. Results are shown in Fig. 4.11 for the quark number density as a function of μ/T for $M/T = 1/2$ and $5/2$; the parameter m_0 is set to 1. The most obvious feature is the saturation of the number density at 3 for large μ. In the context of lattice gauge theories at finite density, saturation was first discussed in [113] for the case of $SU(2)$, where there is no sign problem. See [109, 114] for recent discussions

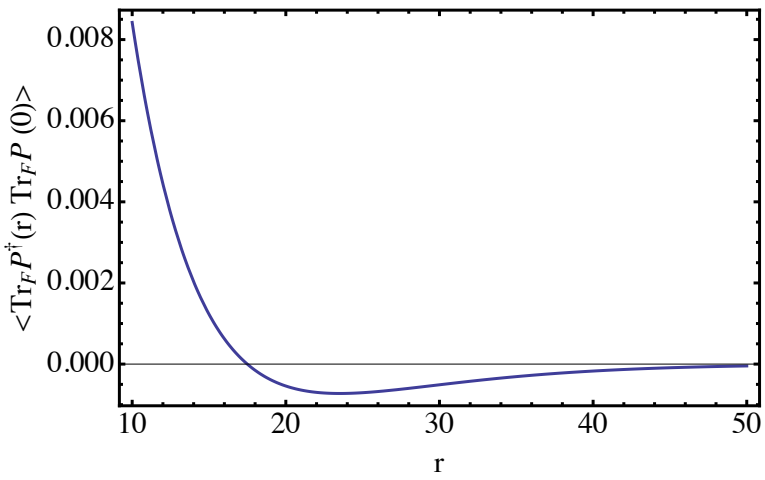

Figure 4.10: The $3-\bar{3}$ Polyakov loop correlation function $\left\langle Tr_F P^\dagger(r)\, Tr_F P(0)\right\rangle$ as a function of r for $m_0 = 0.1$ and $z_1 = 0.08$ with $z_2 = 0$.

of saturation effects in strong-coupling models of $SU(3)$ at finite density. Saturation is also observed in recent Langevin simulation with heavy quarks [95]. For the heavier quark mass $M/T = 5/2$, we expect that antiquark effects are negligible for $\mu \simeq M$, and the system has an approximate particle-hole symmetry at $M = \mu$. This in turn implies that the quark number density reaches half-filling (1.5) at $M = \mu$. As may be seen from the figure, that expectation is confirmed. For the lighter quark mass, $M/T = 1/2$, antiquark effects are not negligible when $\mu \simeq M$, and antiquark contributions lower the number density at $\mu = M$ below the half-filling value. In both cases, the number density saturates at some value of μ larger than M.

4.5 Conclusions

The spatial transfer matrix associated with Polyakov loops in finite-density QCD with static quarks have complex eigenvalues over a significant region of parameter space in strong-

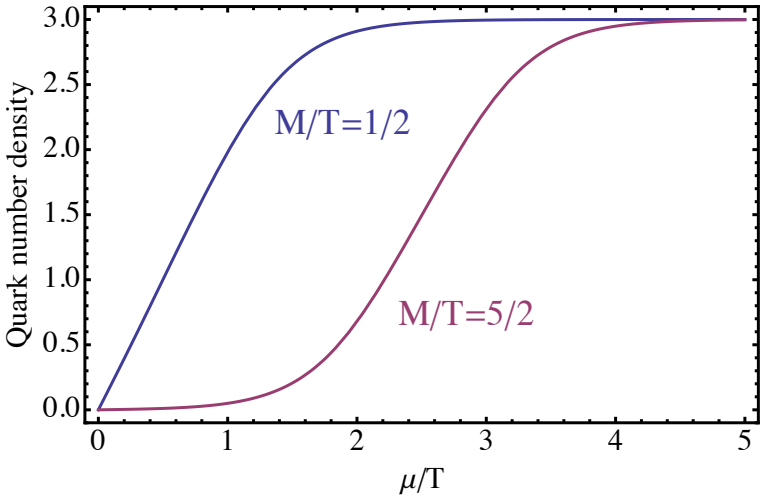

Figure 4.11: Quark number density as a function of μ/T for $M/T = 1/2$ and $5/2$. The parameter m_0 is set to 1. For the heavier mass $M/T = 5/2$, the quark number density reaches half-filling (1.5) at $M = \mu$.

coupling limit. The appearance of complex eigenvalues is a direct consequence of the non-hermiticity of the transfer matrix. This is a manifestation of the sign problem in finite-density QCD. We have given a graphical explanation of the non-hermiticity in terms of the mixing between different representations. The invariance of finite-density QCD under $\mathcal{CK}$ symmetry ensures that the eigenvalues are either real or part of complex conjugate pair. The complex conjugate pairs in turn give rise to sinusoidal modulation of Polyakov loop correlation function. If the activities z_1 and z_2 are set to a common value z, i.e. $\mu = 0$, all the eigenvalues are real. In this case, all the low-lying eigenvalues are largest when the static fermion mass M is zero, corresponding to $z = 1$. In the case where antiparticles effects are completely suppressed by setting $z_2 = 0$, the mass spectrum reflected the particle-hole symmetry of the theory under $z_1 \to 1/z_1$. As in the previous case, the real part of the transfer matrix eigenvalues peak at $z_1 = 1$, corresponding to $M = \mu$. This is a point where

the transfer matrix is Hermitian, and also the point of half-filling. The complete suppression of antiquark effects obtained by setting $z_2 = 0$ is an approximation. If z_2 were exactly zero, then we would find that: a) all mass ratios would be real at $z_1 = 1$, a property that would hold in a region around $z_1 = 1$; b) mass ratios would show maxima or minima at $z_1 = 1$; c) $Tr_F P$ and $Tr_F P^\dagger$ would cross at $z_1 = 1$. We have confirmed that these properties persist when $z_2 \ll 1$, reflecting an approximate particle-hole symmetry. As z_2 increases and antiparticle effects become more important, the regions where complex eigenvalues occur reduce in size and eventually disappear as z_2 approaches z_1.

The mass spectrum can also be analyzed in terms of the more physical parameters M/T and μ/T. In general, the spectrum of low-lying eigenvalues shows a complicated set of behaviors, with both real and complex pairs of eigenvalues occurring. When M/T is large compared to m_0 and μ/T, the spectrum obtained is essentially that of pure gauge theory, and the low-lying eigenvalues are all real. The region where μ/T is close to M/T corresponds to $z_1 = 1$, and the behavior in this region is largely determined by the approximate particle-hole symmetry discussed above. In all the cases studied, $\langle Tr_F P \rangle \leq \left\langle Tr_F P^\dagger \right\rangle$ for $0 < \mu < M$ reflecting the lower free energy cost associated with introducing antiparticles. The occurrence of conjugate complex mass pairs and sinusoidal modulation of Polyakov loop correlation functions was previously observed by us in the study of phenomenological models of QCD using a saddle point approximations [79, 102]. The presence of similar phenomenon in lattice models of QCD at strong coupling strongly suggests the generality of the phenomenon. It has been suggested [76, 77] that sinusoidal modulation of this type might be observed in

lattice simulations and heavy ion experiments. In both phenomenological models and in lattice strong-coupling calculations, the imaginary part of the mass is significantly smaller than the real part, suggesting that the direct observation of modulation might be difficult because of a long wavelength. However, there is another way to observe the splitting of the spectrum into complex pairs in lattice simulations. Suppose that the imaginary part of the masses are too small to be directly observed and can be neglected. In the regions where there are complex conjugate eigenvalue pairs, the real parts of the eigenvalues are degenerate, but outside of those regions they are different. This effect should be present and observable in lattice simulations of finite-density QCD, and may provide a strong test for finite-density algorithms.

Chapter 5

LIQUID-GAS PHASE TRANSITIONS AND $\mathcal{CK}$ SYMMETRY IN QUANTUM FIELD THEORIES

This chapter contains the materials published under the same title [1]*. This work was done in collaboration with Dr. Hiromichi Nishimura under the supervision of my advisor, Prof. Michael Ogilvie*

5.1 Introduction

The problem of determining the phase structure of interacting particles at nonzero temperature and density is old and important. Modern field-theoretic approaches are typically susceptible to the sign problem, in which basic quantities such as the action becomes complex. This problem is particularly acute in the case of QCD at finite temperature and density: Lattice simulations have given excellent first-principles results for many observables of finite-temperature QCD, there has been less clear success when the chemical potential μ is nonzero [41–43]. A central problem is the determination of the phase structure of QCD at low temperature and density where a critical line with a critical end point in the Ising, or liquid-gas, universality class is widely expected.

Here we address the generic problem of liquid-gas phase transitions from a field theory perspective. The general class of field theories we will study is the class of $\mathcal{CK}$-symmetric models obtained from dimensional reduction of a four-dimensional field theory at finite tem-

[1] Nishimura, H., Ogilvie, M.C. and Pangeni, K., 2017. Liquid-gas phase transitions and C K symmetry in quantum field theories. Physical Review D, 95(7), p.076003.

perature and density. The simplest case of interest are models with a single type of particles, interacting via a scalar field σ and a vector field A_μ. Both σ and A_μ will be taken to have masses. The potential induced by σ will be attractive, while that caused by the static vector potential A_4 will be repulsive between particles. The particles of the underlying theory are integrated out, and after dimensional reduction and redefinition of fields, we obtain a Lagrangian of the general form

$$L_{3d} = \frac{1}{2}\left(\nabla\phi_1\right)^2 + \frac{1}{2}m_1^2\phi_1^2 + \frac{1}{2}\left(\nabla\phi_2\right)^2 + \frac{1}{2}m_2^2\phi_2^2 - F\left(\phi_1, \phi_2\right) \tag{5.1}$$

where ϕ_1 is associated with the attractive force, and ϕ_2 with the repulsive force. The field ϕ_1 is naturally as a four-dimensional scalar, but ϕ_2 is obtained from the fourth component of a vector interaction. The function F can be interpreted as $\beta p\left(\phi_1, \phi_2\right)$, where β is the inverse of the tempurature T and p is a local pressure. In particular, $p\left(\phi_1, \phi_2\right)$ is the local pressure of the gas of particles in the grand canonical ensemble in the presence of the background fields ϕ_1 and ϕ_2.

The key feature of L_{3d} is that it is not real, but instead satisfies the $\mathcal{CK}$ symmetry condition

$$L_{3d}(\phi_1, \phi_2)^* = L_{3d}(\phi_1, -\phi_2). \tag{5.2}$$

The $\mathcal{C}$ transformation naturally takes $\phi_2 \to -\phi_2$ as in the case of QED, and the ϕ_1 field is left invariant. A nonzero chemical potential μ explicitly breaks C symmetry, but the antilinear symmetry $\mathcal{CK}$ remains [70, 79, 102, 115]. $\mathcal{CK}$ symmetry implies that the saddle points of L_{3d}

have ϕ_2 purely imaginary; at these saddle points, L_{3d} is real. Analytic continuation of the fields into the complex plane leads to a resolution of the sign problem at tree level. More generally, unbroken $\mathcal{CK}$ symmetry implies that the expected value of $\langle\phi_2\rangle$ must be zero or purely imaginary, because $\langle i\phi_2\rangle^* = \langle i\phi_2\rangle$.

The static solutions of the equations of motion take the form

$$m_1^2\phi_1 = \frac{\partial F}{\partial \phi_1} \tag{5.3}$$

$$m_2^2\phi_2 = \frac{\partial F}{\partial \phi_2}. \tag{5.4}$$

The presence of such a $\mathcal{CK}$ symmetry is generic in quantum field theories at finite density. The mass matrix for ϕ_1 and ϕ_2 is given by

$$\begin{pmatrix} m_1^2 - \frac{\partial^2 F}{\partial \phi_1^2} & -\frac{\partial^2 F}{\partial \phi_1 \partial \phi_2} \\ -\frac{\partial^2 F}{\partial \phi_2 \partial \phi_1} & m_2^2 - \frac{\partial^2 F}{\partial \phi_2^2} \end{pmatrix}. \tag{5.5}$$

The mass matrix is nonhermitian because the off-diagonal elements are purely imaginary at the saddle point, where ϕ_2 is imaginary. It does, however, inherit the $\mathcal{CK}$ symmetry of the underlying model. This in turn implies that the eigenvalues of the mass matrix are either both real or form a complex conjugate pair [70, 79, 102, 115] . The boundary of the region where complex conjugate pairs occur is given by

$$\left(m_1^2 - \frac{\partial^2 F}{\partial \phi_1^2} - m_2^2 + \frac{\partial^2 F}{\partial \phi_2^2}\right)^2 + 4\left(\frac{\partial^2 F}{\partial \phi_1 \partial \phi_2}\right)^2 = 0. \tag{5.6}$$

The occurence of complex conjugate pairs of mass eigenvalues in turn lead to the damped sinusoidal density oscillations often associated with the presence of a liquid phase. Thus we see that this formalism can give a simple understanding of the existence of disorder lines, which mark a change in the behavior of the potential between particles from exponential to damped sinusoidal behavior. This behavior cannot be obtained from field theories with real actions.

One of the hallmarks of typical liquid-gas systems is the existence of regions in parameter space where density-density correlation functions exhibit damped oscillatory behavior. From the perspective of quantum field theory, the appearance of damped oscillatory behavior in correlation functions is unusual. Such behavior is prohibited in Euclidean quantum field theories with spectral positivity. The simpest model of the liquid-gas transition, the Ising model in its binary alloy form, has spectral positivity and cannot exhibit damped oscillatory behavior of its correlation functions. Damped oscillatory behavior occurs generally in the class of models we consider whenever a first-order critical line occurs.

We will consider four different models, corresponding to four different choices for the function $F(\phi_1, \phi_2)$. In the next section, we will consider the case of relativistic fermions of mass m, with F taken to be

$$F = \int \frac{d^3k}{(2\pi)^3} \log\left[1 + \exp\left(-\beta\sqrt{k^2 + (m - g\beta^{-1/2}\phi_1)^2} + \beta\mu + i\beta^{1/2}e\phi_2\right)\right]. \tag{5.7}$$

The coupling constants g and e determine the strength of the attractive and repulsive forces respectively. There is a natural nonrelativistic limit, where after redefinition of the chemical

potential we have

$$F = \int \frac{d^3k}{(2\pi)^3} \log\left[1 + \exp\left(-\beta k^2/2m + \beta\mu + \beta^{1/2} g\phi_1 + i\beta^{1/2} e\phi_2\right)\right]. \tag{5.8}$$

Although the case of relativistic fermions exhibits a first-order liquid-gas transition, the nonrelativistic reduction does not. The third section considers the case of static fermions, where

$$F = \frac{1}{v} \log\left[1 + \exp\left(-\beta m + \beta\mu + \beta^{1/2} g\phi_1 + i\beta^{1/2} e\phi_2\right)\right] \tag{5.9}$$

where v is a parameter with dimensions of volume. This model also has a first-order liquid gas transition. However, its low-density reduction, the classical gas with

$$F = \frac{1}{v} \exp\left(-\beta m + \beta\mu + \beta^{1/2} g\phi_1 + i\beta^{1/2} e\phi_2\right) \tag{5.10}$$

does not have a first-order transition and does not have stable ground state. On the other hand, its partition function is exactly equivalent to that of a classical gas, as we show in an appendix. A final section gives our conclusions.

5.2 Relativistic Fermions

In this section, we study the liquid-gas phase transition in a model of relativistic fermions. We begin by showing how an effective three-dimensional field theory can be derived from a fundamental field theory. This approach is general and can be applied to other models as well, such as relativistic or nonrelativistic bosons.

5.2.1 Derivation from fundamental field theory

We consider a relativistic fermion interacting with a scalar field σ of mass m_σ and a vector field A_μ of mass m_A. These fields couple to the fermion with coupling g and e respectively. The Lagrangian for the fermionic part is

$$L_F = \bar{\psi}\left[i\gamma \cdot (\partial - ieA - \mu\hat{e}_4) - (m - g\sigma)\right]\psi \tag{5.11}$$

where m is the fermion mass. The bosonic part is given by

$$L_B = \frac{1}{2}(\partial\sigma)^2 + \frac{1}{2}m_\sigma^2\sigma^2 + \frac{1}{4}F_{\mu\nu}^2 + \frac{1}{2}m_A^2A_\mu^2. \tag{5.12}$$

This can be considered to be a QED version of the PNJL model, that is, a PNJL model where the gauge symmetry is $U(1)$. We set the boson masses m_σ and m_A to be constant, although in practical applications of the formalism they may be temperature dependent. Any expected value for the boson fields σ and A_μ (actually the associated Polyakov loop) are induced in this model by the effects of the fermions at finite temperature and density. That said, it is completely straightforward to include potential terms for σ and A_4 that can produce a more complicated phase structure. For example, a potential for σ could give rise to the analog of the chiral transition in NJL and PNJL models. In this model, however, the liquid-gas transition is driven solely by the interactions between the fermions.

The finite-temperature one-loop effective potential in the presence of constant fields σ and A_4 takes the form

$$S_{eff} = \int d^d x \left[V_\phi + V_A + V_{FT} \right] \tag{5.13}$$

where the temperature-dependent part of the one-loop fermionic contribution to the effective potential V_{FT} is given by

$$V_{FT} = -\frac{1}{\beta} \int \frac{d^3 k}{(2\pi)^3} \log \left[1 + \exp \left(-\beta \sqrt{k^2 + (m - g\sigma)^2} + \beta\mu + i\beta e A_4 \right) \right] \tag{5.14}$$

and V_σ and V_A are quadratic. Although there are also contributions from thermal excitations of σ and A_μ, we ignore them here because they do not affect the phase structure. For simplicity, we generally assume that μ is sufficently large that the antiparticle contribution can be suppressed. However, in the case of relativistic fermions, antiparticle effects must be included to obtain the correct phase structure near $\mu = 0$, so in this case antiparticle effects are included. For comparison with the other models, we do no denote these effect explicitly here. The potential V_{FT} is nothing but the negative of the pressure of a relativistic fermion moving in the constant background provided by σ and A_4. For slowly varying fields σ and A_μ, V_{FT} represents the lowest order fermionic contribution in a derivative expansion of the effective action [116]. We have also assumed that the spatial part of the vector field can be neglected, so that only the timelike component of A_μ need be included.

We dimensionally reduce to a three-dimensional effective theory, yielding an effective Lagrangian L_{3d} of the form

$$L_{3d} = \beta L_B + \beta V_{FT}.$$

We define new variables $\phi_1 = \beta^{1/2}\sigma$ and $\phi_2 = \beta^{1/2}A_4$ so as to maintain the canonical kinetic terms and also set $m_1 = m_\sigma$ and $m_2 = m_A$, giving

$$\begin{aligned} L_{3d} &= \frac{1}{2}\left(\nabla\phi_1\right)^2 + \frac{1}{2}m_1^2\phi_1^2 + \frac{1}{2}\left(\nabla\phi_2\right) + \frac{1}{2}m_2^2\phi_2^2 \\ &\quad - \int \frac{d^3k}{\left(2\pi\right)^3}\log\left[1 + \exp\left(-\beta\sqrt{k^2 + \left(m - g\beta^{-1/2}\phi_1\right)^2} + \beta\mu + i\beta^{1/2}e\phi_2\right)\right] \end{aligned} \tag{5.15}$$

The last term in the expression is the definition of $F(\phi_1, \phi_2)$ for this model.

5.2.2 Phase structure and disorder lines

The phase structure of the model is obtained from the static solutions of the equations of motion:

$$m_1^2\phi_1 = \frac{\partial F}{\partial\phi_1} \tag{5.16}$$

$$m_2^2\phi_2 = \frac{\partial F}{\partial\phi_2} \tag{5.17}$$

while the presence of disorder lines is determined from the mass matrix

$$\begin{pmatrix} m_1^2 - \frac{\partial^2 F}{\partial\phi_1^2} & -\frac{\partial^2 F}{\partial\phi_1\partial\phi_2} \\ -\frac{\partial^2 F}{\partial\phi_2\partial\phi_1} & m_2^2 - \frac{\partial^2 F}{\partial\phi_2^2} \end{pmatrix}. \tag{5.18}$$

In addition to T and μ, all of the models we consider have five parameters: m, m_1, m_2, $e$and g. This is a very large parameter space to explore. In general, the potential takes the form $F(\phi_1, \phi_2) \to F(g\phi_1, e\phi_2)$. In terms of the rescaled fields $\tilde{\phi}_1 = g\phi_1$ and $\tilde{\phi}_2 = e\phi_2$, we can write

the eqution of motion as

$$\frac{1}{\kappa_1}\tilde{\phi}_1 = \frac{\partial F}{\partial \tilde{\phi}_1} \tag{5.19}$$

$$\frac{1}{\kappa_2}\tilde{\phi}_2 = \frac{\partial F}{\partial \tilde{\phi}_2} \tag{5.20}$$

where $\kappa_1 = g^2/m_1^2$ and $\kappa_2 = e^2/m_2^2$. It is then clear that in addition to T and μ, only three parameters, κ_1, κ_2 and m determine the solution as well as the location of the critical line if there is one. On the other hand, the equation for the disorder line becomes

$$\left[\left(\frac{1}{\kappa_1} - \frac{\partial^2 F}{\partial \tilde{\phi}_1^2}\right) - \frac{e^2}{g^2}\left(\frac{1}{\kappa_2} - \frac{\partial^2 F}{\partial \tilde{\phi}_2^2}\right)\right]^2 + 4\frac{e^2}{g^2}\left(\frac{\partial^2 F}{\partial \tilde{\phi}_1 \partial \tilde{\phi}_2}\right)^2 = 0 \tag{5.21}$$

so the disorder line depends on the additional parameter of e/g. Because we are interested in conventional liquid gas transitions, we will choose the fermion mass m to be substantially heavier than the masses m_1 and m_2. In all the models we consider, we set $m = 20$, $\kappa_1 = 1$, and $e = 0.3$, and we then vary the value of κ_2 to see the change of phase diagramas, as well as the value of $g = m_1$ to observe the difference in disorder lines.

Generally speaking, the liquid-gas transition will occur for low temperatures and $\mu \lesssim m$. The left-hand graph of Figure 5.1 shows the phase diagram for $m = 20$, $m_1 = 1$ and $m_2 = 0.75$. The couplings are given by $e = 0.3$ and $g = 1$. The shaded region indicates where the mass matrix eigenvalues form complex conjugate pairs, and the contour lines refer to the imaginary parts of the mass matrix eigenvalues. The boundary of the shaded region defines the disorder line in the phase diagram. The thick line shows a first-order line

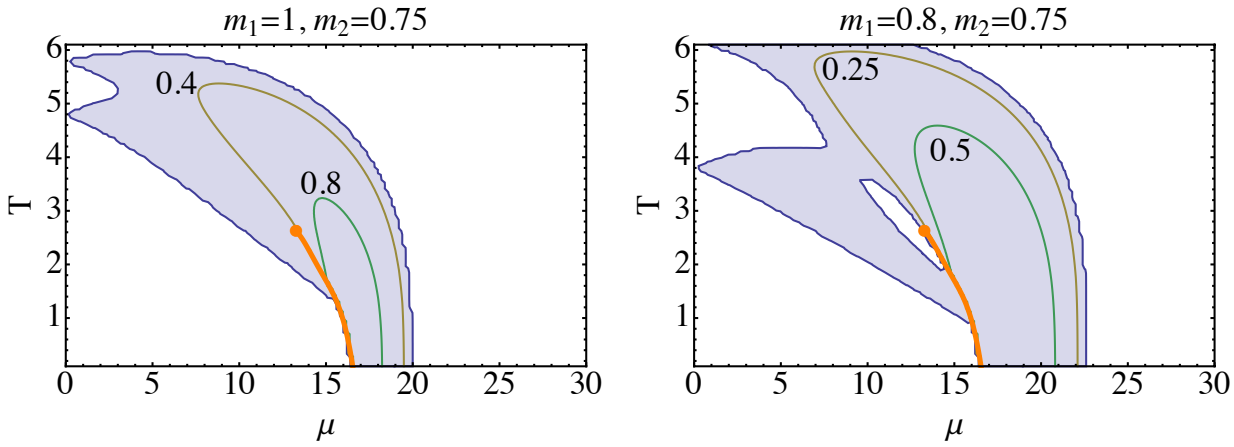

Figure 5.1: Phase diagrams for relativistic fermions for $m = 20$ and $m_2 = 0.75$ with $e = 0.3$. In the first graph $g_1 = m_1 = 1$, while in the second $g_1 = m_1 = 0.8$. The shaded region indicates where the mass matrix eigenvalues form complex conjugate pairs, and the contour lines refer to the imaginary parts of the mass matrix eigenvalues. The boundary of the shaded region defines the disorder line in the phase diagram. Note the appearance of a second disorder line inside the first in the second graph. The thick line shows a first-order line emerging from the $T = 0$ axis and terminating in a critical end point.

emerging from the $T = 0$ axis and terminating in a critical end point. The disorder line has a somewhat surprising shape; we will return to this point later. The graph on the right-hand side of the figure shows what happens if m_1 and g are decreased to 0.8. The phase structure is essentially unchanged, and the old disorder line has changed only slightly. However, a new disorder line boundary has opened up near the critical end point, inside the region where complex mass matrix eigenvalues were previously found.

In Figure 5.2, we show a second pair of phase diagrams. The graph on the left-hand side has $m_1 = g = 1$ and $m_2 = 0.5$. As before, $e = 0.3$ and $m = 20$. The end point of the critical line is at a lower value of T and slightly shifted to the right, but is otherwise similar to the previous graphs. However, when we examine the eigenvalues of the mass matrix, we see

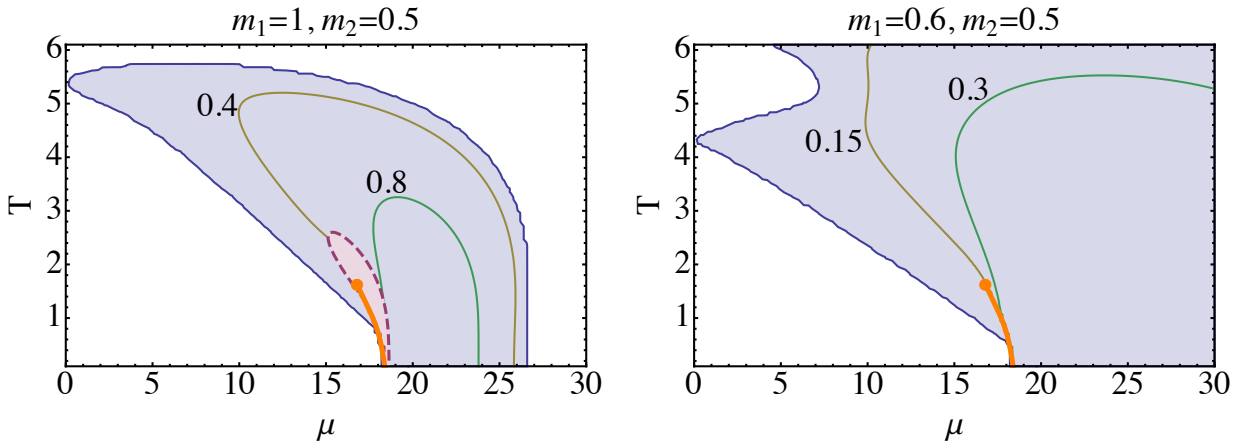

Figure 5.2: Phase diagrams for relativistic fermions for $m = 20$ and $m_2 = 0.5$ with $e = 0.3$. In the first graph $g_1 = m_1 = 1$, while in the second $g_1 = m_1 = 0.6$. The shaded region indicates where the mass matrix eigenvalues form complex conjugate pairs, and the contour lines refer to the imaginary parts of the mass matrix eigenvalues. The boundary of the shaded region defines the disorder line in the phase diagram. In the first graph, the dashed line near the critical end point is the boundary of the regions where the real parts of the mass matrix eigenvalues are negative. The thick line shows a first-order line emerging from the $T = 0$ axis and terminating in a critical end point.

something new: the real part of conjugate pair of mass matrix eigenvalues becomes negative in a region near the critical end point. This is not neccesarily unphysical behavior. The mass matrix is the matrix of squared masses, which are in general complex. A sufficiently large phase in the complex mass will lead to a squared mass eigenvalue with a negative real part. The boundary of this region is denoted in the figure by a dashed line. We have checked carefully for alternative possibilities and have concluded that this is likely to represent the correct phase structure of the model. We will return to this point in our conclusions after examining results from the other models. The graph on the right-hand side of the figure has $m_1 = g = 0.6$ and again has $m_2 = 0.5$, $e = 0.3$ and $m = 20$. The lower values of g and m_1 eliminate the region where the real part of the conjugate pair of mass matrix eigenvalues

becomes negative. The shaded region becomes larger, but the values of the imaginary parts become smaller.

5.2.3 Nonrelativistic Fermions

The case of nonrelativistic fermions can be obtained straightforwardly from the relativistic case, yielding the effective Lagrangian

$$\begin{aligned} L_{3d} &= \frac{1}{2}\left(\nabla\phi_1\right)^2 + \frac{1}{2}m_1^2\phi_1^2 + \frac{1}{2}\left(\nabla\phi_2\right) + \frac{1}{2}m_2^2\phi_2^2 \\ &\quad - \int \frac{d^3k}{\left(2\pi\right)^3} \log\left[1 + \exp\left(-\beta k^2/2m + \beta\mu - \beta m + \beta^{1/2} g\phi_1 + i\beta^{1/2} e\phi_2\right)\right]. \end{aligned} \tag{5.22}$$

An important simplification occurs because the fields ϕ_1 and ϕ_2 appear in F only as the combination $\Phi = \beta^{1/2} g\phi_1 + i\beta^{1/2} e\phi_2$. The equations of motion for static solutions become

$$\phi_1 = \frac{\beta^{1/2} g}{m_1^2}\frac{\partial F}{\partial \Phi} \tag{5.23}$$

$$\phi_2 = i\frac{\beta^{1/2} e}{m_2^2}\frac{\partial F}{\partial \Phi}. \tag{5.24}$$

Combining these equations , we obtain

$$\Phi = \left(\frac{\beta g^2}{m_1^2} - \frac{\beta e^2}{m_2^2}\right)\frac{\partial F}{\partial \Phi}. \tag{5.25}$$

Defining

$$\kappa = \kappa_1 - \kappa_2 = \frac{g^2}{m_1^2} - \frac{e^2}{m_2^2} \tag{5.26}$$

we see that the phase diagram is determined by the single equation

$$\Phi = \beta\kappa \frac{\partial F}{\partial \Phi} \tag{5.27}$$

with the four parameters m_1, m_2, e and g collapsing into a single parameter κ. The solutions of this equation are extrema of the synthetic potential

$$U = \frac{1}{2}\Phi^2 - \beta\kappa F\left(\Phi\right). \tag{5.28}$$

This simplification also holds for static and classical particles as well.

Unlike the case of relativistic fermions, we find no liquid-gas transition in the case of nonrelativistic fermions. This can be very simply from the behavior of the potential U, which always has a single minimum.

5.3 Static Fermions

In this section, we study the behavior of static continuum fermions, which have no kinetic energy. The potential is given by

$$V_{static} = -\frac{1}{\beta v}\log\left[1 + \exp\left(-\beta m + \beta g\sigma + \beta\mu + i\beta e A_4\right)\right] \tag{5.29}$$

where v should be thought of as some volume associated with the particle. For lattice models, this is a natural limit at nonzero temperature where very heavy particles are fixed on a spatial lattice site. For continuum field theories, there is no systematic approximation

which yields static fermions as a natural limit. Aside from the connection with lattice gauge theory, there are nevertheless good reasons to consider this model. The lattice form of this model was studied by Park and Fisher as a tool for demonstrating that the repulsive-core phase transition at negative $z \equiv \exp\beta\left(\mu - m\right)$ is in the $i\phi^3$ universality class [117]. The continuum model plays a similar role, illustrating both a liquid-gas transition in the usual Ising universality class and a repulsive-core transition in the $i\phi^3$ universality class for $z < 0$. The model is also interesting because it has an exact particle-hole symmetry that allows us to determine analytically the location of the critical line as well as some of the other key features of the model. This model reduces to the classical model in the limit where $z \exp\Phi \ll 1$. In that case the parameter v can be identified as $\lambda_T^3 = (2\pi/mT)^{3/2}$, but that identification is special to the low-density limit.

The dimensionally reduced effective Lagrangian L_{3d} has the form

$$L_{3d} = \frac{1}{2}\left(\nabla\phi_1\right)^2 + \frac{1}{2}m_1^2\phi_1^2 + \frac{1}{2}\left(\nabla\phi_2\right)^2 + \frac{1}{2}m_2^2\phi_2^2 - \frac{1}{v}\log\left[1 + \exp\left(-\beta m + \beta^{1/2}g\phi_1 + \beta\mu + i\beta^{1/2}e\phi_2\right)\right]. \tag{5.30}$$

As was the case with nonrelativistic fermions, the crucial simplifying feature of this model, is that F depends on ϕ_1 and ϕ_2 only through $\Phi = \beta^{1/2}g\phi_1 + i\beta^{1/2}e\phi_2$. The static equations of motion reduce to

$$\Phi = \beta\kappa\frac{\partial F}{\partial\Phi} \tag{5.31}$$

which in this case can be written as

$$\Phi = \left(\frac{\beta\kappa}{v}\right) \frac{\partial}{\partial\Phi} \log\left[1 + z\exp\left(\Phi\right)\right]. \tag{5.32}$$

The corresponding potential U takes the form

$$U = \frac{1}{2}\Phi^2 - \kappa y \log\left[1 + z\exp\left(\Phi\right)\right] \tag{5.33}$$

where we have introduced for convenience $y = \beta/v$.

This model has a conventional liquid-gas transtion for $\kappa y > 0$ and $z > 0$. We can locate the critical point of this model analytically. The second derivative of the potential $d^2U/d\Phi^2$ has two inflection points when $\kappa y > 4$; hence the potential U itself has two minima for $\kappa y > 4$. At the critical end point, the minimum of the potential coalesces with the two inflection points and one finds the critical end point at $(\kappa y = 4, z = e^{-2})$. Note that for $\kappa < 0$, there is a phase transition for $z < 0$; this transition is in the $i\phi^3$ universality class as discussed by Park and Fisher[117]. As they show, the phase structure may also be understood graphically. The equation $\partial U/\partial\Phi = 0$ may easily be written in the form

$$\Phi\exp\left(-\Phi\right) = \kappa y z - z\Phi \tag{5.34}$$

and the solutions found from the intersection of the left- and right-hand sides.

5.3.1 Particle-Hole Duality

Analytic information about the phase structure may be obtained from an exact dualtity argument [115] that exchanges particle and holes. We can rewrite U as

$$U = \frac{1}{2}\Phi^2 - \kappa y \log\left[1 + z^{-1}e^{-\Phi}\right] - \kappa y \Phi - \kappa y \log z \tag{5.35}$$

or

$$U = \frac{1}{2}\left(\Phi - \kappa y\right)^2 - \kappa y \log\left[1 + z^{-1}e^{-\Phi}\right] - \kappa y \log z - \frac{1}{2}\left(\kappa y\right)^2. \tag{5.36}$$

After shifting $\Phi \to \Phi' = -\Phi + \kappa y$, we have

$$U = \frac{1}{2}\Phi^2 - \kappa y \log\left[1 + z^{-1}e^{\Phi - \kappa y}\right] - \kappa y \log z - \frac{1}{2}\left(\kappa y\right)^2 \tag{5.37}$$

so the phase structure as revealed by Φ is invariant under

$$z \to z' = z^{-1}e^{-\kappa y} \tag{5.38}$$

$$\Phi \to \Phi' = -\Phi + \kappa y \tag{5.39}$$

These results can be extended to the potential V, where the duality transformation acts on ϕ_1 and ϕ_2 as

$$\phi_1 \quad \to \quad \phi_1' = -\phi_1 + \frac{\beta^{1/2} g}{v m_1^2} \tag{5.40}$$

$$\phi_2 \;\rightarrow\; \phi_2^{'} = -\phi_2 + \frac{i\beta^{1/2}e}{vm_2^2} \tag{5.41}$$

consistent with the duality transformation of Φ.

The critical line must map into itself under this transformation and thus must form part of the curve

$$z = e^{-\kappa y/2}. \tag{5.42}$$

This is

$$\mu = m - \frac{\kappa}{2v} = m - \frac{1}{2v}\left(\frac{g^2}{m_1^2} - \frac{e^2}{m_2^2}\right). \tag{5.43}$$

The critical end point at $(\kappa y = 4, z = e^{-2})$ lies on the critical line and maps onto itself under duality. In more physial units, we have for the critical end point $T_{cep} = \kappa/4v$ and $\mu_{cep} = m - 2T_{cep}$. Along the critical line, the jump in Φ is given by

$$\Delta\Phi = \Phi - \Phi' = 2\Phi - \kappa y. \tag{5.44}$$

This is zero at the critical end point, which must occur when $\Phi = \kappa y/2$, consistent with the location of the critical end point.

The disorder lines associated with the mass matrix

$$\begin{pmatrix} m_1^2 - \frac{\partial^2 F}{\partial \phi_1^2} & -\frac{\partial^2 F}{\partial \phi_1 \partial \phi_2} \\ -\frac{\partial^2 F}{\partial \phi_2 \partial \phi_1} & m_2^2 - \frac{\partial^2 F}{\partial \phi_2^2} \end{pmatrix} \tag{5.45}$$

occur when the two eigenvalues are degenerate. Using the fact is a function of Φ, we arrive

after some algebra at the condition

$$m_1^2 - m_2^2 - \beta \left(g \pm e\right)^2 \frac{\partial^2 F}{\partial \Phi^2} = 0. \tag{5.46}$$

This equation for the disorder lines holds whenever F is a function only of Φ rather than ϕ_1 and ϕ_2 separately; this includes the cases of the nonrelativistic fermionic gas and the classical gas as well as the case of static fermions. For static fermions, this equation may be written as

$$m_1^2 - m_2^2 - \beta \left(g \pm e\right)^2 \frac{1}{v} \frac{z \exp \Phi}{\left(1 + z \exp \Phi\right)^2} = 0. \tag{5.47}$$

Because the first term in the sum is always postive and the second and third terms are always negative, we must have $m_1 \geq m_2$ for disorder lines to appear. The appearance of a factor $\left(g \pm e\right)^2$ in the third term makes possible the appearance of two distinct disorder lines, defining two distinct boundaries for the region where the mass matrix eigenvalues have imaginary parts. The negative contribution of the third term is larger in magnitude for the combination $g + e$; this indicates that it is possible to have zero, one or two disorder lines.

5.3.2 Phase structure and disorder lines

As we did in the case of relativistic fermions, we will choose the fermion mass m to be substantially heavier than the masses m_1 and m_2, with $m = 20$. The left-hand graph of Figure 5.3 shows the phase diagram for $m = 20$, $m_1 = 1$ and $m_2 = 0.75$. The couplings are given by $e = 0.3$ and $g = 1$. These are exactly the same values as those used for the first

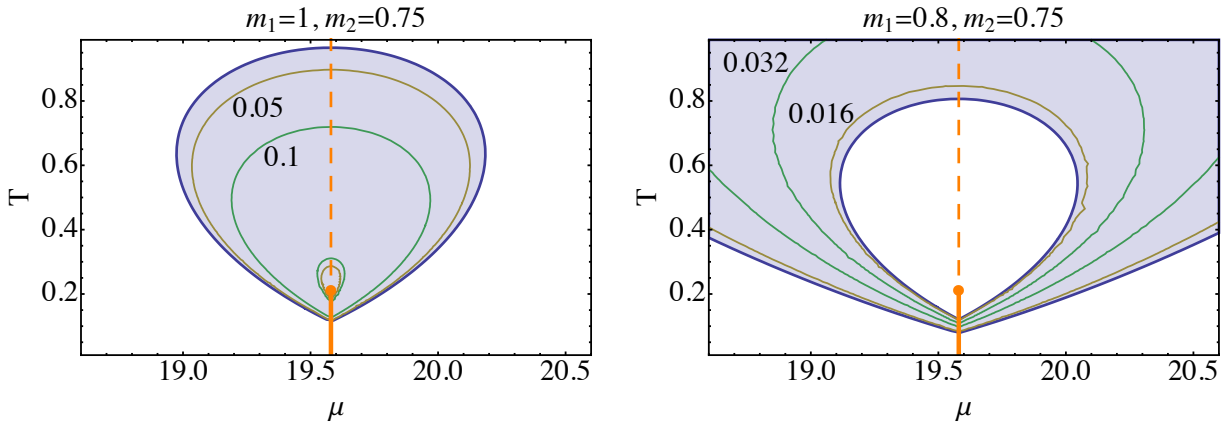

Figure 5.3: Phase diagrams for static fermions for $m = 20$ and $m_2 = 0.75$ with $e = 0.3$. In the first graph $g_1 = m_1 = 1$, while in the second $g_1 = m_1 = 0.8$. The shaded region indicates where the mass matrix eigenvalues form complex conjugate pairs, and the contour lines refer to the imaginary parts of the mass matrix eigenvalues. The boundary of the shaded region defines the disorder line in the phase diagram. Note the appearance of a second disorder line inside the first in the second graph. The thick line shows a first-order line emerging from the $T = 0$ axis and terminating in a critical end point. The dashed vertical line emerging from the critical end point is the line of particle-hole duality.

graph in Figure 5.1. We set $v = 1$ throughout. The vertical line is the line of particle-hole self-duality; the lower portion of this line is a line of first-order phase transitions, terminated by a critical end point. The shaded region again indicates where the mass matrix eigenvalues form complex conjugate pairs, and the contour lines refer to the imaginary parts of the mass matrix eigenvalues. The reflection symmetry of the diagram about the self-dual line is due to particle-hole duality. With these parameters, we see that there is a single disorder line. The graph on the right-hand side of the figure shows what happens if m_1 and g are decreased to 0.8 while m_2 is set to 0.75. As was the case with relativistic fermions, the phase structure is essentially unchanged, but a new disorder line boundary has opened up around the critical end point, inside the region where complex mass matrix eigenvalues were previously found.

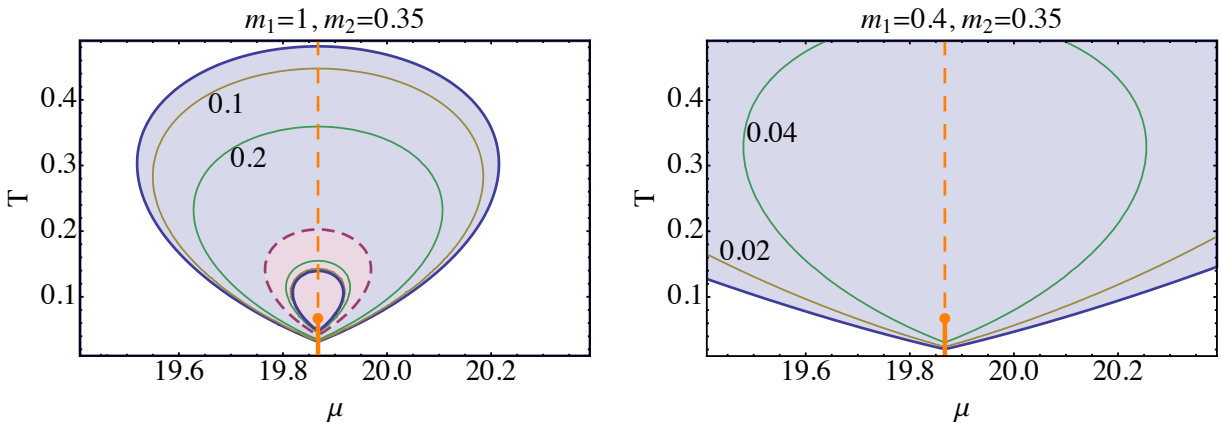

Figure 5.4: Phase diagrams for static fermions for $m = 20$ and $m_2 = 0.35$ with $e = 0.3$. In the first graph $g_1 = m_1 = 1$, while in the second $g_1 = m_1 = 0.4$. The shaded region indicates where the mass matrix eigenvalues form complex conjugate pairs, and the contour lines refer to the imaginary parts of the mass matrix eigenvalues. The boundary of the shaded region defines the disorder line in the phase diagram. In the first graph, the dashed line near the critical end point is the boundary of the regions where the real parts of the mass matrix eigenvalues are negative. The thick line shows a first-order line emerging from the $T = 0$ axis and terminating in a critical end point. The dashed vertical line emerging from the critical end point is the line of particle-hole duality.

In Figure 5.4, we show a second pair of phase diagrams. The graph on the left-hand side has $m_1 = g = 1$ and $m_2 = 0.35$. As was the case with relativistic fermions, we find a small region around the critical end point where real parts of the eigenvalues of the mass matrix become negative. The boundary of this region is again denoted by a dashed line. The graph on the right-hand side of the figure has $m_1 = g = 0.4$ and $m_2 = 0.35$. The lower values of g and m_1 again eliminate the region where the real part of the conjugate pair of mass matrix eigenvalues becomes negative. The shaded region becomes larger, but the values of the imaginary parts become smaller. This behavior is again similar to what we found for relativistic fermions.

5.3.3 Classical Particles

It is easy to obtain the effective field theory assoiciated with the classical gas as a limit of the static fermion case. As mentioned previously, the correct behavior is obtained when $z \exp \Phi \ll 1$. The potential U can be written as

$$U = \frac{1}{2}\Phi^2 - \kappa yz \exp(\Phi). \tag{5.48}$$

The equation $\partial U/\partial \Phi = 0$ now becomes

$$\Phi \exp(-\Phi) = \kappa yz. \tag{5.49}$$

This equation is solved by the Lambert function W: $\Phi = -W\left(-\kappa yz\right)$. More intuitively, it may be solved graphically by plotting $\Phi e^{-\Phi}$, which must be κzy. It is easy to see that there is no real solution for $\kappa yz > e^{-1}$, two solutions for $0 < \kappa yz < e^{-1}$ and one solution for $\kappa yz < 0$. Nowhere do we obtain the three solutions that would be expected with a standard first-order phase transition: two local minima separated by a local maximum. We can also visualize this result by noting that U is unbounded from below for $\kappa yz > 0$, with a local maximum and local minimum when $0 < \kappa yz < e^{-1}$, and no extrema for $\kappa yz > e^{-1}$. When $\kappa yz = e^{-1}$, there is a single static solution at $\Phi = 1$. It is easy to confirm that the mass matrix has a zero eigenvalue at this point, but it is not a conventional critical point; because it is unstable at cubic order, it is more like a spinodal point, where a metastable solution becomes unstable. It has been known for some time that a straightforward application of mean field theory to the classical liquid-gas system is insufficient to recover the critical behavior [118, 119]; it is therefore perhaps unsurprising that tree-level in an equivalent field theoretic approach is also insufficient.

5.4 Conclusions

We have developed a framework for deriving and analyzing field-theoretic models of liquid-gas transtitions and applied the formalism to some important models. In this framework, it is necessary to have two or more fields to include the effects of both attractive and repulsive potentials. The presence of a repulsive potential at nonzero μ gives rise to a sign problem in this class of field theories. Although charge conjugation symmetry is explicitly broken when $\mu \neq 0$, the symmetry $\mathcal{CK}$ is unbroken, with profound consequences. One consequence of the

$\mathcal{CK}$ symmetry is that there are regions of the phase diagram where masses have imaginary parts, givin rise to damped oscillatory behavior in correlation functions. The border of these regions are disorder lines. This behavior cannot occur in conventional field theories without sign problems, as a consequence of spectral positivity.

We have found two models, relativistic fermions and static fermions, that have conventional liquid-gas transitions at tree level. In contrast, the field theories associated with nonrelativistic fermions and classical particles do not have liquid-gas transtions at tree level. The case of static fermions has proven to be very tractable due to the exact particle-hole duality found there. As in our previous work on PNJL-type models of QCD [79, 102], the critical line of the liquid-gas transition is generally found in the phase diagram near any disorder lines present, although there does not seem to be any simple universal rule. The occurence of zero, one or two disorder lines is easy to understand analytically in this model. In hindsight, the phase structure of relativistic fermions is qualitatively quite similar to that of static fermions. The absence of an exact particle-hole symmetry leads to a distortion of the features found in phase diagrams, but the overall behavior appears to be the same. Both models exhibit eigenvalues of the mass matrix with negative real parts for some regions of parameter space. Because the static fermion case is tractable, we believe that this behavior is physical, indicating regions where the phase of complex masses becomes sufficiently large. There are, however, other possibilities. It is possible that the incorrect solution is being used, or that the tree level approach fails when this occurs. Another possibility, discussed below, is that we have found regions where no equilibrium thermodynamic system exits. It

is striking that the case of relativisitic and static fermions have liquid-gas phase transitions at tree level, while nonrelativisic fermions and classical particles do not. It is not clear if this reflects some fundamental feature of the physical systems being modeled, or some limitation of the method used.

Many systems can be studied within the framework we have developed. However, we are acutely aware that not much is known about the stability of most of these systems. Sufficent conditions for the thermodynamic stability of systems of classical particles were developed some time ago by Fisher and Ruelle [120]. For example, the following conditions on the total potential $V = V_2 - V_1$ are sufficient for stability of a d-dimensional system: for some positive values of a_1 and a_2, we have

$$r < a_1 \qquad V(r) \geq C/r^{d+\epsilon} \tag{5.50}$$

$$a_1 < r < a_2 \qquad V(r) \geq -w \tag{5.51}$$

$$r > a_2 \qquad V(r) \geq -C'/r^{d+\epsilon'} \tag{5.52}$$

where C, C', w, ϵ and ϵ' are positive constants. A system with attractive and repulsive Yukawa potentials will satisfy thes conditions if $e > g$. To our knowledge, there are no similar rigorous results for other systems. On physical grounds, we expect that fermionic systems will be stable whenever the corresponding classical system is stable. Because many of the current approaches to the sign problem, including the one used here, rely on saddle points in the complex plane of unknown stability, it would be very helpful to know for which

parameter values a given system is thermodynamically stable.

Appendix

In the common case where F can be written as a function of $\Phi = \beta^{1/2} g\phi_1 + i\beta^{1/2} e\phi_2$, there is a formal equivalence between the partition function of the effective field theory and a generalized Liouville sine-Gordon field theory. This equivalence is a generalization of the equivalence of the sine-Gordon model with a Coulomb gas [121, 122]. The equivalence is proven by expanding $F(\Phi)$ in the action in a power series in z and integrating the resulting functional integrals exactly at each order in the expansion.

$$L_{3d} = \frac{1}{2}(\nabla\phi_1)^2 + \frac{1}{2}m_1^2\phi_1^2 + \frac{1}{2}(\nabla\phi_2)^2 + \frac{1}{2}m_2^2\phi_2^2 - F(\Phi). \tag{5.53}$$

The function F has a natural expansion of the form

$$F = \sum_n f_n e^{n\Phi}. \tag{5.54}$$

Expansion in the f_n leads to the interpretation of the partition function as the grand canonical partition function as a gas with multiple charges n and fugacities f_n; some of the fugacities may be negative.

For simplicity, consider the case where only the $n = 1$ term is nonzero. Writing

$$F = \frac{z}{\lambda_T^d} e^{\Phi} \tag{5.55}$$

we can expand the partition function in powers of z:,

$$Z = \int [d\phi]\, e^{-S_0} \sum_{k=0}^{\infty} \frac{1}{k!} \left(\frac{z}{\lambda_T^d} \right)^k \int d^d x_1 ... d^d x_k \exp \left[\sum_{j=1}^{k} \Phi \left(x_j \right) \right] \tag{5.56}$$

where

$$S_0 = \int d^d x \left[\frac{1}{2} \left(\nabla \phi_1 \right)^2 + \frac{1}{2} m_1^2 \phi_1^2 + \frac{1}{2} \left(\nabla \phi_2 \right)^2 + \frac{1}{2} m_2^2 \phi_2^2 \right]. \tag{5.57}$$

Interchanging functional integration and summation and performing the Gaussian functional integrals we have

$$Z = \sum_{k=0}^{\infty} \frac{1}{k!} \left(\frac{z}{\lambda_T^d} \right)^k \int d^d x_1 ... d^d x_k \exp \left\{ -\beta \sum_{k<l} \left[V_2 \left(x_k - x_l \right) - V_1 \left(x_k - x_l \right) \right] \right\} \tag{5.58}$$

where the Yukawa (screened Coulomb) potentials are determined by their Fourier transforms

$$\tilde{V}_1 \left(q \right) = \frac{g_1^2}{q^2 + m_1^2} \tag{5.59}$$

$$\tilde{V}_2 \left(q \right) = \frac{g_2^2}{q^2 + m_2^2} \tag{5.60}$$

The presence of terms in the expansion of F with $n = 1$ correspond to higher charges in the generalized Coulomb gas representation.

Chapter 6

PHYSICS OF NEUTRON STARS

The remaining chapter of this dissertation focus on the effect of large amplitude density oscillation on transport coefficients, such as the neutrino emissivity, in superfluid nuclear matter. This extreme form of nuclear matter is known to exist in neutron stars [123] with profound consequences for transport properties, many of which are strongly suppressed by the superfluidity. However, there are physical events like star quakes [124] and neutron star mergers [125] that involve high-amplitude density oscillations. It was shown in [126] that these large amplitude density oscillations can overcome the strong suppression from superfluidity or superconductivity via the mechanism called "gap-bridging". However, the calculation in [126] was an illustrative proof of principle and not directly applicable to neutron star physics. A realistic calculation that is directly relevant to neutron star physics will be presented in the next chapter. The remaining section of this chapter will introduce the basics of neutron stars and different mechanism of neutrino emission in neutron stars.

Neutron stars are formed as a result of gravitational collapse of massive stars ($>8\times$ solar mass) at the end of their lifetime [127]. Neutron stars are the smallest and densest stars known to exist with mass on the order of 1.4 times the mass of sun and radius of around 10 km. Because of their large mass and small radius they posses enormous gravitational energy, E_{grav}, on the order of 10^{53} erg and enormous surface gravity, g, on the order of 10^{14} cm s^{-2}

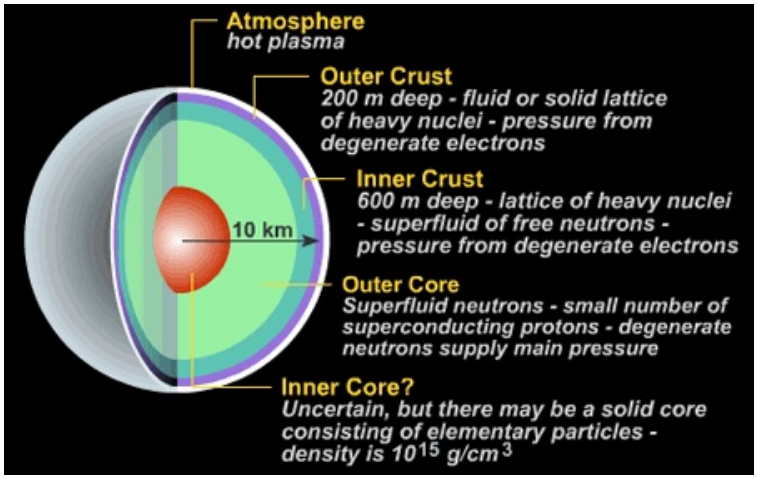

Figure 6.1: Structure of a Neutron Star.

[128]. The central density reaches about (5-10)ρ_0, where $\rho_0 = 2.8 \times 10^{14}$g cm^{-3} is the nuclear saturation density, which makes them unique astrophysical laboratories of superdense matter. They also exhibit phenomenon such as superfluidity and superconductivity with critical temperatures near 10^{10} K.

The structure of neutrons star can be subdivided into the atmosphere and four internal layers: the outer crust, inner crust, the outer core and inner core as shown in Fig. 6.1 [1]. The atmosphere is a very thin layer that varies in depth from some ten centimeters in hot stars down to millimeters in cold stars, while the outer crust with density of around 4 $\times 10^{11}$ g cm^{-3} has depth of a few hundreds of meters. The outer crust is composed mostly of degenerate electron gas and nuclei. The outer crust is followed by a several kilometers thick inner crust with density that reaches about half the nuclear saturation density (ρ_0). It is composed

[1]Figure from:http://jiaps.org/article/neutron-stars.html

mainly of degenerate neutron (could form $^1S_0$ superfluid) and electron gas with proton-rich regions. The inner crust is followed by a several kilometers deep outer core with density ranging from half the nuclear density to twice the nuclear density. This layer is composed mostly of neutrons with small admixture of uniformly distributed protons and electrons [129]. The neutrons could form a $^3P_2$ superfluid and protons a $^1S_0$ superconductor [127]. For low mass stars this outer core can extend all the way to the center. More massive stars may have a inner core region which may contain exotic phases such as pion condensation, kaon condensation and strange quark matter. See [129] for further discussion about various hypothesis on inner core composition.

The major mechanism of energy loss for a cooling neutron star is the neutrino emission. Right from its birth to about hundred thousand years, a neutron star cools mainly via the emission of neutrinos from its interiors. At later times, the star is cold so the neutrino emission is suppressed and the star cools mainly from the emission of photons from its surface [127]. Given the rich spectrum of physical conditions in different layers of the neutron star, as discussed in previous section, different neutrino emission mechanisms may be important across different crust layers for different temperature intervals. Some of the neutrino processes that takes place in neutron stars are electron-positron pair annihilation, plasmon decay, electron synchrotron and beta processes. The strongest of them is the baryon direct Urca process

$$n \to p + e^- + \bar{\nu}_e \quad , \quad p + e^- \to n + \nu_e \tag{6.1}$$

but it occurs only when the density reaches several times the nuclear saturation density, at

which point the proton and neutron Fermi momenta are sufficiently similar to allow direct conversion of one species into the other. In most if not all regions of a neutron star the direct Urca process is forbidden by energy and momentum conservation. In the absence of the direct Urca process, the main flavor-changing β process is the modified Urca process. The next chapter will describe the modified Urca process and present calculations that show the enhancement of neutrino emissivity for the case of modified Urca process in nuclear matter with $^3P_2$ neutron pairing.

Chapter 7

GAP-BRIDGING ENHANCEMENT OF MODIFIED URCA PROCESSES IN NUCLEAR MATTER

This chapter contains the materials published under the same title [1]*. This work was done by me under the supervision of Prof. Mark Alford.*

7.1 Introduction

Ultra-dense nuclear matter is believed to be a superfluid (via neutron Cooper pairing) and a superconductor (via proton Cooper pairing) for at least part of the range of densities that is relevant for neutron star physics [123, 130, 131]. This has a profound effect on transport properties, many of which are suppressed as $\exp(-\Delta/T)$ by the gap Δ in the neutron or proton spectrum. Since neutron star core temperatures T are of order 0.01 MeV [127] and Δ is typically in the MeV range [123], the suppression factor can be as strong as 10^{-40}.

It has previously been shown [126] that compression oscillations of sufficiently high amplitude can entirely overcome this suppression for certain transport properties, such as bulk viscosity and neutrino emissivity, that are dominated by flavor-changing β (weak interaction) processes. The mechanism, called "gap bridging", is a threshold-like behavior, separate from high-amplitude suprathermal enhancement of β processes [132–134]. Additional enhancement may come from the suppression of the gap itself by high-velocity flow of the superfluid

[1] Alford, M.G. and Pangeni, K., 2017. Gap-bridging enhancement of modified Urca processes in nuclear matter. Physical Review C, 95(1), p.015802.

relative to the normal fluid [135].

The previous calculation of gap bridging [126] found that oscillations with density amplitude that reached $\Delta n/\bar{n} \sim 10^{-4}$ could show gap bridging enhancement. Gap bridging is therefore expected to be relevant to high-amplitude oscillations of neutron stars such as f- or r-modes [136, 137], or the oscillations caused by star quakes [124] or neutron star mergers [125]. However, the previous calculation was an illustrative proof of principle in which the neutron pairing was assumed isotropic, in the ${}^1S_0$ channel, and only direct Urca processes were considered. In this paper we provide a more realistic calculation, obtaining the gap-bridging enhancement of the modified Urca neutrino emissivity for nuclear matter with ${}^3P_2$ neutron pairing. We find that gap bridging is just as dramatic in this realistic scenario as the original estimates indicated.

In Sec. 7.2 we describe the modified Urca process and the quantities that we will calculate to characterize the neutrino emissivity of nuclear matter. In Sec. 7.3 we calculate the modified-Urca emissivity for matter with ${}^1S_0$ pairing of neutrons. In Sec. 7.4 we calculate the modified-Urca emissivity for matter with ${}^3P_2$ pairing of neutrons. Sec. 7.5 contains our conclusions.

7.2 Modified Urca process

Urca processes change the flavor (isospin) of nucleons and emit neutrinos. They dominate certain physical properties such as bulk viscosity and neutrino emissivity. In this paper we will calculate the enhancement of the neutrino emissivity by gap bridging in high amplitude compression oscillations.

Initial work on gap bridging studied the direct Urca process because of its simplicity, but in β-equilibrated nuclear matter direct Urca processes occur only when the density reaches several times the nuclear saturation density, at which point the proton and neutron Fermi momenta are sufficiently similar to allow direct conversion of one species into the other. In most if not all regions of a neutron star the direct Urca process $n \to p\ e^-\ \bar{\nu}_e$ is forbidden by energy and momentum conservation: a neutron near its Fermi momentum p_{Fn} cannot turn into a proton near its Fermi momentum p_{Fp} and an electron near its Fermi momentum p_{Fe} because $p_{Fn} > p_{Fp} + p_{Fe}$. In the absence of the direct Urca process, the main flavor-changing β process is the modified Urca process in which a "spectator" neutron, interacting via pion exchange, absorbs the extra momentum (Fig. 7.1)

$$\begin{aligned} n + n &\to n + p + e^- + \bar{\nu}_e \\ p + n + e^- &\to n + n + \nu_e \end{aligned} \tag{7.1}$$

We neglect the modified Urca process that uses a spectator proton because it is suppressed by the lower density of protons.

The neutrino emissivity (energy radiation rate per unit volume) arising from the modified Urca process (7.1) is [129]

$$\begin{aligned} \epsilon = \int \left[\prod_{j=1}^{4} \frac{d^3P_j}{(2\pi)^3}\right] \frac{d^3P_e}{(2\pi)^3}\frac{d^3P_\nu}{(2\pi)^3}(2\pi)^4\delta(E_{\rm f} - E_{\rm i})\times \\ \times\, \delta^3(\vec{P}_{\rm f} - \vec{P}_{\rm i})E_\nu f_1 f_2(1-f_3)(1-f_4)(1-f_e)|M_{\rm fi}|^2 \end{aligned} \tag{7.2}$$

where the index j labels the four nucleon states (two neutrons in the initial state "i" and a proton and a neutron in the final state "f"); $f_j \equiv 1/\{1 + \exp[(E_j - \mu_j)/T]\}$ are the Fermi-Dirac occupation distributions for the nucleons, P_j are the nucleon momenta, P_e and E_e are the electron momentum and energy, P_ν and E_ν are the neutrino momentum and energy, and $|M_{\rm fi}|^2$ is the squared matrix element summed over spin states. In superfluid matter the matrix elements acquire coherence pre-factors (Bogoliubov coefficients) because the quasi-particles are a superposition of particles and holes. We will neglect these prefactors, which is valid when $\Delta \ll \mu$ [138, 139].

The matrix element, $|M_{\rm fi}|$ depends on the magnitude and relative orientation of the particle momenta and thus cannot be taken out of the integral. However, because of the strong degeneracy of nucleons and electrons in nuclear matter, the main contribution to the integral in Eq.(7.2) comes from the region near the Fermi surface. Therefore, we can set $|\vec{p}| = p_F$ in all smooth functions of energy and momenta. Furthermore, in the approximation where we treat the nucleons as non-relativistic and ignore the neutrino momenta as well as the electron and the proton momenta (which are all small in the region of our interest), the matrix elements turn out to be independent of the relative orientation of the particle momenta [129, 140]. This enables us to take the matrix element out of the integral. Since we will be interested in calculating the ratio of the the neutrino emissivity rate with and without superconductivity or superfluidity, the matrix element cancels out at leading order in μ_Δ/p_F expansion. Interested readers can find the expression for the matrix element in Eq. 139 of [129] and Eq. 36 of [140].

7.2.1 Effect of superfluidity

We will consider phases of nuclear matter with neutron superfluidity, with or without proton superconductivity. The superfluidity or superconductivity arises from Cooper pairing due to the attractive nuclear force between nucleons. Cooper pairing creates a gap in the energy spectrum of the particles near the Fermi surface. For nuclear matter in neutron stars the temperature is far below the Fermi energy, so only the degrees of freedom close to the Fermi surface are relevant for transport. Their dispersion relation $E_i(p_i)$ is

$$(E_i - \mu_i)^2 = v_{Fi}^2 (p_i - p_{Fi})^2 + \Delta_i^2, \tag{7.3}$$

where $i = n$ or p indexes the nucleon species, and Δ_i is the gap arising from Cooper pairing. For electrons and neutrinos we can use the free dispersion relations $E_e^2 = p_e^2 + m_e^2$ and $E_\nu = p_\nu$.

We will write the neutrino emissivity ϵ as

$$\epsilon = R_\epsilon \, \epsilon_0, \tag{7.4}$$

where ϵ_0 is the purely thermal emissivity (with no external compression oscillations) for non-superfluid matter, and R_ϵ is the "modification factor" that takes into account the effects of gaps in the fermion spectra and high amplitude effects such as suprathermal enhancement and gap bridging. As the gap rises, R_ϵ drops below 1 because of Boltzmann suppression [141] but in the presence of compression oscillations that drive the system out of beta equilibrium R_ϵ can be pushed up to very large values. The modification function R_ϵ for the modified

Urca process is

$$
\begin{aligned}
R_\epsilon = & \frac{945\, P_{Fn}^3}{92104\, \pi^{13}} \int_0^\infty dx_\nu x_\nu^3 \\
& \times \prod_{i=1}^{3} \left[\int_{-\infty}^{\infty} dx_{ni} W(x_{ni}, \Delta_n/T) \right] \\
& \times \int_{-\infty}^{\infty} dx_p W(x_p, \Delta_p/T)\ A\ \left[f(X_-) + f(X_+) \right] \\
& \times f(x_{n1}) f(x_{n2}) f(-x_{n3}) f(-x_p)\ ,
\end{aligned}
\tag{7.5}
$$

where

$$W(x,z) \equiv \frac{|x|\Theta(x^2-z^2)}{\sqrt{x^2-z^2}}, \tag{7.6}$$

$$\Theta(a) \equiv 1 \text{ if } a>0, \text{ or } 0 \text{ if } a<0, \tag{7.7}$$

$$A \equiv 4\pi \int \prod_{j=1}^{5} d\Omega_j \delta^3(\vec{P}_{\rm f} - \vec{P}_{\rm i})\ , \tag{7.8}$$

$$X_\pm \equiv x_{n3} + x_p + x_\nu - x_{n1} - x_{n2} \pm \mu_\Delta/T\ , \tag{7.9}$$

$$\mu_\Delta \equiv \mu_n - \mu_p - \mu_e\ , \tag{7.10}$$

$$f(x) \equiv 1/(1+e^x)\ , \tag{7.11}$$

$$x_i \equiv (E_i - \mu_i)/T\ . \tag{7.12}$$

The subscripts $n1$ and $n2$ refer to the incoming neutrons; $n3$ and p refer to the outgoing neutron and proton. The chemical potential μ_Δ arises from external compression oscillations that drive the system out of β equilibrium. R_ϵ is normalized so that $R_\epsilon = 1$ when all the gaps are zero and $\mu_\Delta = 0$.

We will calculate $R_{\bar{\epsilon}}$, which measures how much the emissivity is affected by nonlinear

high amplitude effects and by Cooper pairing,

$$\begin{aligned} R_{\bar{\epsilon}}(\hat{\mu}_\Delta) &= \frac{\langle \epsilon(\mu_\Delta)\rangle}{\langle \epsilon_0\rangle} = \big\langle R_\epsilon(\mu_\Delta)\big\rangle \ , \\ \mu_\Delta(t) &= \hat{\mu}_\Delta \sin(\omega t) \ , \end{aligned} \tag{7.13}$$

where $\langle X\rangle$ means the average of X over one oscillation cycle. Since ϵ_0, the emissivity in the absence of oscillations and with no Cooper pairing, is independent of μ_Δ, then $\langle \epsilon_0\rangle = \epsilon_0$.

7.3 Singlet state ($^1S_0$) pairing for both nucleons

We first consider modified-Urca neutrino emission in matter where both the neutrons and protons form Cooper pairs in the $^1S_0$ state. As we will see in Sec. 7.4, the results for the realistic case of $^3P_2$ neutron pairing are qualitatively and quantitatively similar to this case. For $^1S_0$ pairing the gap is isotropic so the angular integral A and the radial integral in Eq. (7.5) can be separated. After angular integration, the modification function is

$$\begin{aligned} R_\epsilon =& \frac{60480}{11513\pi^8}\int_0^\infty dx_\nu x_\nu^3 \\ &\times \prod_{i=1}^{3}\int_{-\infty}^{\infty} dx_{ni} W(x_{ni}, \Delta_n/T) \\ &\times \int_{-\infty}^{\infty} dx_p W(x_p, \Delta_p/T) \\ &\times f(x_{n1}) f(x_{n2}) f(-x_{n3}) f(-x_p)\big[f(X_-) + f(X_+)\big] \ . \end{aligned} \tag{7.14}$$

In Fig. 7.2 we show the effect of increasing the amplitude of the applied compression

oscillations for the case where protons and neutrons have the same $^1S_0$ gap, $\Delta_p = \Delta_n$. For low amplitude oscillations the system remains in β equilibrium ($\hat{\mu}_\Delta/\Delta_n \ll 1$) and the neutrino emissivity is very heavily suppressed by the gaps, roughly as $\exp(-2\Delta_n/T)$. As the amplitude rises, $R_{\bar{\epsilon}}$ rises due to suprathermal effects [a factor of $(\mu_\Delta/T)^8$ [133]]. On the log scale used in Fig. 7.2 this appears as a very slow, logarithmic, increase. When $\hat{\mu}_\Delta$ becomes of the same order as Δ_n, gap bridging begins to occur: some β processes start to become unsuppressed, and their rate rises exponentially (straight line on this plot). As we discuss in more detail below, this happens in two steps, until at high amplitude of the oscillations, $\hat{\mu}_\Delta/\Delta_n \approx 4$, all the Boltzmann suppression due to the gap has been overcome, and $R_{\bar{\epsilon}} \approx 1$, regardless of how low the temperature may be.

To understand the staircase-like behavior of the dependence of the emissivity on the amplitude, it is necessary to analyze the different channels that contribute to the modified Urca process. These channels are schematically shown in Fig. 7.3 and their contribution to the modification function $R_{\bar{\epsilon}}$ is shown in Fig. 7.4 where we can already see how gap bridging is manifested at different values of $\hat{\mu}_\Delta$ depending on the channel, so the sum of all the channels yields a staircase dependence on $\hat{\mu}_\Delta$.

Figure 7.3 contains 16 panels showing all the channels that contribute to the modified Urca process. Each of the two nucleons can have an initial state above or below its Fermi energy and a final state above or below its Fermi energy, yielding $2^4 = 16$ possibilities. For each channel we show the three Fermi seas in β equilibrium: from left to right, neutron (gapped), proton (gapped), electron (ungapped). We are interested in the free energy $\epsilon_i - \mu_i$

of each species i, so the Fermi energies are aligned. The black arrows show the transitions of the spectator neutron, the $n \leftrightarrow p$ conversion (arrow that goes from neutron to proton Fermi sea), and electron. The vertical length of each arrow shows the free energy input or output, so by energy conservation and beta equilibration ($\mu_n = \mu_p + \mu_e$) these add up to zero in each process. The electron line starts at the electron Fermi energy because the free energy cost of placing an electron there is zero. The length of the electron arrow then tells us the amount of energy yielded (or consumed) by the hadronic processes.

7.3.1 Rates at zero compression amplitude

The processes fall into five classes, labeled by the number below each panel. At $\hat{\mu}_\Delta = 0$ the degree of suppression of the rate for each process can be estimated by keeping track of the Boltzmann factors that arise when one tries to annihilate a fermion in a sparsely populated part of phase space, or create a fermion in a densely occupied part of phase space, according to the following rules:

$$\begin{aligned} &- \text{For each arrow starting at energy } +|E| \text{ (i.e. above the Fermi surface):} \\ &\text{a factor of } \exp(-|E|/T). \\ &- \text{For each arrow ending at energy } -|E| \text{ (i.e. below the Fermi surface): a} \\ &\text{factor of } \exp(-|E|/T). \end{aligned} \tag{7.15}$$

The result of applying this rule to each class of channel is:

$$\begin{aligned} \text{Classes 1 and 5:} \quad & \exp(-4\Delta/T) \\ \text{Classes 2 and 4:} \quad & \exp(-3\Delta/T) \\ \text{Class 3:} \quad & \exp(-2\Delta/T) \end{aligned} \tag{7.16}$$

For example, class 1 contains one channel (top left panel of Fig. 7.3). To see that this has a suppression factor of $\exp(-4\Delta/T)$, we look at each arrow in turn. The spectator neutron transitions from an occupied state at free energy $-\Delta_n$ to an unoccupied state at free energy $+\Delta_n$, so it contributes no suppression factor according to the rules. The "protagonist" neutron starts in an occupied state at free energy $-\Delta_n$ and becomes a proton in an unoccupied state at free energy $+\Delta_p$, so it also contributes no suppression factor. However, these two processes each require an energy input of 2Δ so the electron that is created by the β process must produce 4Δ by ending up in a state at free energy -4Δ which is deep in the occupied electron sea, yielding a suppression factor of $\exp(-4\Delta/T)$ which reflects the unlikeliness of finding an unoccupied state there.

We can now understand the $\hat{\mu}_\Delta = 0$ part of Fig. 7.4: channels 1 and 5 are the most suppressed, then channels 2 and 4, and finally the least suppressed is channel 3 where the nucleon transitions are energy neutral so the electron yields or requires no energy.

7.3.2 Rates as a function of compression amplitude

We now analyze the variation of the rates in the various channels in the presence of a density oscillation whose amplitude $\hat{\mu}_\Delta$ rises to values as large as $5\Delta_n$. The external compression drives the system out of β equilibrium. Under a relatively fast compression the proton and

neutron Fermi energies increase by the same fraction, but because the proton fraction in β-equilibrated matter rises with density, the proton Fermi energy is then μ_Δ below its β-equilibrated value at the higher density. This reflects the fact that the system now "wants to make more protons".

The rules are modified as follows,

— For channels where the electron is created with energy $-|E|$ (i.e. below the electron Fermi energy), its Boltzmann factor is now:
$\exp((-|E| + \mu_\Delta)/T)$, or $(\mu_\Delta/T)^8$ if $\mu_\Delta > E$.

— For channels where the electron is created with energy above the electron Fermi energy, there is an additional overall factor of $(\mu_\Delta/T)^8$ (suprathermal enhancement).

(7.17)

In channels of class 3-5, at $\hat{\mu}_\Delta = 0$ the electron is created in a state at or above the Fermi energy. There is therefore no gap-bridging, just suprathermal enhancement which multiplies the $\hat{\mu}_\Delta = 0$ rate by $(\mu_\Delta/T)^8$. On the log scale used in Fig. 7.4 this gives a very weak growth with $\hat{\mu}_\Delta$ which appears as the horizontal lines at approximately $\exp(-2\Delta/T)$ (class 3 channels), $\exp(-3\Delta/T)$ (class 4 channels) and $\exp(-4\Delta/T)$ (class 5 channels). For class 3 channels, where the electron is created at its Fermi energy, there is a small gap-bridging growth at very small amplitudes where $\mu_\Delta \sim T$.

In class 2 channels, at $\hat{\mu}_\Delta = 0$ the hadronic processes are suppressed in two ways. Firstly, there is a Boltzmann factor of $\exp(-\Delta/T)$ from either trying to place a final-state hadron in the mostly occupied states below the gap, or from finding an initial-state hadron in the

sparsely occupied states above the gap. Secondly, the hadronic processes require an energy input of 2Δ, either to move the spectator neutron up above its pairing gap, or to convert the other neutron into a proton above its pairing gap. This leads to an additional suppression by $\exp(-2\Delta/T)$ since to deliver this amount of energy the electron must be created at free energy -2Δ, deep in its occupied Fermi sea. As $\hat{\mu}_\Delta$ increases, this second factor is canceled by gap bridging: the required energy input is reduced by $\hat{\mu}_\Delta$, since the proton Fermi sea is lowered by this amount. The electron can therefore be created in a state with free energy $\hat{\mu}_\Delta - 2\Delta$, so the second Boltzmann suppression factor is reduced and eventually when $\hat{\mu}_\Delta \approx 2\Delta$ the electron has enough energy to be placed in a state above its Fermi energy where there are plenty of unoccupied states and there is no Boltzmann suppression factor. Any further increase in $\hat{\mu}_\Delta$ only results in suprathermal enhancement, with the remaining $\exp(-\Delta/T)$ (described at the start of this paragraph) which is not affected by gap bridging.

In channel 1, all the hadrons are taken from below the gap and created above the gap, so there are no Boltzmann factors associated with hadronic Fermi-Dirac distributions. However, this requires a large energy input (4Δ at $\hat{\mu}_\Delta = 0$) from the electron, which leads to a suppression factor of $\exp(-4\Delta/T)$ from forcing the electron into the heavily occupied phase space deep in its Fermi sea at a free energy of -4Δ. As $\hat{\mu}_\Delta$ rises, the proton energy states drop relative to the neutron ones, and the $n \to p$ process requires less and less energy. At $\hat{\mu}_\Delta = 2\Delta$ the process breaks even, and at $\hat{\mu}_\Delta = 4\Delta$ it can provide all the energy needed by the spectator neutron. The electron is then relieved of the requirement to subsidize the hadrons, and can be created above its Fermi energy. All Boltzmann suppression has been canceled

by gap bridging, and further increase in $\hat{\mu}_\Delta$ produces only suprathermal enhancement. In conclusion, even though this channel is the most suppressed at $\hat{\mu}_\Delta = 0$ it dominates at large $\hat{\mu}_\Delta$ because all the suppression arises from the hadronic energy requirements, which can be eliminated by gap bridging.

Up to now we have assumed that the protons and neutrons have the same pairing gap. We now explore the effect of varying the proton gap: fixing the temperature so that $\Delta_n/T = 60$, we plot the amplitude dependence of the emissivity for $\Delta_p/\Delta_n = 2,\ 1,\ 1/2,$.

In Fig. 7.5 we show the results of this variation in Δ_p. Not surprisingly, lower values of the proton gap bring the point of complete gap bridging to a lower $\hat{\mu}_\Delta/\Delta_n$. This is because at large $\hat{\mu}_\Delta/\Delta_n$ the rate is dominated by channel 1 where, as explained in the previous paragraph, all the suppression comes from the energy requirements of the hadronic processes. For the spectator neutron to jump the gap requires $2\Delta_n$ and the conversion of a neutron below the gap to a proton above the gap requires energy $\Delta_n + \Delta_p$, so the total requirement is $3\Delta_n + \Delta_p$. Thus when $\Delta_p/\Delta_n = 1/2$ full gap bridging can be achieved when $\hat{\mu}_\Delta/\Delta_n \approx 3.5$ (top curve in Fig. 7.5) rather than $4\Delta_n$ when $\Delta_p = \Delta_n$ (middle curve in Fig. 7.5)

When $\Delta_p/\Delta_n = 2$, the suppression factor is $\exp(-5\Delta_n/T)$ so a compression oscillation of magnitude $\hat{\mu}_\Delta/\Delta_n \approx 5$, is necessary for complete gap bridging.

7.4 Triplet state ($^3P_2$) neutron pairing

We now calculate the modified Urca neutrino emissivity for nuclear matter in the inner regions of a neutron star where the neutron density is high and the neutrons pair in a $^3P_2$

channel, while the proton density is relatively low and the protons pair in a $^1S_0$ channel [142]. For the neutrons there are other available triplet channels, but $^3P_0$ is only weakly attractive while the $^3P_1$ state is repulsive [123, 143]. For the $^3P_2$ channel, there is still a choice of orientation of the condensate: J_z could be 0, ± 1, ± 2. Microscopic calculations [142, 144, 145] find that $J_z = 0$ is very slightly energetically favored over the other values, however this is not conclusive because of uncertainties in the microscopic theory [146]. In the following discussion we will consider neutron condensates with $J_z = 0$ and ± 2. We expect these to show different dependencies of the emissivity on temperature and oscillation amplitude because for $J_z = 0$ all neutron states at the Fermi surface are gapped, but for $J_z = \pm 2$ there are ungapped nodes at the poles [129].

In our calculations we will assume $\Delta_p = \Delta_n$ for simplicity. In real neutron star core matter it is likely that Δ_p is significantly larger than Δ_n [131].

7.4.1 $^3P_2(J_z = 0)$ neutron pairing

For neutrons that Cooper pair in the $^3P_2$ state with $J_z = 0$, rotational symmetry is broken. There is a preferred direction in space (we will align the z axis along it) and the gap in the neutron spectrum becomes dependent on the angle θ between the momentum of the neutron quasiparticle and the z axis [142],

$$\Delta_n(\theta) = \Delta_{n0}\sqrt{1 + 3\,\cos^2(\theta)}\ . \tag{7.18}$$

Note that the gap varies between a minimum of Δ_{n0} (around the equator) and $2\Delta_{n0}$ (at the poles) but does not vanish anywhere on the Fermi surface. We therefore expect that $^3P_2$ pairing will be qualitatively similar to $^1S_0$ pairing, having the same parametric dependence of the rate on temperature and oscillation amplitude.

The dependence of the $^3P_2$ gap on θ restricts us from separating the angular and radial part of the integral in Eq. (7.5). However, the gap has no ϕ dependence so we can integrate the momentum-conserving δ function in Eq. (7.5) over the azimuthal angles analytically [147]

$$\int_0^{2\pi} d\phi_1 d\phi_2 d\phi_3 \delta^3(P_1 + P_2 + P_3) = \frac{4\pi\,\Theta\left(\frac{3}{4} - c_1c_2 - c_1^2 - c_2^2\right)}{p_{Fn}^3\sqrt{\frac{3}{4} - c_1c_2 - c_1^2 - c_2^2}}\delta(c_1 + c_2 + c_3) \tag{7.19}$$

where $c_j \equiv \cos(\theta_j)$ and Θ is the unit step function. We then perform the remaining angular and radial integrals numerically.

Fig. 7.6 shows how the neutrino emissivity is affected by increasing the amplitude of compression oscillations. Since the neutrons are gapped everywhere on the Fermi surface we expect the results to be similar to those calculated for $^1S_0$ neutron pairing in Sec. 7.3, and comparing Fig. 7.6 with Fig. 7.2 we see this this is indeed the case. The overall pattern of the dependence on T and $\hat{\mu}_\Delta$ is the same, the only difference is that $R_{\bar{\epsilon}}$ for $^3P_2(J_z = 0)$ pairing is smaller than for $^1S_0$ pairing by a factor that varies between 400 and 20 as $\hat{\mu}_\Delta$ ranges from 0 to $5\Delta_n$.

7.4.2 $^3P_2(J_z = \pm 2)$ neutron pairing

We now consider the case where the neutron Cooper pairs are in the $^3P_2$ state with $|J_z| = 2$ while the protons pair in the $^1S_0$ channel. The angular dependence of the neutron gap in this channel is [142]

$$\Delta_n(\theta) = \Delta_{n0} \sin(\theta) \tag{7.20}$$

Note that the neutron gap vanishes at the poles and has a maximum value of Δ_{n0} around the equator.

In Fig. 7.7, we show the effect of increasing the amplitude of the applied compression oscillations. To explain this figure we first explain how the angular dependence of the gap affects the modified Urca process. In Fig. 7.8 we have plotted a typical arrangement of the neutron momenta. To understand the overall behavior we can neglect the proton and electron Fermi momenta, which are significantly smaller than the neutron Fermi momentum. The momenta of the incoming neutrons n_1 and n_2 (Fig. 7.1) then add up to the momentum of the outgoing neutron n_3. Since all three neutron momenta lie near the neutron Fermi surface, p_{n1} and p_{n2} must be at a 60° angle to p_{n3}, on opposite sides in the same plane. Only one of the three neutrons can be at the gapless node on their Fermi surface. In Fig. 7.8 we placed p_{n3} at the node. The other two neutron momenta are at $\theta = \pi/3$ where the gap is $\sqrt{3}\Delta_{n0}/2$.

We can now understand the effect of increasing the amplitude of the applied compression oscillations, as shown in Fig. 7.7. For low amplitudes the neutrino emissivity is exponentially suppressed by the gap, roughly as $\exp(-1.73\Delta_{n0}/T)$, as compared with $\exp(-2\Delta_n/T)$ for

$^1S_0$ neutron pairing (Fig. 7.2). It is natural to expect the $^3P_2(J_z = \pm 2)$ pairing to be less suppressed because there is a gapless node on the neutron Fermi surface.

To understand more fully the origin of the suppression factor, we analyze one of the dominant channels at low $\hat{\mu}_\Delta/\Delta_{n0}$, shown in Fig. 7.9 (a). In the figure we show two neutron Fermi seas, one gapless, corresponding to a neutron momentum at the gapless node on the Fermi surface (polar angle $\theta = 0$), and one with a gap of $\sqrt{3}\Delta_{n0}/2 \approx 0.866\Delta_{n0}$, corresponding to neutron momenta at $\theta = \pi/3$ or $2\pi/3$. For the process shown in Fig. 7.9 (a) there is a suppression factor of $\exp(-\sqrt{3}\Delta_{n0}/t) \approx \exp(-1.73\Delta_{n0}/t)$, arising from the unlikelihood of finding both initial state neutrons in the sparsely occupied region above the gap at $\theta = \pi/3$. The final state neutron is at the gapless node, and so experiences no Boltzmann suppression. The electron is created above its Fermi surface (because the hadrons provide an energy surplus to be absorbed by the electron) so it too experiences no Boltzmann suppression.

As we see in Fig. 7.7, increasing the amplitude of compression oscillation leads to gap bridging: some of the β processes become unsuppressed which results in steady increase of the neutrino emissivity until at $\hat{\mu}_\Delta/\Delta_{n0} \approx 2.73$ the β process rate reaches the ungapped limit ($R_\epsilon \sim 1$), regardless of how low the temperature may be.

To understand why complete gap bridging happens at $\hat{\mu}_\Delta/\Delta_{n0} \approx 2.73$, we show in Fig. 7.9 (b) the channel of class 1 (Fig. 7.3) which dominates at large $\hat{\mu}_\Delta/\Delta_{n0}$. As in the case of $^1S_0$ neutron pairing, this is because all the suppression comes from the energy requirements of the hadronic sector, none from hadronic Fermi-Dirac factors (all hadrons start below the gap and end in the sparsely occupied region above the gap). At $\hat{\mu}_\Delta = 0$ the energy required

for this is $0.866\Delta_{n0}$ for $n_1 \to n_3$ and $0.866\Delta_{n0} + \Delta_p$ for $n_2 \to p$, totalling $2.73\Delta_{n0}$ assuming $\Delta_p = \Delta_{n0}$. This energy is supplied by the electron, which must be created deep in its Fermi sea at a free energy of $-2.73\Delta_{n0}$, yielding a Boltzmann suppression of $\exp(-2.73\Delta_{n0}/T)$.

As we increase $\hat{\mu}_\Delta$, the proton Fermi surface is lowered by $\hat{\mu}_\Delta$ relative to the neutron Fermi surface and the $n \to p$ process requires less and less energy. At $\hat{\mu}_\Delta = 1.866\Delta_{n0}$ the $n \to p$ process breaks even, and at $\hat{\mu}_\Delta = 2.73\Delta_{n0}$ it can provide all the energy needed by the spectator neutron. The electron can then be created above its Fermi energy. All Boltzmann suppression has then been canceled by gap bridging, and further increase in μ_Δ produces only suprathermal enhancement.

7.5 Conclusion and discussion

We have shown that the exponential suppression of flavor-changing β processes in superfluid and superconducting nuclear matter can be completely overcome, via the mechanism of gap bridging, by compression oscillations of sufficiently high amplitude, regardless of how low the temperature may be. This confirms the conjecture outlined in previous work [126], and shows that it applies to the realistic case of modified Urca processes and ${}^3P_2$ neutron pairing.

We expect gap bridging to be relevant in processes that induce density oscillations of amplitude $\Delta n/\bar{n} \sim 10^{-3}$ to 10^{-2} [126]. This is sufficient to overcome typical nucleon pairing gaps which are of order 1 MeV. In hyperonic [148, 149] or quark [150, 151] matter, there are processes which are only suppressed by $\Delta \lesssim 0.01\,\mathrm{MeV}$, and these could be bridged by oscillations with amplitudes as small as $\Delta n/\bar{n} \lesssim 10^{-4}$. Relevant physical scenarios that are likely to involve high-amplitude oscillations include unstable oscillations of rotating compact

stars such as f-modes or r-modes [136], events like star quakes [124], and neutron star mergers [125]. When such high-amplitude compression oscillations occur in superfluid or superconducting matter, certain transport properties, such as bulk viscosity and neutrino emissivity, will be greatly enhanced, leading to nonlinear (in amplitude) damping of the mode itself, and enhanced cooling via neutrino emission.

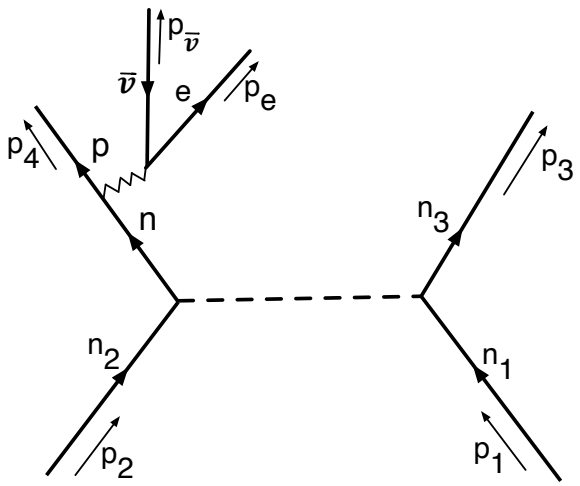

Figure 7.1: Feynman diagram for a modified Urca process. The initial state contains two neutrons: n_2, which undergoes β decay to a proton, and n_1, which is a spectator, interacting with the other neutron or proton via the strong nuclear force.

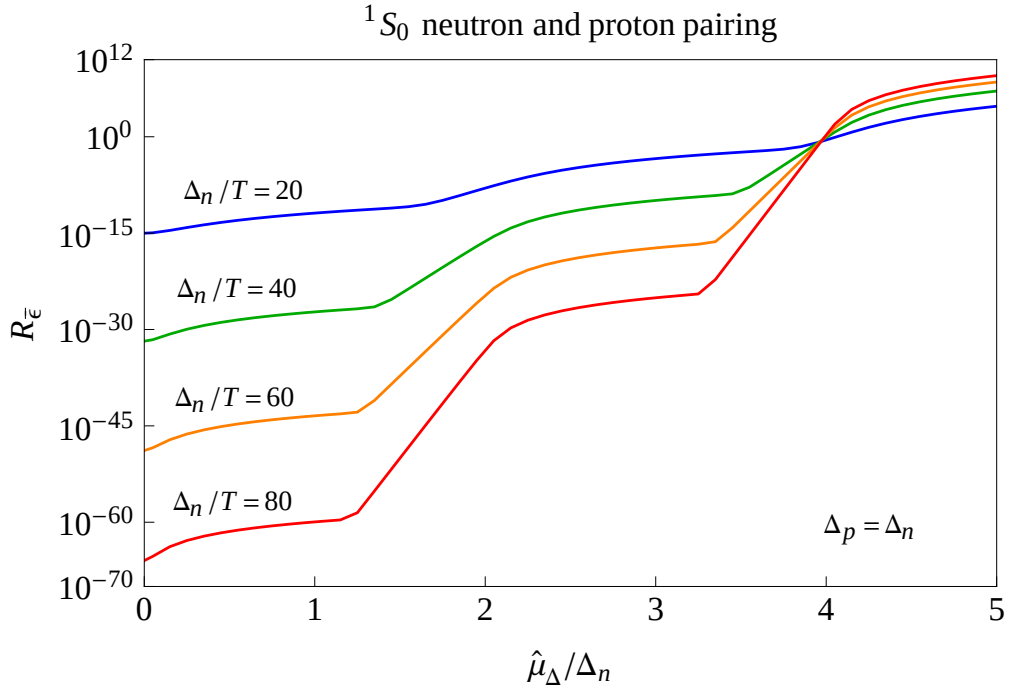

Figure 7.2: Dependence of neutrino emissivity [via the averaged modification function $R_{\bar{\epsilon}}$, Eqs. (7.13) and (7.4)] on the amplitude of the applied oscillation [via the departure μ_Δ from β equilibrium, Eq. (7.10)], for $^1S_0$ neutron and proton pairing. At low amplitude the emissivity is Boltzmann suppressed by the gaps, but for high enough amplitude gap bridging reverses the suppression.

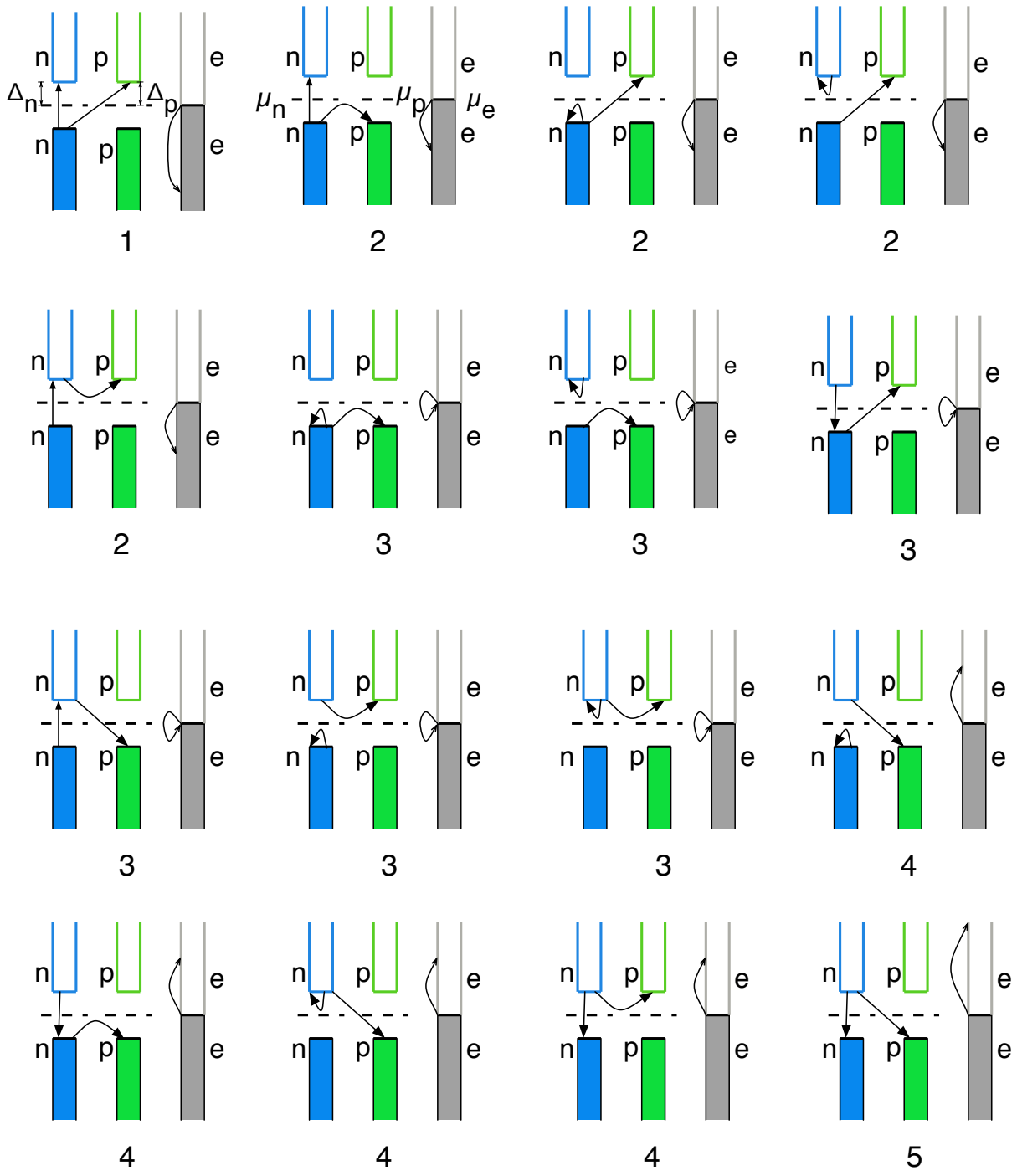

Figure 7.3: The 16 channels that contribute to the modified Urca process. For each channel we show the three Fermi seas: from left to right, neutron (gapped), proton (gapped), and electron (ungapped) with their Fermi energies aligned. The black arrows show the transitions of the spectator neutron (leftmost arrow), the $n \leftrightarrow p$ conversion (arrow that goes from neutron to proton Fermi sea) and electron (rightmost arrow). The vertical lengths of the arrows represent the free energy input or output; by energy conservation these add up to zero in each process.

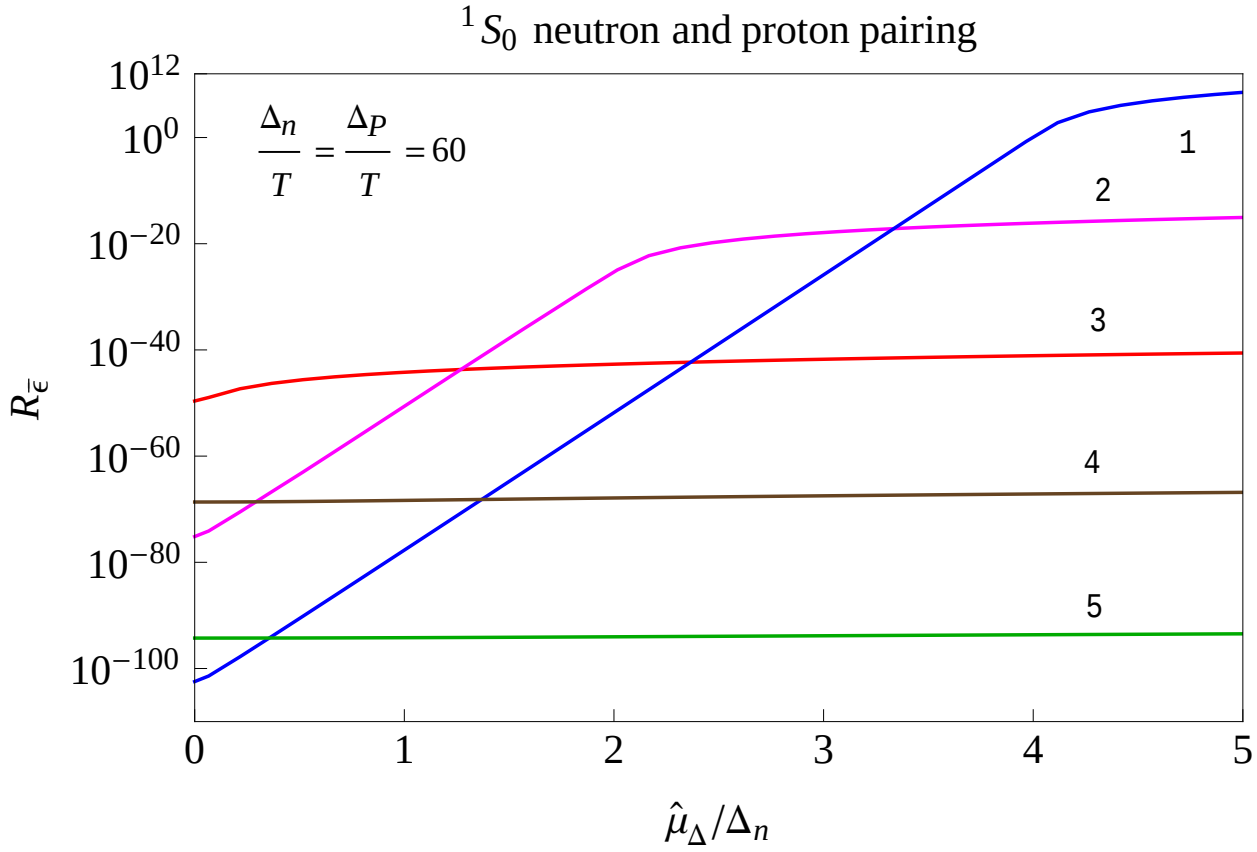

Figure 7.4: Amplitude dependence of the neutrino emissivity for different channels that contribute to the modified Urca process. This explains the step structure in Fig. 7.2

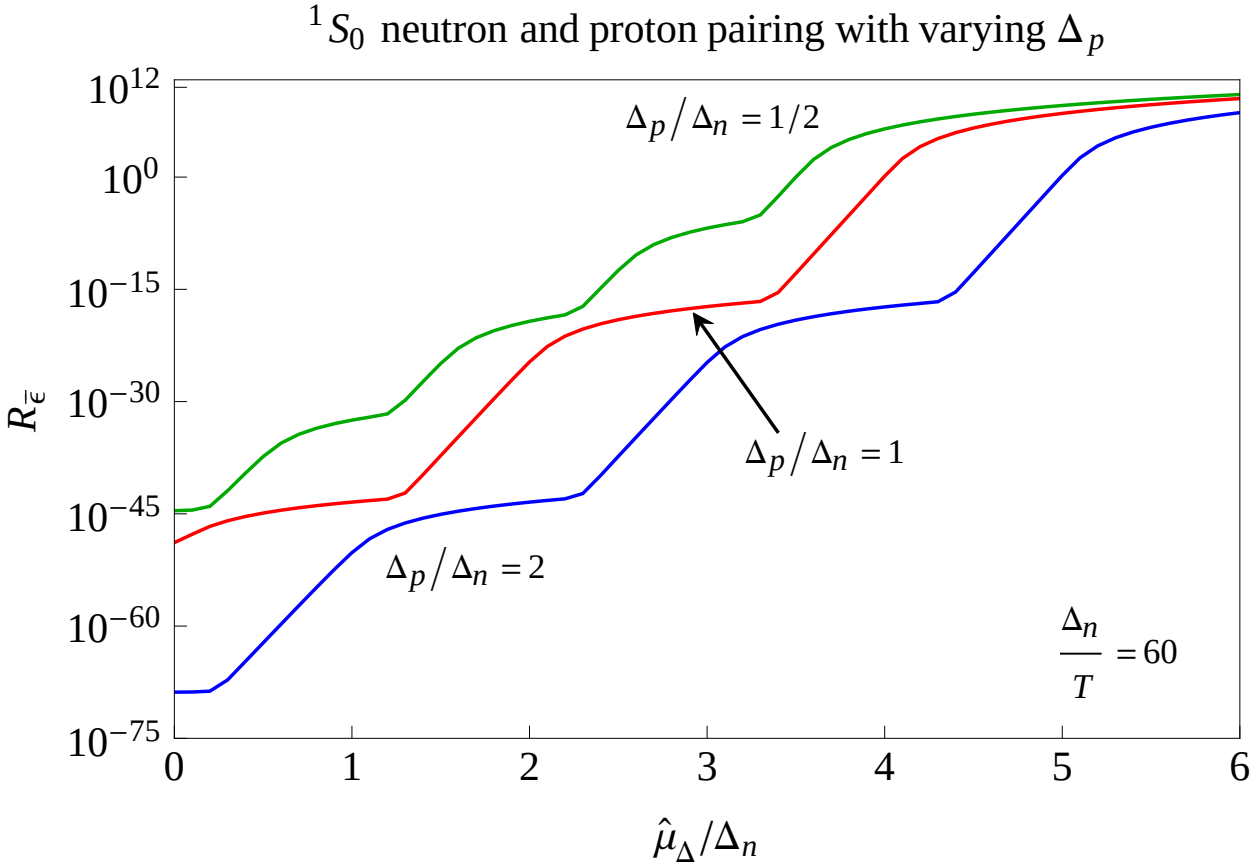

Figure 7.5: How the amplitude dependence of the neutrino emissivity depends on the $^1S_0$ proton pairing gap, for $^1S_0$ neutron pairing with $\Delta_n/T = 60$. We show curves for $\Delta_p/\Delta_n = 1/2,\ 1,\ 2$.

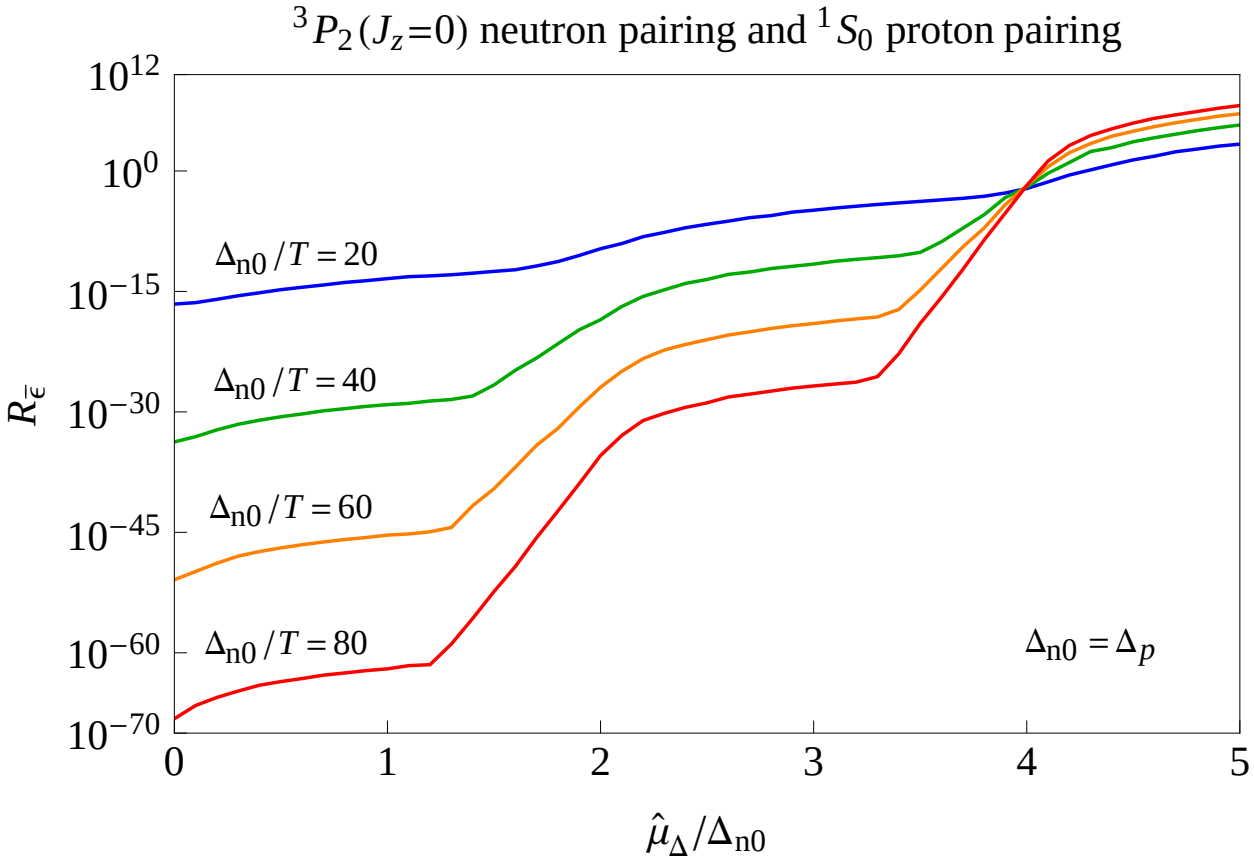

Figure 7.6: Dependence of the neutrino emissivity on the amplitude of the applied compression oscillations, for $^3P_2$ ($J_z = 0$) neutron pairing and $^1S_0$ proton pairing.

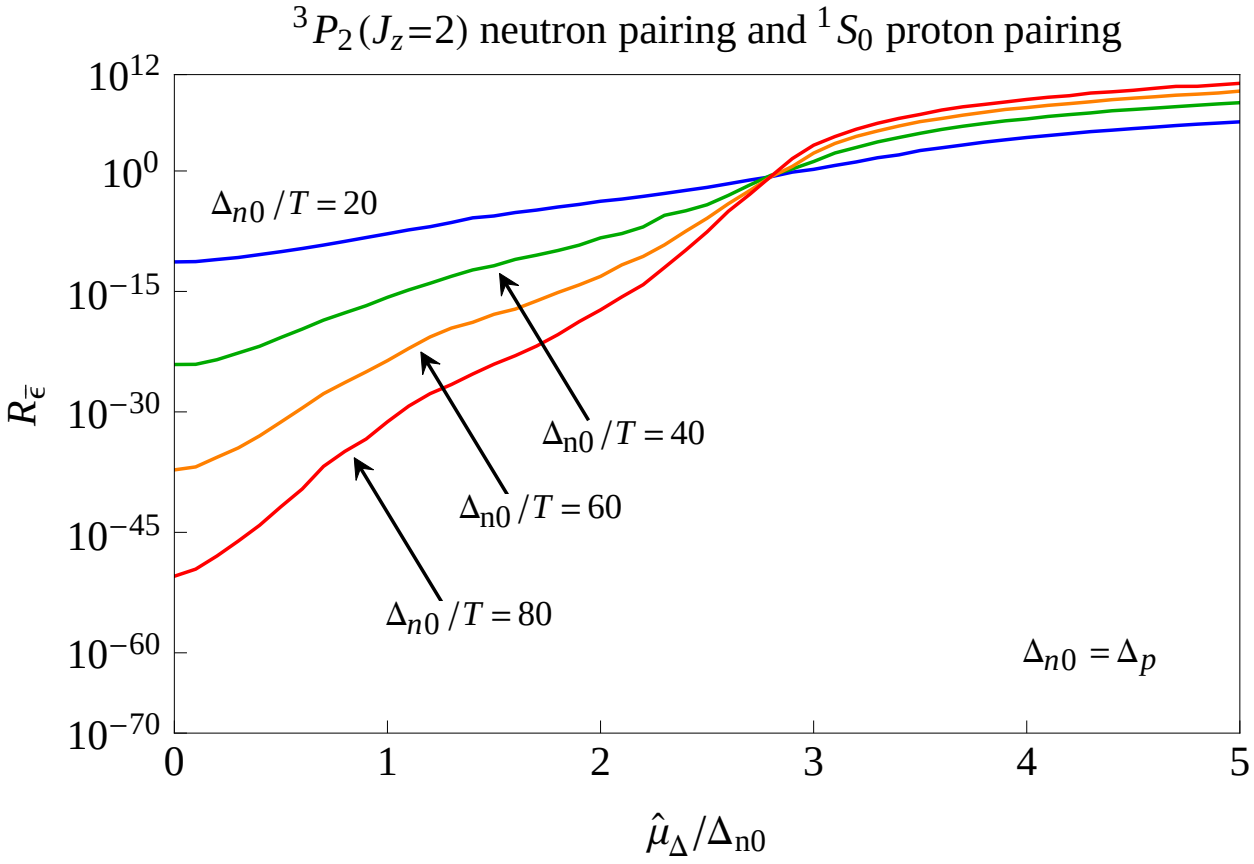

Figure 7.7: Dependence of the neutrino emissivity on the amplitude of the applied compression oscillations, for $^3P_2$ ($J_z = 2$) neutron pairing and $^1S_0$ proton pairing.

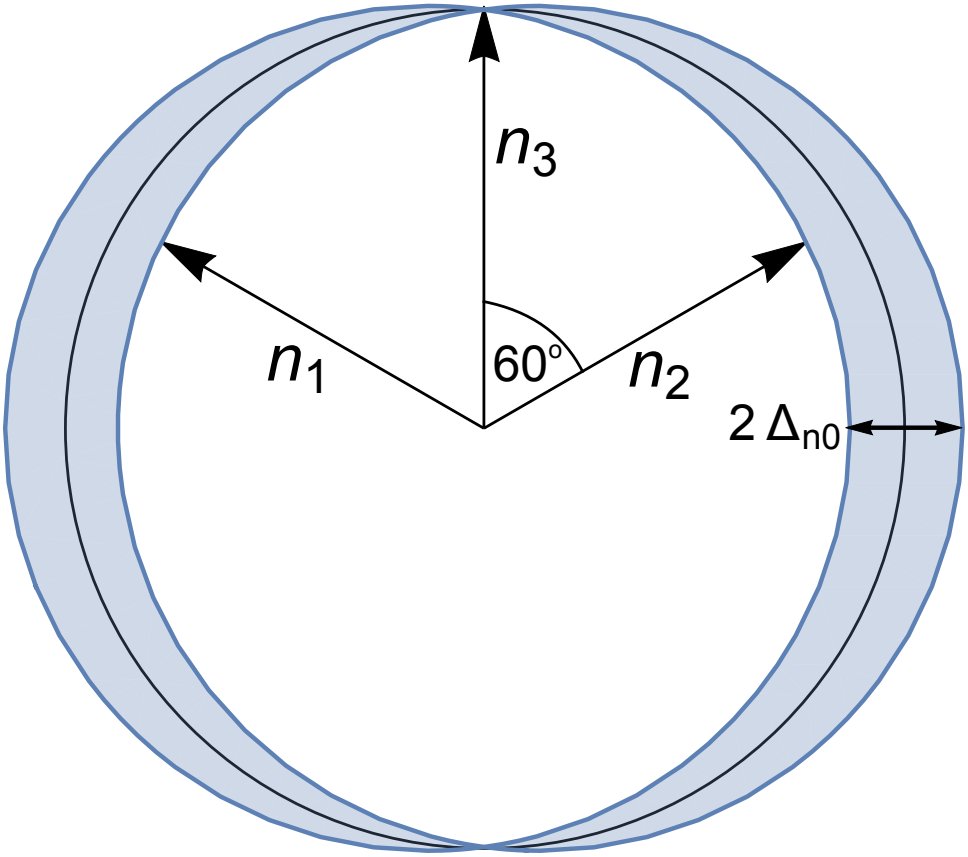

Figure 7.8: Momenta of the neutrons in one example of a typical Urca process in a ${}^3P_s(J_z = \pm 2)$ neutron superfluid. The shaded region is the gap at the neutron Fermi surface. The momenta of the two initial state neutrons n_1 and n_2 add up to the momentum of the final state neutron n_3 (neglecting the proton and electron momenta). Only one of the three neutron momenta can be at a gapless node on the Fermi surface.

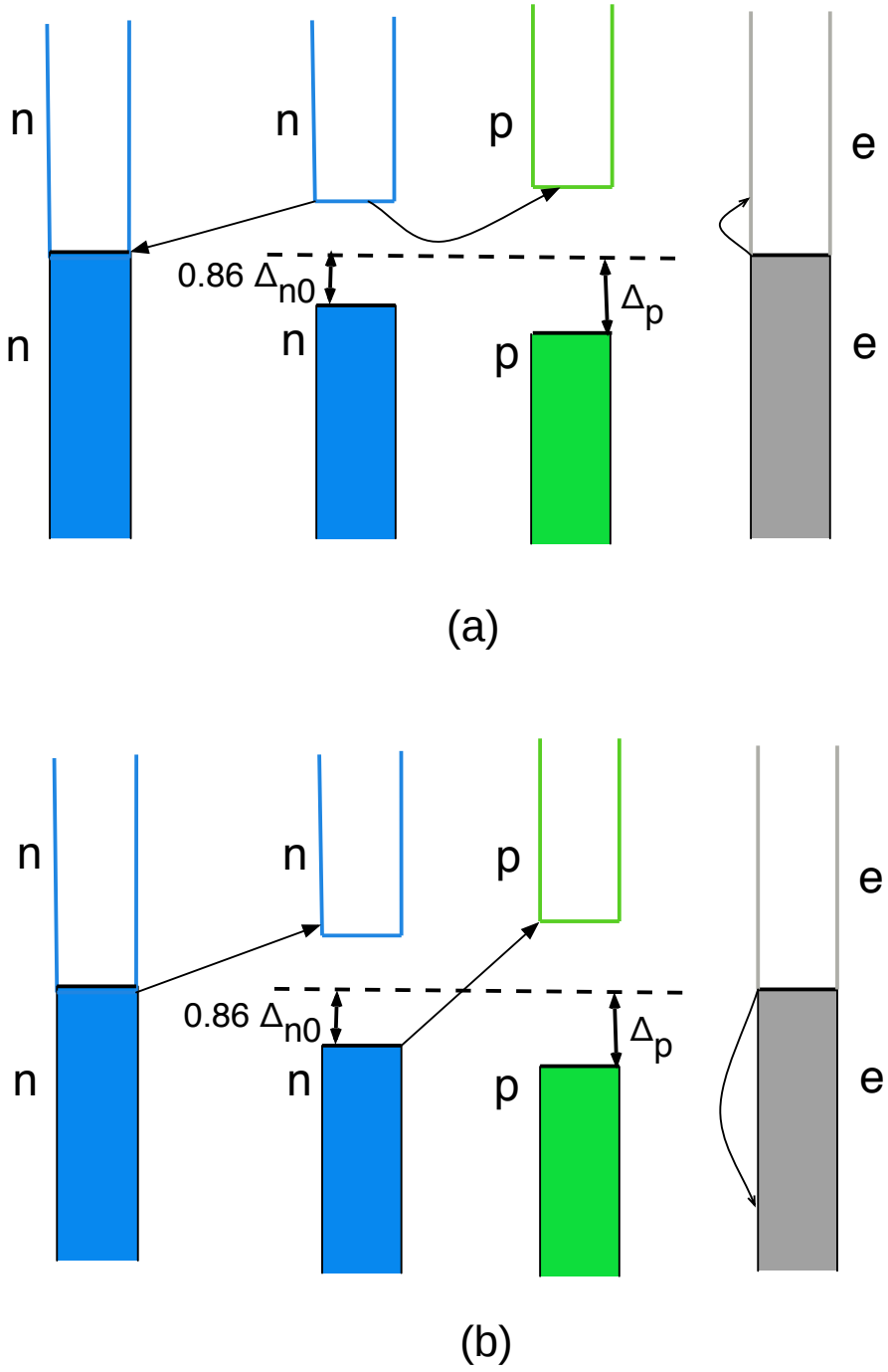

Figure 7.9: Channels that in the presence of ${}^3P_2(J_z = \pm 2)$ neutron pairing and ${}^1S_0$ proton pairing, will dominate the modified Urca process in different regimes: (a) at low μ_Δ/Δ_{n0}, (b) at high μ_Δ/Δ_{n0}.

BIBLIOGRAPHY

[1] M. Gell-Mann. A schematic model of baryons and mesons. *Physics Letters*, 8:214–215, February 1964.

[2] G. Zweig. An SU(3) model for strong interaction symmetry and its breaking. Version 1. 1964.

[3] Jerome I. Friedman. Deep Inelastic Scattering Evidence for the Reality of Quarks. *NATO Sci. Ser. B*, 352:725–741, 1996.

[4] Jerome I Friedman and Henry W Kendall. Deep inelastic electron scattering. *Annual Review of Nuclear Science*, 22(1):203–254, 1972.

[5] Richard E Taylor. Deep inelastic scattering: The early years. *Reviews of Modern Physics*, 63(3):573, 1991.

[6] D. P. Barber, U. Becker, H. Benda, A. Boehm, J. G. Branson, J. Bron, D. Buikman, J. Burger, C. C. Chang, H. S. Chen, M. Chen, C. P. Cheng, Y. S. Chu, R. Clare, P. Duinker, G. Y. Fang, H. Fesefeldt, D. Fong, M. Fukushima, J. C. Guo, A. Hariri, G. Herten, M. C. Ho, H. K. Hsu, T. T. Hsu, R. W. Kadel, W. Krenz, J. Li, Q. Z. Li, M. Lu, D. Luckey, D. A. Ma, C. M. Ma, G. G. G. Massaro, T. Matsuda, H. Newman, J. Paradiso, F. P. Poschmann, J. P. Revol, M. Rohde, H. Rykaczewski, K. Sinram,

H. W. Tang, L. G. Tang, Samuel C. C. Ting, K. L. Tung, F. Vannucci, X. R. Wang, P. S. Wei, M. White, G. H. Wu, T. W. Wu, J. P. Xi, P. C. Yang, X. H. Yu, N. L. Zhang, and R. Y. Zhu. Discovery of three-jet events and a test of quantum chromodynamics at petra. *Phys. Rev. Lett.*, 43:830–833, Sep 1979.

[7] Ch Berger, H Genzel, R Grigull, W Lackas, F Raupach, A Klovning, E Lillestöl, E Lillethun, JA Skard, H Ackermann, et al. Evidence for gluon bremsstrahlung in e+ e- annihilations at high energies. *Physics Letters B*, 86(3-4):418–425, 1979.

[8] R Brandelik, W Braunschweig, K Gather, V Kadansky, K Lübelsmeyer, P Mättig, H-U Martyn, G Peise, J Rimkus, HG Sander, et al. Evidence for planar events in e+ e- annihilation at high energies. *Physics Letters B*, 86(2):243–249, 1979.

[9] David J. Gross and Frank Wilczek. Ultraviolet behavior of non-abelian gauge theories. *Phys. Rev. Lett.*, 30:1343–1346, Jun 1973.

[10] H. David Politzer. Reliable perturbative results for strong interactions? *Phys. Rev. Lett.*, 30:1346–1349, Jun 1973.

[11] Mark Srednicki. *Quantum field theory.* Cambridge University Press, 2007.

[12] Claude Bernard, Tom Burch, Kostas Orginos, Doug Toussaint, Thomas A. DeGrand, Carleton DeTar, Saumen Datta, Steven Gottlieb, Urs M. Heller, and Robert Sugar. Qcd spectrum with three quark flavors. *Phys. Rev. D*, 64:054506, Aug 2001.

[13] Stefan Dürr, Zoltàn Fodor, Julien Frison, Christian Hoelbling, Roland Hoffmann,

SD Katz, Stefan Krieg, Thorsten Kurth, Laurent Lellouch, Thomas Lippert, et al. Ab initio determination of light hadron masses. *Science*, 322(5905):1224–1227, 2008.

[14] Kenneth G Wilson. Confinement of quarks. *Physical Review D*, 10(8):2445, 1974.

[15] Tom Banks and A Casher. Chiral symmetry breaking in confining theories. *Nuclear Physics B*, 169(1):103–125, 1980.

[16] Paul H Ginsparg and Kenneth G Wilson. A remnant of chiral symmetry on the lattice. *Physical Review D*, 25(10):2649, 1982.

[17] John B. Kogut. An introduction to lattice gauge theory and spin systems. *Rev. Mod. Phys.*, 51:659–713, Oct 1979.

[18] Michael Creutz, Laurence Jacobs, and Claudio Rebbi. Monte carlo computations in lattice gauge theories. *Physics Reports*, 95(4):201–282, 1983.

[19] Jean-Michel Drouffe and Jean-Bernard Zuber. Strong coupling and mean field methods in lattice gauge theories. *Physics Reports*, 102(1-2):1–119, 1983.

[20] C Gattringer and Christian B Lang. Quantum chromodynamics on the lattice, vol. 788 of lect. *Notes Phys., Springer,*, 2009.

[21] H.J. Rothe. *Lattice Gauge Theories: An Introduction*. EBSCO ebook academic collection. World Scientific, 2005.

[22] Michael C Ogilvie. Phases of gauge theories. *Journal of Physics A: Mathematical and Theoretical*, 45(48):483001, 2012.

[23] J Greensite. The confinement problem in lattice gauge theory. *Progress in Particle and Nuclear Physics*, 51(1):1–83, 2003.

[24] Michael C. Ogilvie. Phases of Gauge Theories. *J.Phys.*, A45:483001, 2012.

[25] Larry McLerran and Robert D. Pisarski. Phases of dense quarks at large nc. *Nuclear Physics A*, 796(1):83 – 100, 2007.

[26] Mark G. Alford, Andreas Schmitt, Krishna Rajagopal, and Thomas Schäfer. Color superconductivity in dense quark matter. *Rev. Mod. Phys.*, 80:1455–1515, Nov 2008.

[27] Miklos Gyulassy and Larry McLerran. New forms of qcd matter discovered at rhic. *Nuclear Physics A*, 750(1):30 – 63, 2005.

[28] Mark Alford, David Blaschke, Alessandro Drago, T Klähn, Giuseppe Pagliara, and Juergen Schaffner-Bielich. Astrophysics: Quark matter in compact stars? *Nature*, 445(7125):E7–E8, 2007.

[29] GM Fuller, GJ Mathews, and CR Alcock. Quark-hadron phase transition in the early universe: Isothermal baryon-number fluctuations and primordial nucleosynthesis. *Physical Review D*, 37(6):1380, 1988.

[30] A Ali Khan, S Aoki, R Burkhalter, S Ejiri, M Fukugita, S Hashimoto, N Ishizuka, Y Iwasaki, K Kanaya, T Kaneko, et al. Phase structure and critical temperature of two-flavor qcd with a renormalization group improved gauge action and clover improved wilson quark action. *Physical review D*, 63(3):034502, 2000.

[31] Edwin Laermann and Owe Philipsen. Lattice qcd at finite temperature. *Annual Review of Nuclear and Particle Science*, 53(1):163–198, 2003.

[32] J Kogut, H Matsuoka, M Stone, HW Wyld, S Shenker, J Shigemitsu, and DK Sinclair. Quark and gluon latent heats at the deconfinement phase transition in su (3) gauge theory. *Physical Review Letters*, 51(10):869, 1983.

[33] Frank R. Brown, Norman H. Christ, Yuefan Deng, Mingshen Gao, and Thomas J. Woch. Nature of the deconfining phase transition in su(3) lattice gauge theory. *Phys. Rev. Lett.*, 61:2058–2061, Oct 1988.

[34] LG Yaffe and B Svetitsky. First-order phase transition in the su (3) gauge theory at finite temperature. *Physical Review D*, 26(4):963, 1982.

[35] Y. Aoki, G. Endrodi, Z. Fodor, S. D. Katz, and K. K. Szabo. The Order of the quantum chromodynamics transition predicted by the standard model of particle physics. *Nature*, 443:675–678, 2006.

[36] D. T. Son and M. A. Stephanov. Dynamic universality class of the QCD critical point. *Phys. Rev.*, D70:056001, 2004.

[37] Roy A. Lacey. Indications for a Critical End Point in the Phase Diagram for Hot and Dense Nuclear Matter. *Phys. Rev. Lett.*, 114(14):142301, 2015.

[38] Mark G. Alford, Krishna Rajagopal, and Frank Wilczek. QCD at finite baryon density: Nucleon droplets and color superconductivity. *Phys. Lett.*, B422:247–256, 1998.

[39] D. Bailin and A. Love. Superfluidity and Superconductivity in Relativistic Fermion Systems. *Phys. Rept.*, 107:325, 1984.

[40] Mark G. Alford, Krishna Rajagopal, and Frank Wilczek. Color flavor locking and chiral symmetry breaking in high density QCD. *Nucl. Phys.*, B537:443–458, 1999.

[41] Philippe de Forcrand. Simulating QCD at finite density. *PoS*, LAT2009:010, 2009.

[42] Sourendu Gupta. QCD at finite density. *PoS*, LATTICE2010:007, 2010.

[43] Gert Aarts. Complex Langevin dynamics and other approaches at finite chemical potential. *PoS*, LATTICE2012:017, 2012.

[44] Ian Barbour, Nasr-Eddine Behilil, Elbio Dagotto, Frithjof Karsch, Adriana Moreo, Michael Stone, and HW Wyld. Problems with finite density simulations of lattice qcd. *Nuclear Physics B*, 275(2):296–318, 1986.

[45] Yoichiro Nambu and Giovanni Jona-Lasinio. Dynamical model of elementary particles based on an analogy with superconductivity. i. *Physical Review*, 122(1):345, 1961.

[46] Yoichiro Nambu and Giovanni Jona-Lasinio. Dynamical model of elementary particles based on an analogy with superconductivity. ii. *Physical Review*, 124(1):246, 1961.

[47] SP Klevansky. The nambujona-lasinio model of quantum chromodynamics. *Reviews of Modern Physics*, 64(3):649, 1992.

[48] U Vogl and W Weise. The nambu and jona-lasinio model: its implications for hadrons and nuclei. *Progress in Particle and Nuclear Physics*, 27:195–272, 1991.

[49] Michael Buballa. Njl-model analysis of dense quark matter. *Physics Reports*, 407(4):205–376, 2005.

[50] M Fukugita and A Ukawa. Deconfining and chiral transitions of finite-temperature quantum chromodynamics in the presence of dynamical quark loops. *Physical Review Letters*, 57(5):503, 1986.

[51] Yasumichi Aoki, Z Fodor, SD Katz, and KK Szabo. The qcd transition temperature: Results with physical masses in the continuum limit. *Physics Letters B*, 643(1):46–54, 2006.

[52] A Gocksch and Michael Ogilvie. Finite-temperature deconfinement and chiral-symmetry restoration at strong coupling. *Physical Review D*, 31(4):877, 1985.

[53] Peter N Meisinger and Michael C Ogilvie. Chiral symmetry restoration and zn symmetry. *Physics Letters B*, 379(1-4):163–168, 1996.

[54] Kenji Fukushima. Chiral effective model with the polyakov loop. *Physics Letters B*, 591(3):277–284, 2004.

[55] Marco Cristoforetti, Luigi Scorzato, and Francesco Di Renzo. The sign problem and the Lefschetz thimble. *J.Phys.Conf.Ser.*, 432:012025, 2013.

[56] H. Fujii, D. Honda, M. Kato, Y. Kikukawa, S. Komatsu, et al. Hybrid Monte Carlo on Lefschetz thimbles - A study of the residual sign problem. *JHEP*, 1310:147, 2013.

[57] M. Cristoforetti, F. Di Renzo, A. Mukherjee, and L. Scorzato. Quantum field theories on the Lefschetz thimble. *PoS*, LATTICE2013:197, 2014.

[58] Marco Cristoforetti, Francesco Di Renzo, Abhishek Mukherjee, and Luigi Scorzato. Monte Carlo simulations on the Lefschetz thimble: Taming the sign problem. *Phys.Rev.*, D88(5):051501, 2013.

[59] M. Cristoforetti, F. Di Renzo, G. Eruzzi, A. Mukherjee, C. Schmidt, et al. An efficient method to compute the residual phase on a Lefschetz thimble. *Phys.Rev.*, D89:114505, 2014.

[60] M. Cristoforetti, F. Di Renzo, A. Mukherjee, and L. Scorzato. Lefschetz thimbles and sign problem: rst results in 0 and 4 dimensional eld theories. *PoS*, QCD-TNT-III:010, 2014.

[61] Simon Hands, Timothy J. Hollowood, and Joyce C. Myers. Numerical Study of the Two Color Attoworld. *JHEP*, 1012:057, 2010.

[62] Simon Hands, Timothy J. Hollowood, and Joyce C. Myers. QCD with Chemical Potential in a Small Hyperspherical Box. *JHEP*, 1007:086, 2010.

[63] Timothy J. Hollowood, S. Prem Kumar, and Joyce C. Myers. Weak coupling large-N transitions at finite baryon density. *JHEP*, 1111:138, 2011.

[64] Timothy J. Hollowood and Joyce C. Myers. Deconfinement transitions of large N QCD with chemical potential at weak and strong coupling. *JHEP*, 1210:067, 2012.

[65] Kenji Fukushima. Chiral effective model with the Polyakov loop. *Phys.Lett.*, B591:277–284, 2004.

[66] Joyce C. Myers and Michael C. Ogilvie. New phases of SU(3) and SU(4) at finite temperature. *Phys.Rev.*, D77:125030, 2008.

[67] Mithat Unsal. Abelian duality, confinement, and chiral symmetry breaking in QCD(adj). *Phys.Rev.Lett.*, 100:032005, 2008.

[68] Michael Buballa and Igor A. Shovkovy. A Note on color neutrality in NJL-type models. *Phys.Rev.*, D72:097501, 2005.

[69] Carl M. Bender and Stefan Boettcher. Real spectra in nonHermitian Hamiltonians having PT symmetry. *Phys.Rev.Lett.*, 80:5243–5246, 1998.

[70] Peter N. Meisinger and Michael C. Ogilvie. PT Symmetry in Classical and Quantum Statistical Mechanics. *Phil.Trans.Roy.Soc.Lond.*, A371:20120058, 2013.

[71] C.P. Korthals Altes, Robert D. Pisarski, and Annamaria Sinkovics. The Potential for the phase of the Wilson line at nonzero quark density. *Phys.Rev.*, D61:056007, 2000.

[72] Peter N. Meisinger and Michael C. Ogilvie. Complete high temperature expansions for one loop finite temperature effects. *Phys.Rev.*, D65:056013, 2002.

[73] Peter N. Meisinger, Travis R. Miller, and Michael C. Ogilvie. Phenomenological equations of state for the quark gluon plasma. *Phys.Rev.*, D65:034009, 2002.

[74] Mithat Unsal and Laurence G. Yaffe. Center-stabilized Yang-Mills theory: Confinement and large N volume independence. *Phys.Rev.*, D78:065035, 2008.

[75] Bernd-Jochen Schaefer, Jan M. Pawlowski, and Jochen Wambach. The Phase Structure of the Polyakov–Quark-Meson Model. *Phys.Rev.*, D76:074023, 2007.

[76] Apoorva Patel. Flux Tube Model Signals for Baryon Correlations in Heavy Ion Collisions. *Phys.Rev.*, D85:114019, 2012.

[77] Apoorva Patel. Baryon Number Correlations in Heavy Ion Collisions. *PoS*, LATTICE2012:096, 2012.

[78] Denes Sexty. New algorithms for finite density QCD. 2014.

[79] Hiromichi Nishimura, Michael C. Ogilvie, and Kamal Pangeni. Complex saddle points in QCD at finite temperature and density. *Phys.Rev.*, D90:045039, 2014.

[80] Gert Aarts and Ion-Olimpiu Stamatescu. Stochastic quantization at finite chemical potential. *JHEP*, 0809:018, 2008.

[81] John Stephenson. Ising model with antiferromagnetic next-nearest-neighbor coupling: Spin correlations and disorder points. *Phys. Rev. B*, 1:4405–4409, Jun 1970.

[82] John Stephenson. Two one-dimensional ising models with disorder points. *Canadian Journal of Physics*, 48(14):1724–1734, 1970.

[83] Walter Selke. The annni model a theoretical analysis and experimental application. *Physics Reports*, 170(4):213 – 264, 1988.

[84] S.P. Klevansky. The Nambu-Jona-Lasinio model of quantum chromodynamics. *Rev.Mod.Phys.*, 64:649–708, 1992.

[85] Hiromichi Nishimura and Michael C. Ogilvie. A PNJL Model for Adjoint Fermions with Periodic Boundary Conditions. *Phys.Rev.*, D81:014018, 2010.

[86] Tetsuo Hatsuda and Teiji Kunihiro. QCD phenomenology based on a chiral effective Lagrangian. *Phys.Rept.*, 247:221–367, 1994.

[87] Tohru Eguchi. A New Approach to Collective Phenomena in Superconductivity Models. *Phys.Rev.*, D14:2755, 1976.

[88] Shotaro Imai, Hiroshi Toki, and Wolfram Weise. Quark-Hadron Matter at Finite Temperature and Density in a Two-Color PNJL model. *Nucl.Phys.*, A913:71–102, 2013.

[89] Thomas C. Blum, James E. Hetrick, and Doug Toussaint. High density QCD with static quarks. *Phys.Rev.Lett.*, 76:1019–1022, 1996.

[90] Kouji Kashiwa, Robert D. Pisarski, and Vladimir V. Skokov. Critical endpoint for deconfinement in matrix and other effective models. *Phys.Rev.*, D85:114029, 2012.

[91] Erhard Seiler, Denes Sexty, and Ion-Olimpiu Stamatescu. Gauge cooling in complex Langevin for QCD with heavy quarks. *Phys. Lett.*, B723:213–216, 2013.

[92] Gert Aarts, Lorenzo Bongiovanni, Erhard Seiler, Denes Sexty, and Ion-Olimpiu Sta-

matescu. Controlling complex Langevin dynamics at finite density. *Eur. Phys. J.*, A49:89, 2013.

[93] Denes Sexty. Simulating full QCD at nonzero density using the complex Langevin equation. *Phys. Lett.*, B729:108–111, 2014.

[94] Denes Sexty. Progress in complex Langevin simulations of full QCD at non-zero density. *Nucl. Phys.*, A931:856–860, 2014.

[95] Gert Aarts, Erhard Seiler, Denes Sexty, and Ion-Olimpiu Stamatescu. Simulating QCD at nonzero baryon density to all orders in the hopping parameter expansion. *Phys. Rev.*, D90(11):114505, 2014.

[96] Keitaro Nagata, Jun Nishimura, and Shinji Shimasaki. Justification of the complex Langevin method with the gauge cooling procedure. *Progress of Theoretical and Experimental Physics*, 2016(1), 2016.

[97] Marco Cristoforetti, Francesco Di Renzo, and Luigi Scorzato. New approach to the sign problem in quantum field theories: High density QCD on a Lefschetz thimble. *Phys. Rev.*, D86:074506, 2012.

[98] Abhishek Mukherjee, Marco Cristoforetti, and Luigi Scorzato. Metropolis Monte Carlo integration on the Lefschetz thimble: Application to a one-plaquette model. *Phys.Rev.*, D88(5):051502, 2013.

[99] Gert Aarts, Lorenzo Bongiovanni, Erhard Seiler, and Denes Sexty. Some remarks on Lefschetz thimbles and complex Langevin dynamics. *JHEP*, 10:159, 2014.

[100] Yuya Tanizaki, Hiromichi Nishimura, and Kouji Kashiwa. Evading the sign problem in the mean-field approximation through Lefschetz-thimble path integral. *Phys. Rev.*, D91(10):101701, 2015.

[101] H. Fujii, S. Kamata, and Y. Kikukawa. Lefschetz thimble structure in one-dimensional lattice Thirring model at finite density. *JHEP*, 11:078, 2015.

[102] Hiromichi Nishimura, Michael C. Ogilvie, and Kamal Pangeni. Complex Saddle Points and Disorder Lines in QCD at finite temperature and density. *Phys. Rev.*, D91(5):054004, 2015.

[103] Jean-Michel Drouffe and Jean-Bernard Zuber. Strong Coupling and Mean Field Methods in Lattice Gauge Theories. *Phys. Rept.*, 102:1, 1983.

[104] Matthias Doring, Kay Huebner, Olaf Kaczmarek, and Frithjof Karsch. Color Screening and Quark-Quark Interactions in Finite Temperature QCD. *Phys. Rev.*, D75:054504, 2007.

[105] Michael C. Ogilvie and Peter N. Meisinger. PT Symmetry and QCD: Finite Temperature and Density. *SIGMA*, 5:047, 2009.

[106] Michael Ogilvie, Peter Meisinger, and Timothy Wiser. "$\mathcal{PT}$" symmetry in statistical

mechanics and the sign problem. *International Journal of Theoretical Physics*, 50:1042–1051, 2011. 10.1007/s10773-010-0626-5.

[107] Benjamin Svetitsky and Laurence G. Yaffe. Critical Behavior at Finite Temperature Confinement Transitions. *Nucl. Phys.*, B210:423, 1982.

[108] M. Billo, M. Caselle, A. D'Adda, and S. Panzeri. Finite temperature lattice QCD in the large N limit. *Int. J. Mod. Phys.*, A12:1783–1846, 1997.

[109] Tobias Rindlisbacher and Philippe de Forcrand. Two-Flavor Lattice QCD with a Finite Density of Heavy Quarks: Heavy-Dense Limit and "Particle-Hole" Symmetry. 2015.

[110] M. S. Marinov and M. V. Terentev. DYNAMICS ON THE GROUP MANIFOLDS AND PATH INTEGRAL. *Fortsch. Phys.*, 27:511, 1979.

[111] P. Menotti and E. Onofri. The Action of SU(N) Lattice Gauge Theory in Terms of the Heat Kernel on the Group Manifold. *Nucl. Phys.*, B190:288, 1981.

[112] J. B. Kogut, D. K. Sinclair, R. B. Pearson, John L. Richardson, and J. Shigemitsu. The Fluctuating String of Lattice Gauge Theory: The Heavy Quark Potential, the Restoration of Rotational Symmetry and Roughening. *Phys. Rev.*, D23:2945, 1981.

[113] Simon Hands, Seyong Kim, and Jon-Ivar Skullerud. Deconfinement in dense 2-color QCD. *Eur. Phys. J.*, C48:193, 2006.

[114] Jens Langelage, Mathias Neuman, and Owe Philipsen. Heavy dense QCD and nuclear matter from an effective lattice theory. *JHEP*, 09:131, 2014.

[115] Hiromichi Nishimura, Michael C. Ogilvie, and Kamal Pangeni. Complex spectrum of finite-density lattice QCD with static quarks at strong coupling. *Phys. Rev.*, D93(9):094501, 2016.

[116] Sidney R. Coleman and Erick J. Weinberg. Radiative Corrections as the Origin of Spontaneous Symmetry Breaking. *Phys. Rev.*, D7:1888–1910, 1973.

[117] Youngah Park and Michael E. Fisher. Identity of the universal repulsive-core singularity with yang-lee edge criticality. *Phys. Rev. E*, 60:6323–6328, Dec 1999.

[118] J. Hubbard and P. Schofield. Wilson theory of a liquid-vapour critical point. *Physics Letters A*, 40(3):245 – 246, 1972.

[119] Nikolai V. Brilliantov. Effective magnetic hamiltonian and ginzburg criterion for fluids. *Phys. Rev. E*, 58:2628–2631, Aug 1998.

[120] Michael E. Fisher and David Ruelle. The stability of many particle systems. *Journal of Mathematical Physics*, 7(2):260–270, 1966.

[121] S. F. Edwards and A. Lenard. Exact statistical mechanics of a one dimensional system with coulomb forces. ii. the method of functional integration. *Journal of Mathematical Physics*, 3(4):778–792, 1962.

[122] Sidney R. Coleman. The Quantum Sine-Gordon Equation as the Massive Thirring Model. *Phys. Rev.*, D11:2088, 1975.

[123] DJ Dean and Morten Hjorth-Jensen. Pairing in nuclear systems: from neutron stars to finite nuclei. *Reviews of Modern Physics*, 75(2):607, 2003.

[124] Lucia M Franco, Bennett Link, and Richard I Epstein. Quaking neutron stars. *The Astrophysical Journal*, 543(2):987, 2000.

[125] David Tsang, Jocelyn S. Read, Tanja Hinderer, Anthony L. Piro, and Ruxandra Bondarescu. Resonant shattering of neutron star crusts. *Phys. Rev. Lett.*, 108:011102, Jan 2012.

[126] Mark G. Alford, Sanjay Reddy, and Kai Schwenzer. Bridging the Gap by Squeezing Superfluid Matter. *Phys. Rev. Lett.*, 108:111102, 2012.

[127] J. M. Lattimer and M. Prakash. The physics of neutron stars. *Science*, 304(5670):536–542, 2004.

[128] Pawel Haensel, Aleksander Yu Potekhin, and Dmitry G Yakovlev. *Neutron stars 1: Equation of state and structure*, volume 326. Springer Science & Business Media, 2007.

[129] DG Yakovlev, AD Kaminker, Oleg Y Gnedin, and P Haensel. Neutrino emission from neutron stars. *Physics Reports*, 354(1):1–155, 2001.

[130] H. Müther and W. H. Dickhoff. Pairing properties of nucleonic matter employing dressed nucleons. *Phys. Rev. C*, 72:054313, Nov 2005.

[131] D. Ding, A. Rios, H. Dussan, W. H. Dickhoff, S. J. Witte, A. Carbone, and A. Polls.

Pairing in high-density neutron matter including short- and long-range correlations. *Phys. Rev. C*, 94:025802, Aug 2016.

[132] J. Madsen. Bulk viscosity of strange dark matter, damping of quark star vibration, and the maximum rotation rate of pulsars. *Phys. Rev.*, D46:3290–3295, 1992.

[133] Andreas Reisenegger. Deviations from chemical equilibrium due to spindown as an internal heat source in neutron stars. *Astrophys. J.*, 442:749, 1995.

[134] Mark G. Alford, Simin Mahmoodifar, and Kai Schwenzer. Large amplitude behavior of the bulk viscosity of dense matter. *J. Phys.*, G37:125202, 2010.

[135] M. E. Gusakov and E. M. Kantor. Velocity-dependent energy gaps and dynamics of superfluid neutron stars. *Mon. Not. Roy. Astron. Soc.*, 428:L26–L30, 2013.

[136] Nikolaos Stergioulas. Rotating stars in relativity. *Living Reviews in Relativity*, 6(3), 2003.

[137] Mark G Alford and Kai Schwenzer. Gravitational wave emission and spin-down of young pulsars. *The Astrophysical Journal*, 781(1):26, 2014.

[138] Armen Sedrakian. Direct Urca neutrino radiation from superfluid baryonic matter. *Phys. Lett.*, B607:27–34, 2005.

[139] Armen Sedrakian. The Physics of dense hadronic matter and compact stars. *Prog. Part. Nucl. Phys.*, 58:168–246, 2007.

[140] BL Friman and OV Maxwell. Neutrino emissivities of neutron stars. *The Astrophysical Journal*, 232:541–557, 1979.

[141] D. G. Yakovlev and K. P. Levenfish. Modified urca process in neutron star cores. *A&A*, 297:717, may 1995.

[142] Tatsuyuki Takatsuka and Ryozo Tamagaki. Superfluid state in neutron star matter. ii properties of anisotropic energy gap of 3p2 pairing. *Progress of Theoretical Physics*, 46(1):114–134, 1971.

[143] Ryozo Tamagaki. Superfluid state in neutron star matter. i generalized bogoliubov transformation and existence of 3p2 gap at high density. *Progress of Theoretical Physics*, 44(4):905–928, 1970.

[144] M. Baldo, J. Cugnon, A. Lejeune, and U. Lombardo. Proton and neutron superfluidity in neutron star matter. *Nuclear Physics A*, 536:349–365, January 1992.

[145] L Amundsen and E Østgaard. Superfluidity of neutron matter:(ii). triplet pairing. *Nuclear Physics A*, 442(1):163–188, 1985.

[146] Alexander Y Potekhin, José A Pons, and Dany Page. Neutron starscooling and transport. *Space Science Reviews*, 191(1-4):239–291, 2015.

[147] ME Gusakov. Neutrino emission from superfluid neutron-star cores: Various types of neutron pairing. *Astronomy & Astrophysics*, 389(2):702–715, 2002.

[148] M. Prakash, M. Prakash, J. M. Lattimer, and C. J. Pethick. Rapid cooling of neutron stars by hyperons and Delta isobars. *Astrophys. J. Lett.*, 390:L77–L80, May 1992.

[149] P. Haensel, K. P. Levenfish, and D. G. Yakovlev. Bulk viscosity in superfluid neutron star cores. 3. Effects of sigma- hyperons. *Astron. Astrophys.*, 381:1080–1089, 2002.

[150] Andreas Schmitt, Igor A. Shovkovy, and Qun Wang. Neutrino emission and cooling rates of spin-one color superconductors. *Phys. Rev.*, D73:034012, 2006.

[151] Xinyang Wang and Igor A. Shovkovy. Bulk viscosity of spin-one color superconducting strange quark matter. *Phys.Rev.*, D82:085007, 2010.